

國立交通大學

電子物理系

博士論文

以摻釹晶體產生不同波長之高能量脈衝雷射
及其波長轉換

Generation of Various High-Pulse-Energy Lasers with Nd-Doped
Crystals and Wavelength Conversions

學 生：黃依萍

指導教授：陳永富 教授

中華民國九十九年六月

以摻釹晶體產生不同波長之高能量脈衝雷射及其波長轉換
Generation of Various High-pulse-energy Lasers with Nd-doped Crystals and
Wavelength Conversions

研究生：黃依萍

Student : Yi-Ping Huang

指導教授：陳永富

Advisor : Yung-Fu Chen

國立交通大學

電子物理系

博士論文

A Dissertation

Submitted to Department of Electrophysics

College of Science

National Chiao Tung University

in partial Fulfillment of the Requirements

for the Degree of

Doctor of Philosophy

in

Electrophysics

June 2010

Hsinchu, Taiwan, Republic of China

中華民國九十九年六月

以摻釹晶體產生不同波長之高能量脈衝雷射及其波長轉換

學生：黃依萍

指導教授：陳永富

國立交通大學電子物理學系博士班

摘 要

全固態雷射和非線性光學波長轉換技術的研究不僅具有重要的學術意義，更具有重要的應用價值。隨著高功率的雷射二極體的發展，高能量的固態雷射已成為目前的重點研究之一。各類雷射增益介質具有不同多個斯塔克分裂能級的譜線，透過實現雷射增益介質本身具有的各級譜線之波長，再結合非線性光學波長轉換技術可拓寬雷射的波長範圍與應用領域。本文是以摻釹的雷射晶體作為研究，實現低增益譜線的準三階雷射波段和人眼安全雷射波段。除了使用傳統的晶體式飽和吸收體作為被動式 Q 開關元件，我們針對不同波段設計合適的半導體材料製作成量子井飽和吸收體，以產生高效率和高能量的脈衝雷射。半導體材料除了作為雷射腔內的飽和吸收體，我們發展半導體週期性材料作為抑制強增益譜線的一種新穎元件，此元件對腔內的損耗很低，對於實現高效率的低增益譜線之雷射相當有價值。摻釹的雷射晶體在最強增益的波段 $1.0 \mu\text{m}$ 已經有相當成熟和穩定的脈衝雷射研究，對於各類的波長轉換技術是重要的關鍵之一。我們利用腔內的光學參數振盪器，產生在 $1.5 \mu\text{m}$ 附近的人眼安全波段雷射。以理論分析腔內的光學參數振盪器之優化，並以實驗佐證，發展高效率、高能量的人眼安全波段雷射及雙波長雷射。透過雷射共振腔體的設計，利用些微的熱透鏡效應去發展不穩定的雷射腔體，有效地改善雷射光束品質。

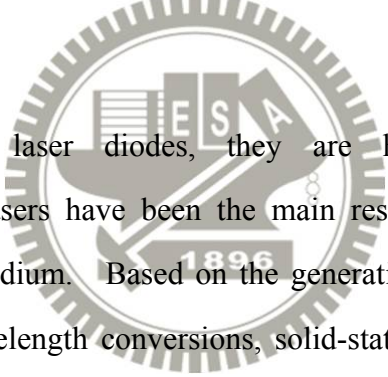
Generation of Various High-pulse-energy Lasers with Nd-doped Crystals and Wavelength Conversions

Student : Yi-Ping Huang

Advisor : Yung-Fu Chen

Department of Electrophysics
National Chiao Tung University

ABSTRACT



As the development of laser diodes, they are helpful for solid-state lasers. High-pulse-energy solid-state lasers have been the main researches. There are many laser transition lines in each laser medium. Based on the generation of various fundamental laser wavelengths and nonlinear wavelength conversions, solid-state lasers can be applied in more fields. In the thesis, Nd-doped crystals are chosen to be the laser media to realize the low-gain quasi-three-level lasers and eye-safe lasers. A good quasi-three-level laser in Q-switched regime is potential and helpful for developing pulsed blue laser. Besides the conventional bulk saturable absorbers, we develop the suitable semiconductor materials for various laser transition lines to make a QWs saturable absorber. Efficient, high-pulse-energy Q-switched lasers are generated. In addition, semiconductor materials are not only used to be the absorber for passively Q-switched laser, but also to be the novel intracavity selective absorbers used for suppressing the higher gain lines. On the other hand, Nd³⁺-doped pulsed lasers at 1.0 μm have been maturely developed for many years and possess superior performances. We utilize the Nd³⁺-doped pulsed lasers at 1.0 μm as the pump lasers to generate eye-safe intracavity OPOs. Based on the numerical analysis and cavity design, we are devoted to generate highly efficient high-energy eye-safe lasers.

誌謝

五年的交大研究所生活過得非常充實，在良好的研究環境讓我學習到很多。很幸運地可以到陳永富 教授的實驗室做研究，以及結識很多朋友。感謝陳老師的指導，無論是研究上的教導和討論，亦或生活上的經驗分享和指正，都讓我獲益良多。也很感謝陳老師的信任，放心的讓我使用單價非常昂貴的 laser diode stack，讓我在實驗上獲得許多別人少有的經驗。這學年當任霹靂博助教，從陳老師的上課更加體驗到物理有趣的連貫，從與學生的討論練習表達。第二位要感謝的是黃凱風 教授。感謝黃老師分享實驗上的想法及提供許多寶貴的材料，並且給予我許多的幫助及多次的推薦。兩位良師在學術上的熱忱是我學習的楷模。

剛踏入實驗室的時候，覺得實驗室的學長姐都很熱心、親切與活潑；感謝美玲、玲意(01)、亭樺(DEER)學姐們，和冠暉(老大)、國欽、聰憲、偉立(立臥)、仕璋(小黃)、哲彥(ppman)學長們營造出非常和樂的研究環境。每天都很早到實驗室的立臥傳授我一些基本雷射架設和最佳化的技巧；此外，非常感謝立臥用那台小VW 幫我搬了無數次的家，以及生活上許多的幫助。博一期間與哲彥學長學習黃光雷射，磨練了許多實驗的基本功。ppman 對研究的認真和努力，非常令我敬佩。小黃的實驗分享與討論，讓我獲得許多經驗及更瞭解一些半導體的區塊。最感謝的人之一，是我一開始最敬畏的蘇老大，直到後來親自被老大教導才健談了起來。跟細心、想法獨到、光學很強的老大一起做實驗，常會發現有趣的東西及注意到很多的小環節。感謝蘇老師 不厭其煩的指導、協助及傳授我如何做個好的實驗紀錄，都使我成長很多。Deer 學姐的表達能力及做投影片的功力、勇於嘗試的態度是我學習的目標。很感謝 Deer 對我的關心照顧與鼓勵，在異鄉可以遇到談心的朋友非常開心。雖然與 01 學姐相處的日子不多，但學姐做事的效率及能力令我見賢思齊。再來要感謝的是同窗：恩毓、建誠、興馳、雅婷、筱筑和雅莉。碩一時跟恩毓去健身房運動的日子非常愉快。感謝同為天蠍座的兩位人夫——建誠、興馳以及雅婷，生活上熱心的幫忙、課業和研究上的共同學習與成長。還有，感謝柏毅(小江)、彥廷、阿龍哥、文政、威哲、毅帆、家楨、郁仁(王牌)、毓捷、建至、昆毅、易純、啟宏、曉玲等對我大大小小的幫助。感謝悶騷的電路設計高手小江，對我

的開導與指教。特別感謝書卷高手、有點自戀的籃球王牌，無論在課業或研究上，追根究柢和認真的態度非常值得讚賞，彼此的互相切磋和討論讓我獲得很多。除了交大人，大學的好麻吉們：婉婷、怡萍、鈺淇、阿龐、育陞，謝謝你們的關心與生活的分享。

這一生最感激的就是養育、栽培我的父母，每當想起他們工作的辛苦就會更加激勵我要往前進。感謝愛問我物理問題的爸爸，在我心情低落時給我鼓勵與支持。『不管遇到什麼困難都要往上爬』是爸爸給我的一句話。感謝貼心的媽媽，時常幫我燉補及打理生活。感謝凡事替我考慮周到的好妹妹及哥哥，爺爺、奶奶、外婆、大姑、小阿姨的疼愛與照顧。家人的支持與鼓勵是我向前的動力。還要感謝從大學至今非常體貼的伴讀—小彥，八年多來細心的照料與包容真的辛苦了。Thank Andrew & Alisa for your cares! 最後，再次感謝所有幫助過我的良師益友們和我親愛的家人，有你們真好!



Contents

摘要	i
Abstract	ii
誌謝	iii
Contents	v
List of Figures	ix
List of Tables	xvii
Chapter 1	1
Introduction	
1.1 Diode-Pumped Solid-State Lasers	1
1.2 Nd-Doped Crystal Lasers	3
1.3 Passively Q-Switched Lasers	11
1.4 Nonlinear Optics	13
1.5 Overview of Thesis	16
References	18
Chapter 2	21
Diode-Pumped Nd:YAG Laser at 0.946 μm and Intracavity Frequency Doubling	
2.1 Continuous-Wave Nd:YAG Laser at 946 nm and Intracavity Frequency Doubling to 473 nm	21
2.1.1 Experimental Setup	22
2.1.2 Experimental Results and Discussion	26

2.2	Efficient Passively Q-Switched Nd:YAG Laser at 946 nm	29
2.2.1	Design of Semiconductor Saturable Absorbers	29
2.2.2	Experimental Setup	34
2.2.3	Experimental Results and Discussion	36
2.3	High-Power 946 nm Nd:YAG Laser and Blue Laser at 473 nm in QCW operation	40
2.3.1	High-Power QCW pump source	40
2.3.2	Experimental Setup	45
2.3.3	Experimental Results and Discussion	47
2.4	High-Peak-Power Passively Q-Switched Nd:YAG Laser at 946 nm	55
2.4.1	Experimental Setup	55
2.4.2	Experimental Results and Discussion	59
2.5	Conclusions	64
References		66
Chapter 3	70
	Diode-Pumped Eye-Safe Nd:YAG Laser at 1.44 μm with an Intracavity Selective Absorber	
3.1	Introduction to Eye-Safe Lasers	70
3.2	Design of Intracavity Selective Absorber	75
3.3	High-Power Continuous-Wave Nd:YAG Laser at 1.44 μm	80
3.3.1	Experimental Setup	80
3.3.2	Experimental Results and Discussion	82
3.4	Conclusions	85
References		86



Chapter 4 92

Design Models and Experiments for Millijoule Intracavity

Optical Parameter Oscillators

4.1	Introduction to Optical Parameter Oscillator (OPO)	92
4.2	Cavity Configurations of Intracavity OPOs	100
4.3	Subnanosecond Eye-Safe Intracavity OPO	102
	4.3.1 Experimental Setup	103
	4.3.2 Theoretical Analysis	106
	4.3.3 Results and Discussion	110
4.4	Analytical Model for Simultaneous Emission of Fundamental and Signal Waves	115
	4.4.1 Theoretical Analysis	117
	4.4.2 Analytical Model	121
	4.4.3 Experimental Results and Discussion	124
4.5	Efficient Intracavity OPO with an AlGaInAs Quantum-Well (QW) Saturable Absorber	133
	4.5.1 AlGaInAs QWs Saturable Absorber	134
	4.5.2 Cavity Design and Setup	137
	4.5.3 Results and Discussion	141
4.6	Conclusions	148
	References	150

Chapter 5 157

Beam-Quality Improvement of Millijoule Q-Switched Lasers with an Unstable Cavity Stabilized by Thermal-Lensing Effect

5.1	Unstable Cavity Design	157
-----	------------------------	-----

5.2	Experimental Setup	169
5.3	Results and Discussion	171
5.4	Conclusions	179
	References	180

Chapter 6 **182**

Summary and Future Work

6.1	Summary	182
6.2	Future Work	185
	References	187

Curriculum Vitae

Publication List



189

190

List of Figures

Chapter 1

- Fig. 1.2.1.** Laser transitions of trivalent rare earth. 4
- Fig. 1.2.2.** Energy levels of Nd³⁺ ions within the solid state. The details of the splitting depend on the host lattice. 5
- Fig. 1.2.3.** Energy level diagram of Nd:YAG. The solid line represents the major transition at 1064 nm, and the dashed lines are the transitions at 1319, 1338, and 946 nm. 7
- Fig. 1.2.4.** Measured results for the fluorescence spectrum of Nd³⁺ in YAG. 8
- Fig. 1.2.5.** Simplified energy level diagrams of (a) a four-level laser system and (b) a quasi-three-level laser system. N_1 and N_2 are the populations of the lower laser level and the upper laser level, respectively. 10
- Fig. 1.3.1.** Schematic illustration of (a) the repetitive Q-switching and (b) development of a Q-switched laser pulse. 12
- Fig. 1.4.1.** Schematic of second-order nonlinear processes: (a) second harmonic generation (SHG), (b) sum frequency generation (SFG), (c) different frequency generation (DFG), and (d) optical parametric generation (OPG). 15

Chapter 2

- Fig.2.1.1.** Transmittance spectrum for the entrance surface of the Nd:YAG crystal: high reflection at 946 nm ($R>99.8\%$) and high transmission at 808 nm ($T>90\%$) and 1064 nm ($T>85\%$). 24
- Fig.2.1.2.** Experimental setup for (a) diode-pumped Nd:YAG laser.; (b) diode-pumped intracavity frequency-doubled 473 nm Nd:YAG /BiBO 25

blue laser.

Fig.2.1.3.	CW average output power at 946 nm with respect to the incident pump power.	27
Fig. 2.1.4.	(a) Optical spectrum of the blue laser; (b) CW average output power at 473 nm with respect to the incident pump power.	28
Fig. 2.2.1.	The structure of the InGaAs SESAMOC.	31
Fig. 2.2.2.	Measured results for the low-intensity transmission spectrum.	32
Fig. 2.2.3.	Room-temperature photoluminescence (PL) spectrum of the InGaAs QWs saturable absorber.	33
Fig. 2.2.4.	Schematic of a diode-pumped passively Q-switched Nd:YAG laser at 946 nm.	35
Fig. 2.2.5.	The average output powers at 946 nm with respect to the incident pump power in CW and passively Q-switching operations.	37
Fig. 2.2.6.	Experimental results for pulse repetition rate and pulse energy versus incident pump power.	38
Fig. 2.2.7.	(a) Typical oscilloscope trace of a train of output pulses and (b) expanded shape of a single pulse.	39
Fig. 2.3.1.	(a) Image of the Quantel laser diode and (b) the near-field image of laser diode emitters at 30 A.	42
Fig. 2.3.2.	(a) Schematic of a lens duct with five geometric parameters of r , L , H_1 , H_2 , and H_3 : r is the radius of the input surface, L is the length of the duct, H_1 is the width of the input surface, H_2 is the width of the output surface, and H_3 is the thickness of the duct. (b) Lens duct assembly.	43
Fig. 2.3.3.	Schematic of ray tracing inside a lens duct: (a) top view in the slow-axis plane, (b) side view in the fast-axis plane.	44
Fig. 2.3.4.	Schematics of QCW diode-pumped Nd:YAG lasers at 946 nm in (a),	46

and intracavity frequency-doubling at 473 nm in (b).

- Fig. 2.3.5.** Experimental results of (a) the free-running operation for the output pulse energy at 946 nm versus the pump energy for three kinds of output surfaces of lens ducts, and (b) pulse train at the maximum pump energy. 49
- Fig. 2.3.6.** Temporal shapes of the single pulse for the lens duct output surface of (a) $2.1 \times 2.1 \text{ mm}^2$; (b) $1.6 \times 1.6 \text{ mm}^2$; (c) $1.2 \times 1.2 \text{ mm}^2$. 50
- Fig. 2.3.7.** Estimated on-time average output power at 946 nm versus the on-time average pump power in the free-running performance, for three kinds of output surfaces of lens ducts. 51
- Fig. 2.3.8.** Experimental results of the free-running operation for the output pulse energy at 473 nm versus the pump energy for three kinds of output surfaces of lens ducts. 52
- Fig. 2.3.9.** Estimated on-time average output power at 473 nm as a function of the on-time average pump power for the lens duct with an output surface of $1.2 \times 1.2 \text{ mm}^2$. 53
- Fig. 2.3.10.** Experimental results for the lens duct with an output surface of $1.2 \times 1.2 \text{ mm}^2$: (a) pulse train at the maximum pump energy of 105 mJ; (b) temporal shape of the single pulse at the maximum pump energy of 105 mJ; (c) Spatial distribution of the output blue beam recorded with a CCD. 54
- Fig. 2.4.1.** Schematic of a diode-pumped passively Q-switched Nd:YAG laser at 946 nm: (a) with the Cr^{4+} :YAG crystal as a saturable absorber; (b) with the InGaAs QWs as a saturable absorber and an output coupler. 57
- Fig. 2.4.2.** The low-intensity transmission spectrum for the InGaAs SESAMOC: transmission at 946 nm and 1064 nm are approximately 10% and 64%, respectively. 58
- Fig. 2.4.3.** Typical result of double pulses in the passively Q-switched 61

Nd:YAG/Cr⁴⁺:YAG laser at 946 nm (upper); expanded shape of each pulse (lower).

- Fig. 2.4.4.** (a) typical oscilloscope trace of a single pulse; (b) typical oscilloscope trace of triple pulses with the InGaAs QWs as a saturable absorber. 62
- Fig. 2.4.5.** 3D spatial distribution of the output beam recorded with an infrared CCD. 63
- Chapter 3**
- Fig.3.1.1.** Penetration of radiation into the eye: 1 - eye transmission to the retina, 2 - radiation absorption in the retina. 72
- Fig. 3.1.2.** Spectral transmission characteristics of the human eye. 73
- Fig.3.1.3.** Water absorption at 20 °C / penetration depth as a function of wavelength. 74
- Fig. 3.2.1.** The partial fluorescence spectrum of Nd:YAG laser crystal in the $^4F_{3/2} \rightarrow ^4I_{13/2}$ manifold. 77
- Fig. 3.2.2.** Structure of the present ISA: the absorption region including 10 groups of two 10-nm QWs with the absorption wavelength around 1.32 μm , spaced at 190-nm intervals by AlGaInAs barrier layers with the absorption wavelength around 1.06 μm . 78
- Fig. 3.2.3.** Transmittance spectrum for the developed ISA device. 79
- Fig. 3.3.1.** Experimental schematic of the laser experiment. 81
- Fig. 3.3.2.** Average output powers, with and without the ISA inserted into the cavity with the OC₁, versus the incident pump power. 83
- Fig. 3.3.3.** Average output powers, with and without the ISA inserted into the cavity with the OC₂, versus the incident pump power. 84

Chapter 4

Fig. 4.1.1.	(a) Diagram of three photons interaction in optical parameter process. (b) The energy-level diagram of the optical parameter process.	95
Fig.4.1.2.	Configurations for parametric interactions: (a) OPA; (b) SRO; (c) DRO.	96
Fig. 4.1.3.	Phase-matching configuration of OPOs: (a) type I; (b) type II.	97
Fig. 4.1.4.	(a) Angle tuning curve of type II <i>x</i> -cut KTP for a pump wavelength of 1064 nm. (b) The signal wavelength with respect to pump wavelength for type II <i>x</i> -cut KTP.	98
Fig. 4.1.5.	Wavelength coverage of Nd:YAG or Nd:YLF pumped OPOs.	99
Fig. 4.2.1.	Schematic of two kinds of configurations: (a) coupled cavity; (b) shared cavity.	101
Fig. 4.3.1.	Experimental setup for an intracavity OPO pumped by a high-power QCW diode-pumped passively Q-switched Nd:YAG laser in a shared resonator.	105
Fig. 4.3.2.	Calculated results for the dependence of the threshold photon density on the output reflectivity R_s .	109
Fig. 4.3.3.	Experimental results for the threshold pump energy versus the OPO output reflectivity.	111
Fig. 4.3.4.	Experimental results for the pulse energy of the signal output versus the OPO output reflectivity.	112
Fig. 4.3.5.	Experimental results for the temporal shapes of the fundamental and the signal pulses.	113
Fig. 4.3.6.	Experimental results for the peak power of the signal output versus the OPO output reflectivity.	114
Fig. 4.4.1.	Calculated results for the output pulse energy as a function of the reflectivity R for several values of T_0 ; solid lines: theoretical results	120

calculated from Eqs. (1)-(6); dashed lines: modeling results obtained with the analytical expressions of Eqs. (7)-(15).

- Fig. 4.4.2.** Experimental setup for an intracavity OPO pumped by a diode-pumped passively Q-switched Nd:YAG / Cr⁴⁺:YAG laser in a shared resonator. 126
- Fig. 4.4.3.** The pump threshold energy with respect to the reflectivity at the fundamental laser wavelength of 1064 nm in T₀= 50% case; solid lines: theoretical results; symbols: experimental values. 129
- Fig. 4.4.4.** Calculated and experimental results for the output pulse energy with respect to the reflectivity at the fundamental laser wavelength of 1064 nm in T₀= 50% case; solid lines: theoretical results calculated from Eqs. (1)-(6); dashed lines: modeling results obtained with the analytical expressions of Eqs. (7)-(15); symbols: experimental results. 130
- Fig. 4.4.5.** Experimentally temporal shapes of the fundamental laser (1064 nm) and OPO signal (1572 nm) pulses generated in T₀= 50% case for the reflectivity of (a) 0.998, (b) 0.98, (c) 0.94, and (d) 0.9. 131
- Fig. 4.4.6.** The output peak power as a function of the reflectivity at the fundamental laser wavelength of 1064 nm in T₀= 50% case. 132
- Fig. 4.5.1.** (a) Structure of the present AlGaInAs material; (b) transmittance spectrum at room temperature for the AR-coated AlGaInAs/InP saturable absorber. 135
- Fig. 4.5.2.** Transmittance of AlGaInAs material and Cr⁴⁺:YAG crystal as a function of the incident pulse energy fluence. 136
- Fig. 4.5.3.** Experimental schematic of the passively Q-switched Nd:YVO₄ laser with AlGaInAs QWs as a saturable absorber. 139
- Fig. 4.5.4.** Schematic diagrams of (a) a linear three-element cavity, (b) an intracavity OPO with AlGaInAs QWs as a saturable absorber in a coupled-cavity configuration. 140

Fig. 4.5.5.	Output energy at 1064 nm with respect to the incident pump energy at 808 nm for QCW free-running operation.	143
Fig. 4.5.6.	(a) Energy stability of the passively Q-switched Nd:YVO ₄ laser under a repetition rate of 200 Hz and (b) temporal shape for the passively Q-switched Nd:YVO ₄ laser with an AlGaInAs QW saturable absorber.	144
Fig. 4.5.7.	Experimental results for the output pulse energy at 1573 nm versus the OPO output reflectivity.	145
Fig. 4.5.8.	Energy stability of the Nd:YVO ₄ OPO with an AlGaInAs QW saturable absorber at a repetition rate of 50 Hz with the optimum output coupler of $R_s = 80\%$.	146
Fig. 4.5.9.	(a) Typical oscilloscope trace of a train of the laser and OPO pulses with $R_s = 80\%$; (b) temporal shapes of the laser and OPO pulses with $R_s = 80\%$.	147

Chapter 5

Fig. 5.1.1.	Schematic of (a) an unstable resonator configuration; (b) an unstable resonator with an internal lenslike laser rod; (c) an unstable resonator for a passively Q-switched laser with an internal lenslike laser rod and a Cr ⁴⁺ :YAG crystal.	160
Fig. 5.1.2.	Calculated results for the dependence of (a) the mode size and (b) the mode-size gradient on the thermal focal length.	164
Fig. 5.1.3.	The laser spot radius $w(z)$ varied along the laser propagation for various values of the thermal focal length f for this present unstable cavity configuration.	165

Fig. 5.1.4.	(a) Schematic of the extracavity backward laser beam transformation, propagating along z_2 for the present cavity configuration; (b) the calculated results of the dependence of extracavity backward laser beam on position z_2 for several thermal focal lengths f .	166
Fig. 5.1.5.	(a) Schematic of the extracavity forward laser beam transformation, propagating along z_1 for the present cavity configuration; (b) the calculated results of the dependence of extracavity forward laser beam on position z_1 for several thermal focal lengths f .	168
Fig. 5.2.1.	Experimental setups of (a) the diode-side-pumped Nd:YAG laser in free-running operation; (b) the diode-side-pumped passively Q-switched Nd:YAG laser with a Cr ⁴⁺ :YAG crystal placed near the output coupler and (c) with a Cr ⁴⁺ :YAG crystal placed near the front mirror.	170
Fig. 5.3.1.	Output energy at 1064 nm with respect to the incident pump energy at 808 nm for QCW free-running operation.	173
Fig. 5.3.2.	Temporal characteristics of the Q-switched pulse in (a) and the expanded modulated pulse in (b).	174
Fig. 5.3.3.	Temporal characteristics of the Q-switched pulse: (a) (T_0 , R) = (30%, 70%), (b) (T_0 , R) = (40%, 60%).	178
Chapter 6		
Fig. 6.2.1.	Room-temperature emission spectrum of an a-cut Nd:LuGdVO ₄ and the partial region around 1.8-1.09 μm shown in (b).	186

List of Tables

Chapter 1

- Tab. 1.2.1.** The stimulated-emission cross section of the various laser transitions in Nd:YAG at room temperature 9

Chapter 3

- Tab. 3.3.1.** The employed OCs coatings with different reflectivities at 1.06, 1.32, and 1.44- μm , respectively. 81

Chapter 5

- Tab. 5.3.1.** Experimental results of passively Q-switched operations with a Cr^{4+} :YAG crystal posited to be adjacent to the high-reflection front mirror. 177

Chapter 1

Introduction

1.1 Diode-Pumped Solid-State Lasers

Solid-state lasers are attractive sources of coherent radiation for various scientific, medical, industrial, and military applications. Major advances in solid-state laser technology have historically been preceded by advances in pumping technology. In early stages, high-pressure noble-gas discharge lamps are typically used in solid-state lasers. Krypton and xenon are the two noble gases most commonly used in the laser lamp systems, Kr arc lamp and Xe flashlamp. Xenon is the typical used material because of its higher radiation density than the other noble gases for a given electric input. However, since flashlamps are broadband sources, they produce unprofitable radiation which generates unwanted heat and consume a large amount of electric power. As development of semiconductor lasers, laser-diode pumped solid-state lasers were demonstrated much soon.

Compared with laser lamps, diode lasers provide an excellent match to the laser pump bands and improved pump source lifetime; therefore, diode lasers possess much advantages of higher overall efficiency, reduced thermal loading of gain medium, smaller size and less weight, and higher system reliability. Fiber-coupled LD is the favorite candidate for SSL since it has circular, symmetric and homogenized intensity profile. For these reasons, diode-pumped solid-state lasers have shown promise for use in present. Two basic approaches have been used to optically pump laser crystals: end pumping and side pumping. End pumping has the potential to yield

high-efficiency and high-beam-quality lasers, provided that the diode laser array emitting area can be matched to the intracavity laser mode size.

Contrary to the conventional high power diode pumped systems based on a low power continuously diode pumped oscillator, the systems pumped by two dimensional laser diode stacks give potential to generate more energetic (milijoule level) nanosecond and picosecond pulses directly from laser oscillator. Milli-joule (mJ) lasers with QCW pumping have different applications from micro-joule (μJ) lasers with CW pumping. For example, military systems such as rangefinders and target designators require pulse energy of 10-200 mJ and pulse width of 10-20 ns [3]. Besides, there are another potential applications of diode-pumped solid-state lasers such as coherent radar, global sensing from satellites, medical uses, micromachining, and miniature visible sources for digital optical storage.



1.2 Nd-Doped Crystal Lasers

Rare earth ions (13 elements, from Ce to Yb) exhibit many sharp fluorescent transitions, and therefore they serve as active ions in solid-state lasers. **Fig. 1.2.1** illustrates laser transitions of trivalent rare earth [1]. The rare-earth metals are usually triply ionized to be impurity ions, with 4f electrons [2]. The electronics states are described by LS coupling and Hund's rules. An example of popular neodymium Nd^{3+} is shown in **Fig. 1.2.2**. The active atoms experience the local electric field generated by the host lattice and thus these levels are shifted by the electric field at the site where the rare earth resides (the Stark effects).

There are two major classes of host materials in solid-state lasers, isotropic (primary various glasses, mostly silicates and phosphates) and crystalline ones (ex: YAG). In all these media (except for some glasses), the neodymium dopant ions replace other ions (often yttrium) of the host medium, which have about the same size. By the way, there are two important differences between glass and crystal lasers: first, is that glass hosts have lower thermal conductivity than the most crystal ones; second, the emission lines of ions in glasses are broader than in crystals. For continuous and very high repetition rate laser systems, crystalline host materials provide higher gain and greater thermal conductivity [3].

Nd^{3+} lasers have been investigated for more than 40 years and have been established as probably the most common near-infrared lasers. The common neodymium-doped gain media are Nd:glass, Nd:YAG, Nd:YVO₄, Nd:YLF, Nd:YAP, Nd:YALO, Nd:GdVO₄, and some mixed crystals. Among the crystals, Nd:YAG crystals have been most widely used in all-solid-state lasers because of their excellent optical properties and high thermal conductivity [3-5].

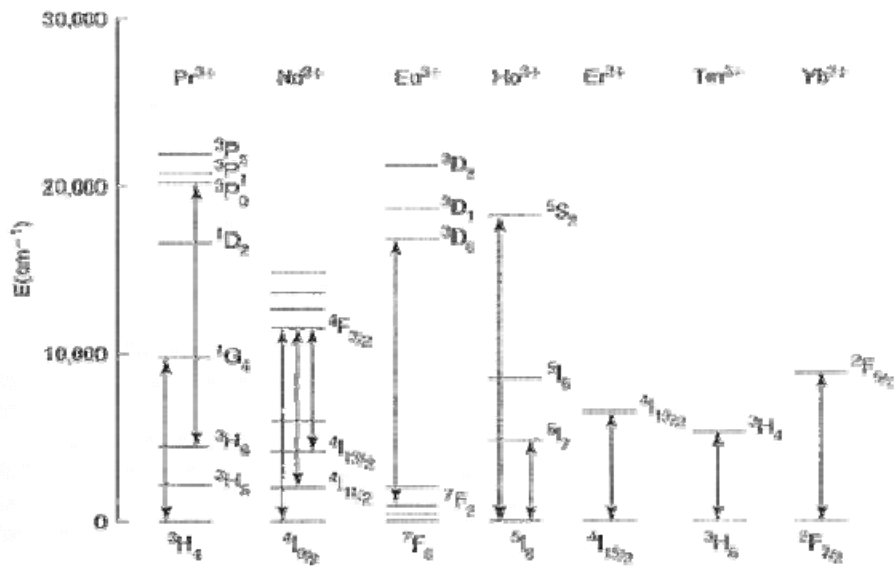


Fig. 1.2.1. Laser transitions of trivalent rare earth [1].

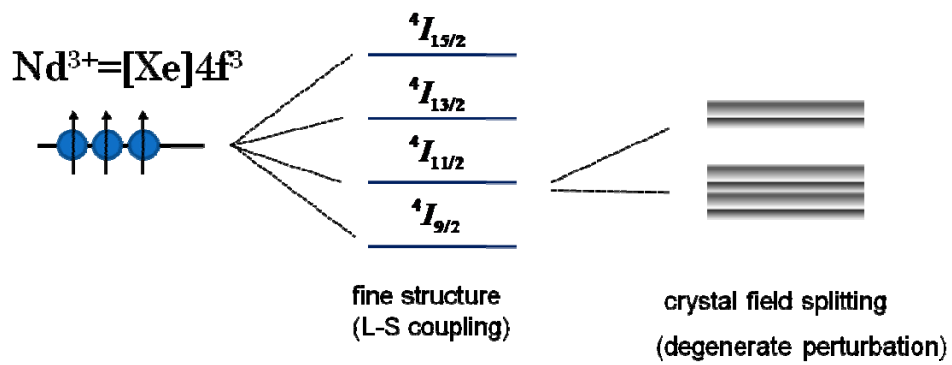


Fig. 1.2.2. Energy levels of Nd^{3+} ions within the solid state. The details of the splitting depend on the host lattice [2].

The energy levels of the rare-earth elements (Nd³⁺) split into a number of Stark levels due to the action of the crystal field. The electron transition corresponding to each Stark level emits a different wavelength. **Fig. 1.2.3** depicts the energy level diagram of Nd:YAG laser medium and Stark splitting of the manifolds are shown. Laser transition lines of 946, 1064, 1319, and 1338 nm are indicated. The laser transitions occur between the individual Stark sublevels of different manifolds.

Figure 1.2.4 shows the measured results for the fluorescence spectrum of Nd³⁺ in YAG with the corresponding energy levels for the various transitions. It can be clearly seen Nd³⁺ in YAG additionally provides the long wavelengths end of the ${}^4F_{3/2} \rightarrow {}^4I_{13/2}$ transition around 1.41–1.44 μm . The effective stimulated-emission cross section is the spectroscopic cross section times the occupancy of the upper laser level relative to the entire ${}^4F_{3/2}$ manifold population. In 1974, Singh *et al.* have been measured the stimulated-emission cross section at room temperature [6], as listed in **Tab. 1.2.1**. In Nd:YAG crystal, the 1064 nm transitions ${}^4F_{3/2} \rightarrow {}^4I_{11/2}$ have the highest emission cross sections at room temperature. Several low-gain transitions, one at 946 nm and two at 1.3 μm , are of particular interest in Nd:YAG because frequency doubling of these wavelengths is attractive for generating visible lasers in the blue and red region. Other low-gain transitions at around 1.44 μm are of particular interest in the eye-safe laser range. To achieve these low-gain transitions, parasitic oscillations at the higher gain transitions have to be suppressed.

It is worth mentioning that the laser operating at 946 nm emission is termed a quasi-three-level laser. Since the lower laser level is only $\sim 4 kT$ (853 cm^{-1}) above the ground state [6], there is a thermal population of about 0.7% at room temperature [3]. This residual population results in a partial reabsorption loss of the laser radiation which increases the laser threshold. Simplified energy level diagrams of a four-level laser and a quasi-three-level laser are depicted in **Fig. 1.2.5**. In a four-level system, the lower laser level is above the ground state by an energy gap $E \gg k_b T$, and therefore is not thermally populated. Compared to the four-level lasers, the quasi-three-level and three-level lasers require high pump intensities to generate population inversion.

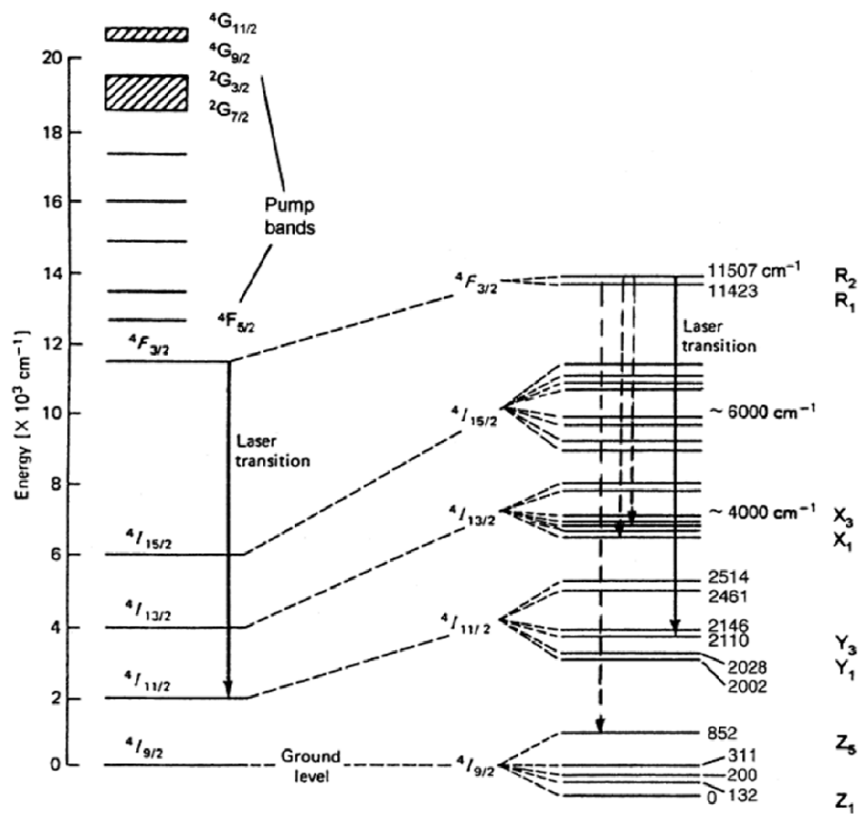


Fig. 1.2.3. Energy level diagram of Nd:YAG. The solid line represents the major transition at 1064 nm, and the dashed lines are the transitions at 1319, 1338, and 946 nm [3].

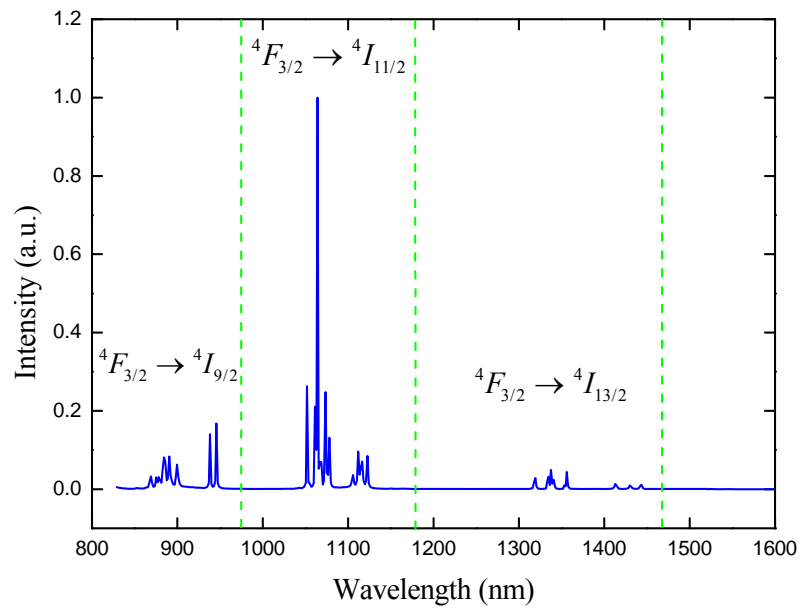


Fig. 1.2.4. Measured results for the fluorescence spectrum of Nd³⁺ in YAG.

Wavelength (nm)	Laser transitions	Cross section (10^{-20} cm^2)
946.1	${}^4F_{3/2} \rightarrow {}^4I_{9/2}$, ($R_1 \rightarrow Z_5$)	0.5
1064.18	${}^4F_{3/2} \rightarrow {}^4I_{11/2}$, ($R_2 \rightarrow Y_3$)	45.8
1318.8	${}^4F_{3/2} \rightarrow {}^4I_{13/2}$, ($R_2 \rightarrow X_1$)	8.7
1338.2	${}^4F_{3/2} \rightarrow {}^4I_{13/2}$, ($R_2 \rightarrow X_3$)	9.2
1414.0	${}^4F_{3/2} \rightarrow {}^4I_{13/2}$, ($R_2 \rightarrow X_6$)	3.3
1430.8	${}^4F_{3/2} \rightarrow {}^4I_{13/2}$, ($R_1 \rightarrow X_6$)	2.3
1444.0	${}^4F_{3/2} \rightarrow {}^4I_{13/2}$, ($R_1 \rightarrow X_7$)	3.4

Tab. 1.2.1. The stimulated-emission cross section of the various laser transitions in Nd:YAG at room temperature [6].

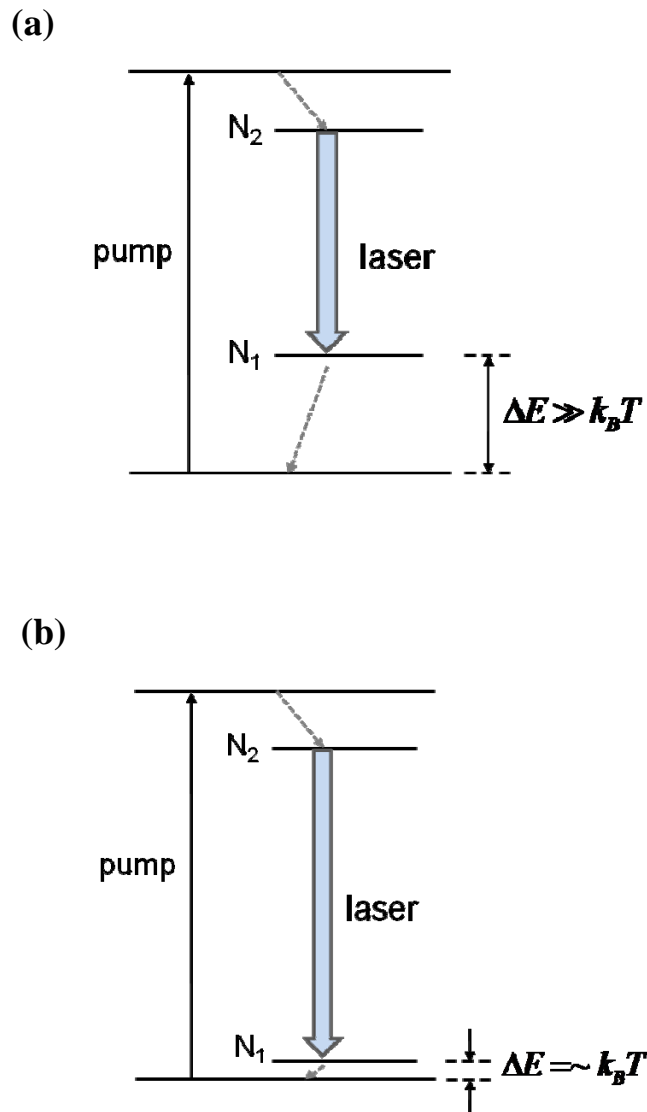


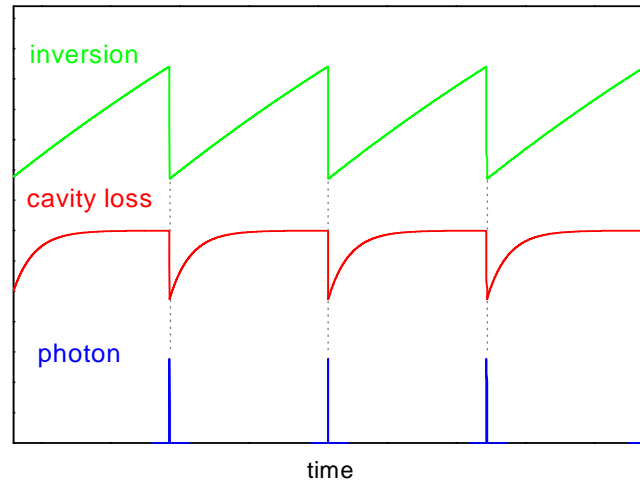
Fig. 1.2.5. Simplified energy level diagrams of (a) a four-level laser system and (b) a quasi-three-level laser system. N_1 and N_2 are the populations of the lower laser level and the upper laser level, respectively.

1.3 Passively Q-Switched Lasers [3]

Q switching is a technique for the generation of nanosecond pulses of high energy and peak power laser pulses by modulating the Q factor of the laser resonator with a saturable absorber. **Fig. 1.3.1** shows the generation of a Q-switched laser pulse. Laser inversion is built up by the pumping process and laser oscillation begins to develop inside the cavity. While the laser oscillation saturates the absorber, the cavity is opened up. Simultaneously, the laser inversion exceeds the cavity losses, and then a short pulse is rapidly emitted. The Q-switched pulse duration is typically in the nanosecond range, corresponding to several cavity round trips.

Passively Q-switched (PQS) lasers are of many practical applications such as laser ranging, laser cutting and drilling, and nonlinear optical studies. Passive Q-switching that uses an internal saturable absorber has the advantages of simplicity, compactness, and low cost, and requires no external driving circuitry. Numerous saturable absorbers have been developed, such as dyes [7], LiF:F₂-color center crystals [8,9], and Cr⁴⁺:YAG crystals [10-16]. Nowadays, Cr⁴⁺:YAG crystal is the popular saturable absorber in the spectral region of 0.9–1.2 μm. Because of its better thermo-mechanical properties, stability, reliability and simplicity, it is especially suitable for all-solid-state laser systems. An attractive alternative is the use of semiconductor saturable absorbers which saturation fluence and maximum modulation depths can be flexibly designed, and they can be adapted to different laser wavelengths. To date, semiconductor saturable absorbers have been demonstrated as useful devices for solid-state lasers [17-20].

(a)



(b)

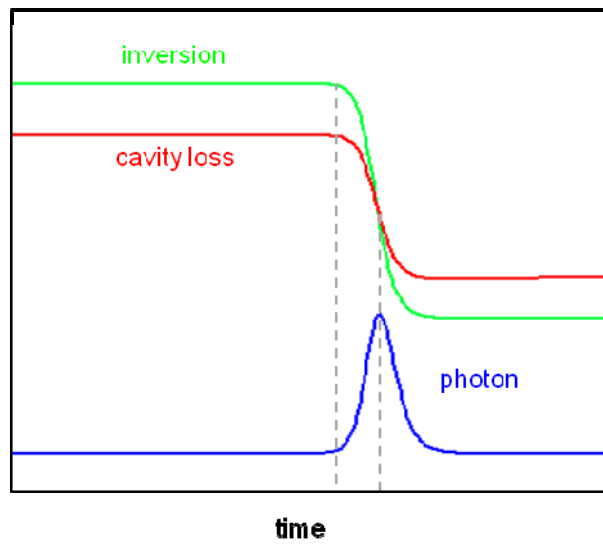


Fig. 1.3.1. Schematic illustration of (a) the repetitive Q-switching and (b) development of a Q-switched laser pulse.

1.4 Nonlinear Optics^[21,22]

A nonlinear optical effect can occur when the electric field \vec{E} of electromagnetic wave is increased significantly to induce nonlinearity in the polarization vector \vec{P} in a material. The relationship between P and the applied electric field E is expressed

$$P = \epsilon_0 \chi^{(1)} E + \epsilon_0 \chi^{(2)} E^2 + \epsilon_0 \chi^{(3)} E^3 + \dots \quad (1)$$

where ϵ_0 is the permittivity of free space and $\chi^{(1)}$ is the linear susceptibility representing the linear response of the material. The other terms describe the nonlinear response of the medium. The term in E^2 is called the second-order nonlinear response and $\chi^{(2)}$ is called the second-order nonlinear susceptibility. Similarly, the term in E^3 is called the third-order nonlinear response and $\chi^{(3)}$ is called the third-order nonlinear susceptibility.

The magnitudes of the nonlinear susceptibility coefficients are such that the second- and third-order polarizations become comparable to the linear polarization term $P_1 = \epsilon_0 \chi^{(1)} E$ when the applied electric field E is of the order of the electric field produced between the electron and proton of a hydrogen atom, $E \approx e / (4\pi\epsilon_0 a_H^2)$, where e is the electron charge, a_H is the radius of the electron orbit. $\chi^{(2)}$ and $\chi^{(3)}$ are of the order of

$$\chi^{(2)} \approx 2 \times 10^{-11} \text{ m/V} \quad (2)$$

and

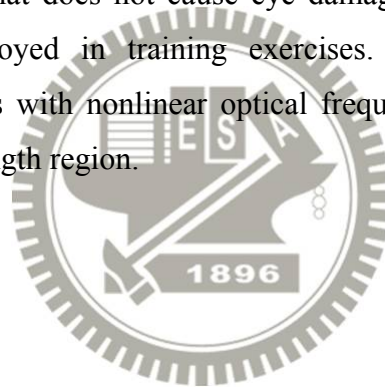
$$\chi^{(3)} \approx 4 \times 10^{-23} \text{ m/V} \quad (3)$$

respectively [22].

Numerous nonlinear processes that use laser radiation to generate new frequencies of coherent light and produce other interesting nonlinear effects. Second-order nonlinear phenomena related to $\chi^{(2)}$ describe three-wave mixing processes, including second harmonic generation (SHG), sum frequency generation

(SFG), different frequency generation (DFG), and optical parametric generation (OPG). Second harmonic generation is a special case of sum frequency generation. **Figure 1.4.1** depicts the second-order nonlinear processes. The third order nonlinearities involved $\chi^{(3)}$ is thus four-wave mixing processes, including third harmonic generation, optical Kerr effect, Raman effect, and Brillouin scattering.

Not all wavelength regions of interest are directly accessible with lasers. Nonlinear frequency conversion is an important method of extending the frequency range of available laser sources. Many industrial, medical, and military applications require a different wavelength than the fundamental output available from standard lasers. Medical applications require solid-state lasers operating in a specific spectral range for control of the absorption depth of the radiation in the skin, tissue, or blood vessels. Military rangefinders need to operate in a region (wavelength $> 1.5 \mu\text{m}$) that does not cause eye damage because most of the time these systems are employed in training exercises. Therefore, diode-pumped solid-state laser combines with nonlinear optical frequency conversion technology will extend wider wavelength region.



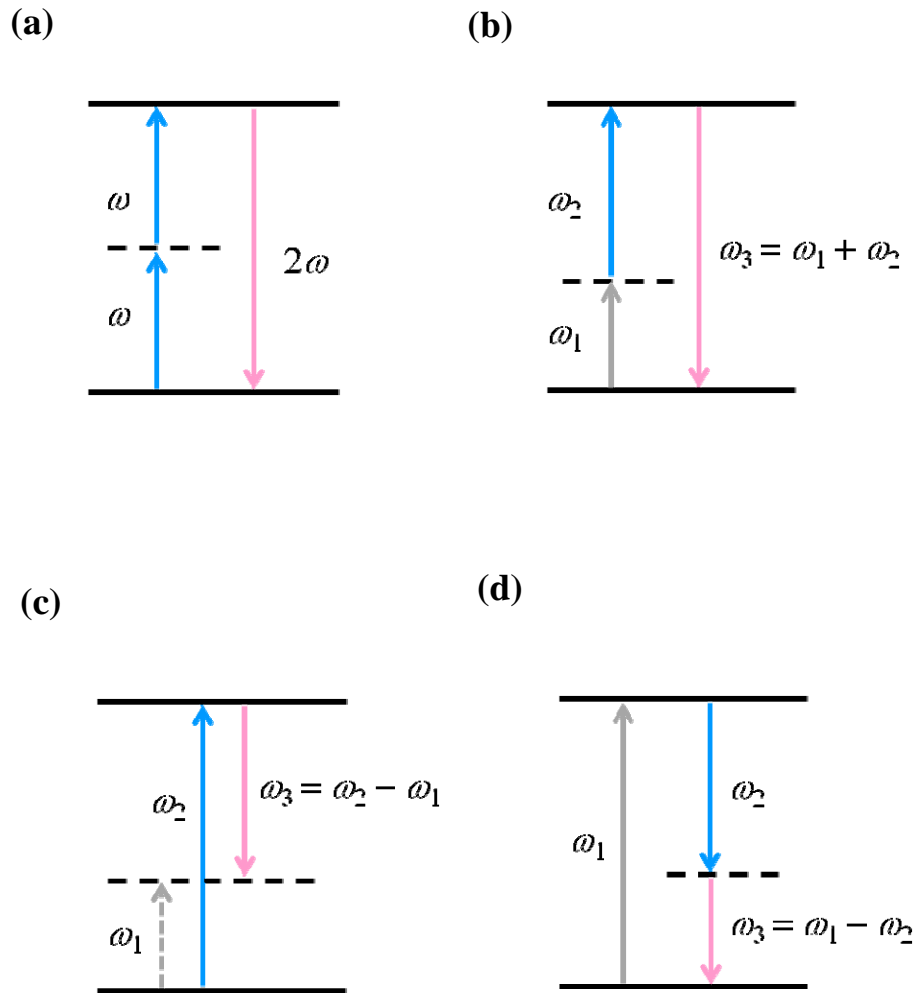


Fig. 1.4.1. Schematic of second-order nonlinear processes: (a) second harmonic generation (SHG), (b) sum frequency generation (SFG), (c) different frequency generation (DFG), and (d) optical parametric generation (OPG).

1.5 Overview of Thesis

In the thesis, various laser emissions in Nd-doped crystals and wavelength conversion with nonlinear optics are the main goal. Besides, high-pulse-energy lasers generation is an additional goal. Therefore two pump source, including CW fiber-coupled laser diode and QCW two dimensional laser diode stacks, are used in laser experiments. The main text of this thesis is organized as following.

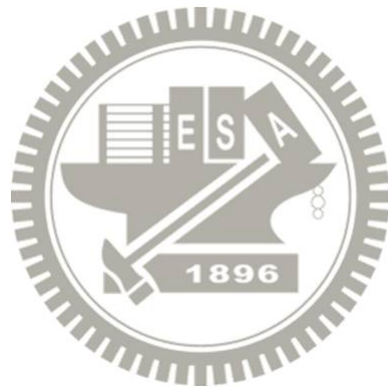
Laser operation on the transition ${}^4F_{3/2} \rightarrow {}^4F_{9/2}$ of Nd^{3+} ions generates wavelengths of 910 to 950 nm and allows for SHG into the blue spectrum region. End pumping is especially good for quasi-three-level operation, because of the high pump intensity in laser crystal. In chapter 2, we realize a quasi-three-level 946 nm Nd:YAG laser and blue light generation at 473 nm by intracavity frequency doubling. For the low gain Nd:YAG laser at 946 nm, we develop a semiconductor quantum-wells saturable absorber with low nonsaturable losses. Furthermore, we make a thorough comparison for the 946-nm passively Q-switched performance between the saturable absorbers of the semiconductor quantum-wells saturable absorber and the Cr^{4+} :YAG crystal. In order to generate a higher-power 946 nm Nd:YAG laser and a blue light at 473 nm, a high-power quasi-continuous-wave (QCW) diode stack is used as a pump source.

SESAM is not only used to be an absorber element for passively Q-switched laser, but also to be a novel intracavity selective absorber (ISA) used for suppressing high-gain lines. In chapter 3, we report an ISA with an AlGaInAs QW-barrier structure grown on a Fe-doped InP transparent substrate. With the novel ISA, an efficient high-power Nd:YAG laser at 1.44 μm is successfully realized.

Nd^{3+} -doped lasers operating at 1.0 μm have been maturely developed for many years and possess superior performances. In chapter 4, eye-safe wavelength is obtained from Nd^{3+} -doped lasers that are wavelength-shifted with an optical parametric oscillator (OPO). Efficient eye-safe lasers with mJ pulse energy are studied for military requirement. We theoretically and experimentally study the output performance of an intracavity OPO in a shared cavity configuration. Besides, we present an analytical design model to investigate the dynamics of simultaneous

emission of fundamental and signal waves. Furthermore, we design an AlGaInAs QW material with a low nonsaturable loss and large modulation strength to be a saturable absorber used in an intracavity Nd:YVO₄/KTP optical parametric oscillator.

In the previous chapter, a plane-parallel configuration generates a high-energy laser but leads to a large beam divergence and poor beam quality. In chapter 5, to improve the beam quality and accomplish efficient energy extraction, we design an unstable convex-concave resonator stabilized by thermal-lensing effect to generate a large fundamental mode volume in a passively Q-switched laser. By using ABCD law and the complex beam parameter q , the laser mode size is analyzed. Based on the unstable cavity, a passively Q-switched Nd:YAG/ Cr⁴⁺:YAG laser with a large fundamental mode volume and good beam quality is experimentally confirmed.



References

- [1] Z. J. Kiss, and R. J. Pressley, "Crystalline solid lasers," *Appl. Opt.* **5**, 1474-1486 (1966).
- [2] D. Meschede, *Optics, light and lasers: the practical approach to modern aspects of photonics and laser physics*, Physics Textbook, first ed., (Wiley-VCH, Weinheim, 2004)
- [3] W. Koechner, *Solid-state laser engineering*, Optical Sciences, 6th ed., (Springer, Berlin, 2006).
- [4] Y. Kaneda, M. Oka, H. Masuda, and S. Kubota, "7.6 W of continuous-wave radiation in a TEM₀₀ mode from a laser-diode end-pumped Nd:YAG laser," *Opt. Lett.* **17**, 1003-1005 (1992).
- [5] T. Kellner, F. Heine, and G. Huber, "Efficient laser performance of Nd:YAG at 946 nm and intracavity frequency doubling with LiJO₃, -BaB₂O₄, and LiB₃O₅," *Appl. Phys. B* **65**, 789-902 (1997).
- [6] S. Singh, R. G. Smith, and L. G. Van Uitert, "Stimulated-emission cross section and fluorescent quantum efficiency of Nd³⁺ in yttrium aluminum garnet at room temperature," *Phys Rev B* **10**, 2566-2572 (1974).
- [7] S. Y. Lam, and M. J. Damzen, "Characterisation of solid-state dyes and their use as tunable laser amplifiers," **77**, 577-584 (2003).
- [8] A. G. Kalinstev, A. A. Mak, L. N. Soms, A. I. Stepanov, and A. A. Tarasov, "Residual losses in passive shutters made from Li crystals with color centers," *Sov. Phys. Tech. Phys.* **26**, 1267-1268 (1981).

- [9] T. T. Basiev, S. V. Vassiliev, V. A. Konjushkin, and V. P. Gapontsev, "Pulsed and cw laser oscillations in LiF : F-2(-) color center crystal under laser diode pumping," *Opt. Lett.* **31**, 2154-2156 (2006).
- [10] Y. F. Chen, S. W. Tsai, and S. C. Wang, "High-power diode pumped Q-switched and mode-locked Nd:YVO₄ laser with a Cr⁴⁺:YAG saturable absorber," *Opt. Lett.* **25**, 1442-1444 (2000).
- [11] J. Liu, J. M. Yang, and J. L. He, "High repetition rate passively Q-switched diode-pumped Nd:YVO₄ laser," *Opt. Laser Technol.* **35**, 431-434 (2003).
- [12] Y. Kalisky, "Cr⁴⁺-doped crystals: their use as lasers and passive Q switches," *Prog. Quantum Electron.* **28**, 249-303 (2004).
- [13] H. Chen, E. Wu, and H. P. Zeng, "Comparison between a-cut and off-axially cut Nd:YVO₄ lasers passively Q-switched with a Cr⁴⁺:YAG crystal," *Opt. Commun.* **230**, 175-180 (2004).
- [14] A. Sennaroglu, U. Demirbas, S. Ozharar, and F. Yaman, "Accurate determination of saturation parameters for Cr⁴⁺-doped solid-state saturable absorbers," *J. Opt. Soc. Am. B* **23**, 241-249 (2006).
- [15] S. Forget, F. Druon, F. Balembos, P. Georges, N. Landru, J.-P. Fève, J. Lin, and Z. Weng, "Passively Q-switched diode-pumped Cr⁴⁺:YAG/Nd³⁺:GdVO₄ monolithic microchip laser," *Opt. Commun.* **259**, 816-819 (2006).
- [16] A. R. Bijanzaden, and R. Khordad, "Study of output energy of Cr⁴⁺:YAG passively Q-switched Nd:YAG laser: using different setup," *Opt. Commun.* **282**, 2595-2603 (2009).
- [17] G. J. Spühler, R. Paschotta, R. Fluck, B. Braun, M. Moser, G. Zhang, E. Gini, and U. Keller, "Experimentally confirmed design guidelines for passively

- Q-switched microchip lasers using semiconductor saturable absorbers,” J. Opt. Soc. Am. B **16**, 376-388 (1999).
- [18] R. Häring, R. Paschotta, R. Fluck, E. Gini, H. Melchior, and U. Keller, “Passively Q -switched microchip laser at 1.5 μm ,” J. Opt. Soc. Am. B **18**, 1805-1812 (2001).
- [19] G. J. Spühler, S. Reffert, M. Haiml, M. Moser, and U. Keller, “Output-coupling semiconductor saturable absorber mirror,” Appl. Phys. Lett. **78**, 2733-2735 (2001).
- [20] B. Y. Zhang, G. Li, M. Chen, G. J. Wang, and Y. G. Wang, “Passively Q-switched Nd :GdVO₄ laser with In_{0.25}Ga_{0.75}As being an output coupler,” Opt. Laser Technol. **39**, 1094-1097 (2007).
- [21] M. Fox, *Quantum optics: an introduction*, Atomic, Optical, and Laser Physics, first ed., (Oxford, New York, 2006).
- [22] W. T. Silfvast, *Laser Fundamentals*, Optics, 2 nd ed., (Cambridge, New York, 2004).

Chapter 2

Diode-Pumped Nd:YAG Laser at 0.946 μm and Intracavity Frequency Doubling

2.1 Continuous-Wave Nd:YAG Laser at 946 nm and Intracavity Frequency Doubling to 473 nm

Fan and Byer first demonstrated the quasi-three-level laser operating at 946 nm [1]. The $4F_{3/2} \rightarrow 4I_{9/2}$ transition has its lower laser level in the thermally populated ground state, which is only 4 kT above the ground state at room temperature [2], leading to temperature-dependent reabsorption losses. In addition, the stimulated emission cross section of 946 nm is smaller than 1064 nm (around 9 times). Nd-doped lasers around 0.9 μm are much attractive for frequency doubling into the blue range. The second-harmonic generation of continuous-wave (cw) 946-nm lasers is useful for applications such as holography, optical data storage, and color displays.

Various nonlinear crystals are utilized for the frequency-doubling of the 946-nm Nd:YAG lasers, such as KN (KNbO_3), PPKTP (periodically poled KTiOPO_4), LBO (LiB_3O_5), BBO ($\beta\text{-BaB}_2\text{O}_4$), and BiBO (BiB_3O_6) [3-8]. Among biaxial crystals, BiBO crystal has a high optical damage threshold and many advantages for nonlinear optics, such as large effective nonlinear coefficient, large angular and spectral acceptance bandwidths, and broadband angle tuning at room temperature [9]. The

most important is that BiBO crystal is non-hygroscopic, and therefore it is favorable for many optical devices and applications.

2.1.1 Experimental Setup

The active medium was 1.1 at.% Nd:YAG crystal with a length of 2.0 mm. Since a short crystal length was used to reduce the reabsorption losses, only approximately 52% of the pump light was absorbed in the gain medium. In order to shorten the cavity length, the entrance surface of the laser crystal was coated to be high reflection at 946 nm ($R > 99.8\%$) and high transmission at 808 nm ($T > 90\%$) and 1064 nm ($T > 85\%$). The other surface of the laser crystal was coated for antireflection at 946 nm ($R < 0.2\%$). Note that for this low-gain 946 nm laser, tough coating is demanded to suppress the competing transition lines of 1064 nm and 1320 nm. The transmittance spectrum for the entrance surface of the Nd:YAG crystal is shown in **Fig. 2.1.1**.

Figure 2.1.2 (a) shows the schematic diagram of cw 946 nm Nd:YAG laser. The pump source was a 10-W 808-nm fiber-coupled laser diode with a core diameter of 600 μm and a numerical aperture of 0.16. Focusing lens with 5 mm focal length and 92% coupling efficiency was used to re-image the pump beam into the laser crystal. The pump spot radius was approximately 160 μm . The output couplers were flat and coated for high transmission at 1064 nm ($T > 90\%$) and partial reflection at 946 nm ($R = 97\%$, 96% and 93%, respectively). The cavity length was approximately 10 mm.

Figure 2.1.2(b) shows the experimental configuration of cw intracavity frequency-doubled Nd:YAG laser. The frequency doubler we used was a $2 \times 2 \times 5 \text{ mm}^3$ BiBO crystal, which is cut for type-I critical phase-matching ($\theta = 161.7^\circ$, $\phi = 90^\circ$). Both facets of the BiBO crystal were coated for anti-reflection at 946 and 473 nm ($R < 0.2\%$) to reduce the reflection loss in the cavity. The laser crystals were wrapped with indium foil and mounted in a water-cooled copper block. A plano-concave mirror of 50 mm radius was chosen to be the output coupler coated for high reflection at 946 nm ($R > 99.8\%$), high transmission at 1064 nm ($T > 70\%$), and high transmission

at 473 nm ($T > 80\%$), respectively. The cavity length was approximately 30 mm.



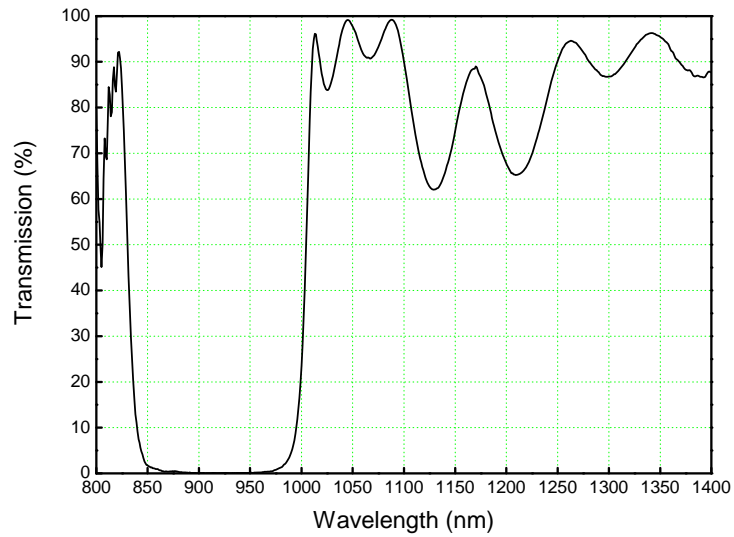


Fig.2.1.1. Transmittance spectrum for the entrance surface of the Nd:YAG crystal: high reflection at 946 nm ($R > 99.8\%$) and high transmission at 808 nm ($T > 90\%$) and 1064 nm ($T > 85\%$).

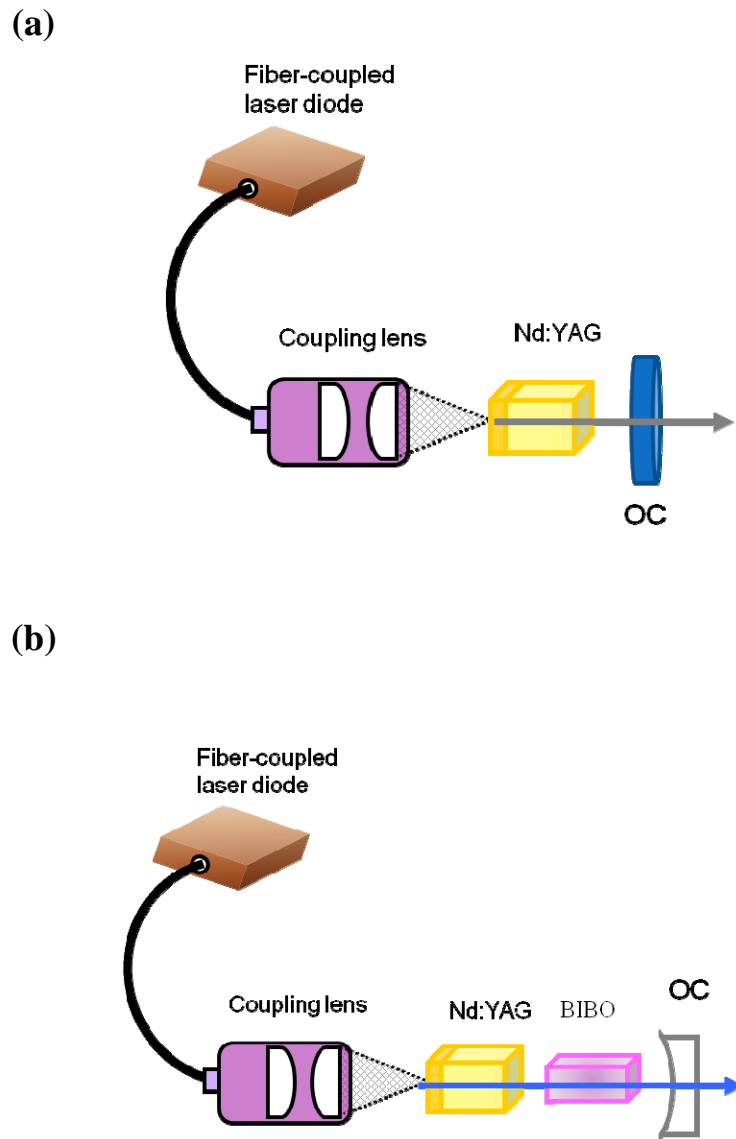
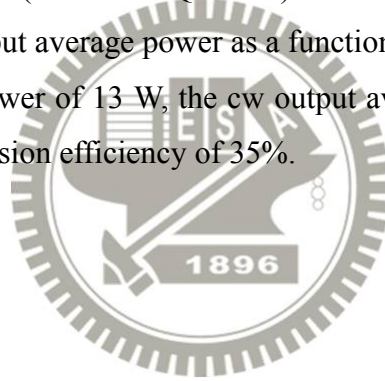


Fig.2.1.2. Experimental setup for (a) diode-pumped Nd:YAG laser.; (b) diode-pumped intracavity frequency-doubled 473 nm Nd:YAG /BiBO blue laser.

2.1.2 Experimental Results and Discussion

First of all, the 946-nm cw laser was performed to confirm the quality of the laser crystal. **Fig. 2.1.3** plots the cw average output power at 946 nm with respect to the incident pump power at 808 nm. It could be seen that the slope efficiency of three output couplers are nearly similar to be 18%. The optimal output reflectivity for cw output power is 97%. At an incident power of 19.6 W, the maximum output power can be up to 3 W with an optical-to-optical conversion efficiency of 15%.

Employing the above-mentioned plano-concave mirror of 50 mm radius, the second harmonic generation (SHG) of 946-nm laser with a BiBO crystal was performance. **Fig. 2.1.4 (a)** shows the spectral information of the laser monitored by an optical spectrum analyzer (Advantest Q8381A) with the resolution of 0.1 nm. **Fig. 2.1.4 (b)** shows the cw output average power as a function of the incident pump power at 808 nm. At a pump power of 13 W, the cw output average power at 473 nm was 0.75 W, with a SHG conversion efficiency of 35%.



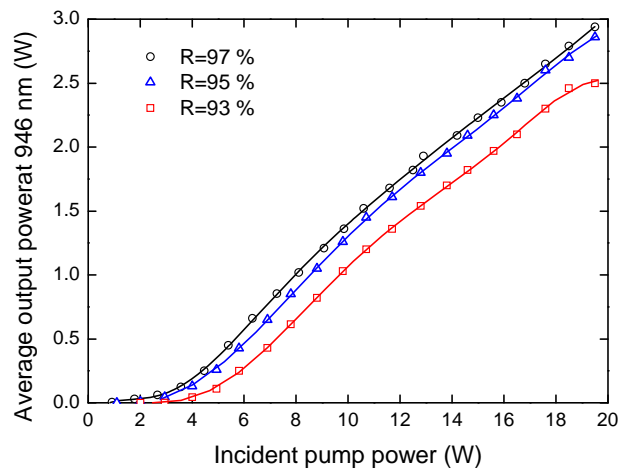
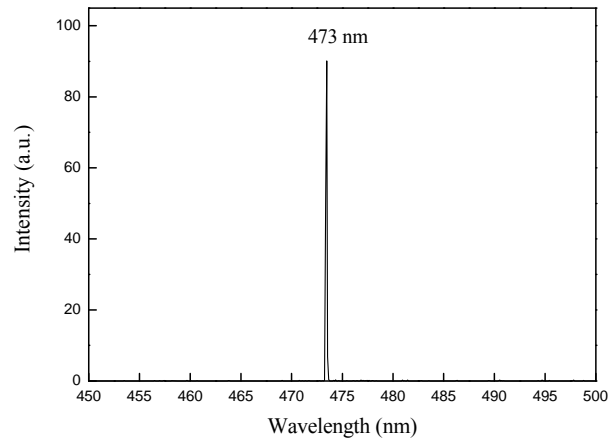


Fig. 2.1.3. CW average output power at 946 nm with respect to the incident pump power.

(a)



(b)

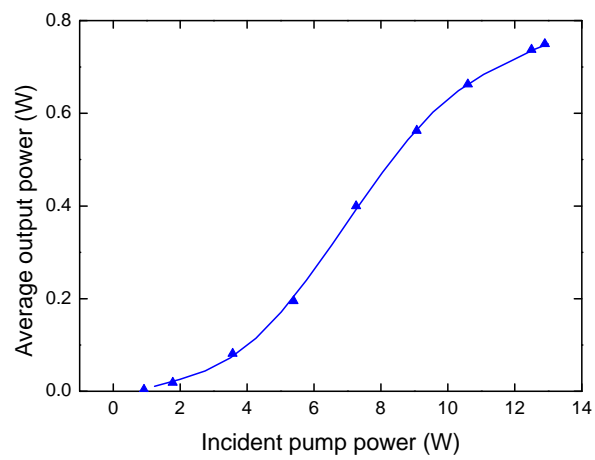


Fig. 2.1.4. (a) Optical spectrum of the blue laser; (b) CW average output power at 473 nm with respect to the incident pump power.

2.2 Efficient Passively Q-Switched Nd:YAG Laser at 946 nm

Passively Q-switched all-solid-state lasers are of great interest because of their potential applications in remote sensing, ranging, micromachining, and nonlinear wavelength conversion. The majority of the work on the Nd:YAG crystal were focused on the ${}^4F_{3/2} \rightarrow {}^4I_{11/2}$ transition in the 1064-nm range. Nevertheless, the lasing wavelength near 946 nm in the ${}^4F_{3/2} \rightarrow {}^4I_{9/2}$ transition has attracted much attention during the last decade [10-17], since it is of interest for second-harmonic generation into the blue region. Kellner et al. employed a Cr^{4+} :YAG crystal as a saturable absorber in a passively Q-switched 946-nm Nd:YAG laser to achieve as much as 1.6-W average output power with pulse width of 70-100 ns [12]. Recently, Zhang et al. demonstrated an average output power of 2.1 W with pulse width of 40.8 ns by using a Nd, Cr:YAG saturable absorber [13]. More recently, Wang et al. used a GaAs saturable absorber to obtain an average output power of 1.24 W with pulse width of 70 ns [14]. However, so far the overall Q-switching efficiencies (ratio of the Q-switched average output power to the cw output power at the same pump power) were in the range of 30-50%. The low Q-switching efficiencies arise from the nonsaturable losses of the saturable absorbers. Since the gain of the Nd:YAG crystal at 946 nm is quite low, a small amount of nonsaturable losses may lead to a considerable reduction in the efficiency. In view of that, it is of practical usefulness to develop a saturable absorber with low nonsaturable losses for the low gain Nd:YAG laser at 946 nm.

2.2.1 Design of Semiconductor Saturable Absorbers

The present saturable absorber was fabricated to combine a SESAM with an output coupler (SESAMOC) that was originally proposed by Spühler et al. to simplify the cavity configuration in passively Q-switched lasers [18]. The SESAMOC device, as shown in **Fig. 2.2.1**, was monolithically grown on an undoped 350 μm thick GaAs substrate by metalorganic chemical vapor deposition (MOCVD) to comprise three strained InGaAs/GaAs QWs grown on the Bragg mirror. The QWs have a thickness

of 8 nm and are separated by 10 nm thick GaAs layers. The Bragg mirror consists of eleven AlAs/GaAs quarter-wavelength layers, designed for a reflectivity in the region of 97~98% at 946 nm. The back side of the GaAs substrate was coated for antireflection at 946 nm ($R < 1\%$). **Figure 2.2.2** shows the measured result for the low-intensity transmission spectrum of the SESAMOC. It can be seen that the low-intensity transmission was approximately 1.5% at 946 nm and 56% at 1064 nm. The experimental result of the room-temperature photoluminescence (PL) spectrum is depicted in **Fig. 2.2.3**. The peak wavelength of the PL spectrum is found to be in the vicinity of 946 nm and the full-width at half maximum (FWHM) is approximately 20 nm. The saturation measurements were performed using nanosecond Q-switched laser pulses to coincide with the present Q-switched experiment. Experimental results revealed that the present SESAM device had a modulation depth of 1.5% and a saturation fluence of $20 \mu\text{J}/\text{cm}^2$.



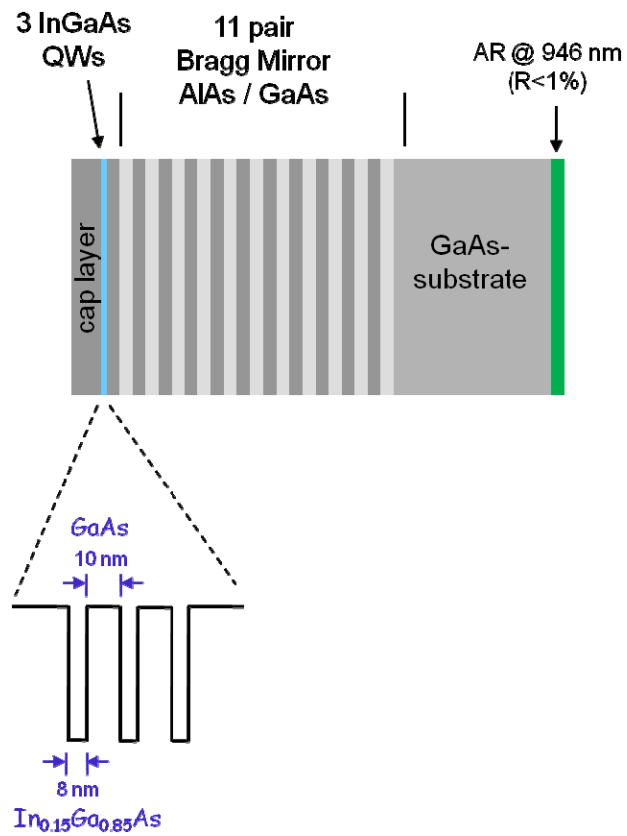


Fig. 2.2.1. The structure of the InGaAs SESAMOC.

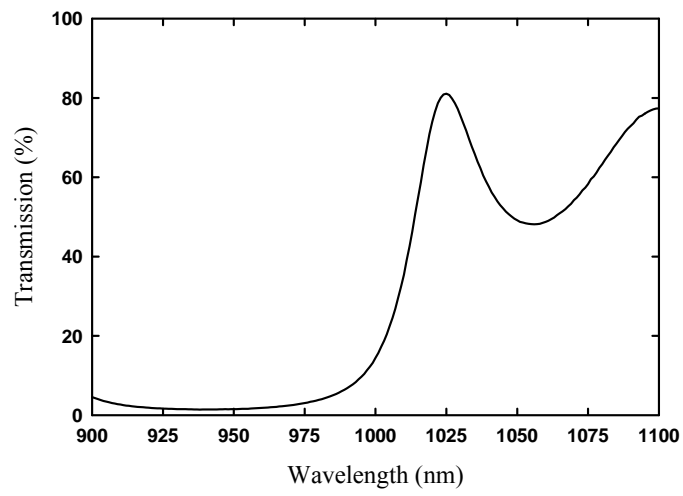


Fig. 2.2.2. Measured results for the low-intensity transmission spectrum.

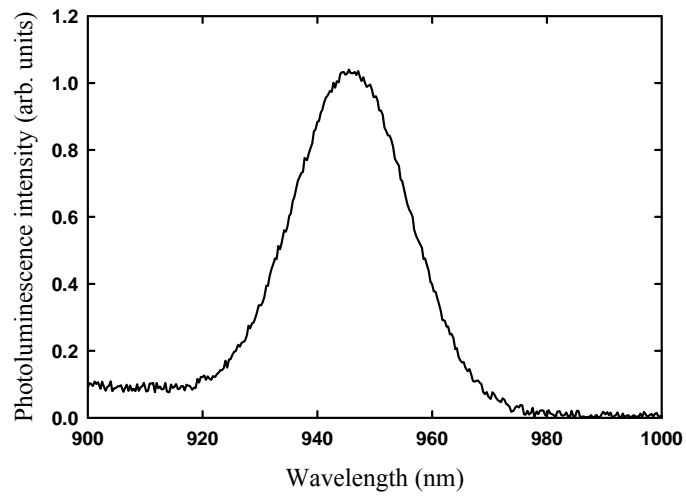


Fig. 2.2.3. Room-temperature photoluminescence (PL) spectrum of the InGaAs QWs saturable absorber.

2.2.2 Experimental Setup

Figure 2.2.4 shows the experimental configuration of the passively Q-switched 946 nm Nd:YAG laser with InGaAs QWs as a SESAMOC. The active medium was 1.1 at.% Nd:YAG crystal with a length of 2.0 mm. The entrance surface of the laser crystal was coated to be high reflection at 946 nm ($R > 99.8\%$) and high transmission at 808 nm ($T > 90\%$) and 1064 nm ($T > 85\%$). The other surface of the laser crystal was coated for antireflection at 946 nm ($R < 0.2\%$). The laser crystal was wrapped with indium foil and mounted in a water-cooled copper block. The pump source was a 10-W 808-nm fiber-coupled laser diode with a core diameter of 600 μm and a numerical aperture of 0.16. Focusing lens with 5 mm focal length and 92% coupling efficiency was used to re-image the pump beam into the laser crystal. The pump spot radius was approximately 160 μm . The cavity length was approximately 15 mm. The spectral information of the laser was monitored by an optical spectrum analyzer (Advantest Q8381A). The spectrum analyzer employing diffraction lattice monochromator can be used for high-speed measurement of pulse light with the resolution of 0.1 nm. The pulse temporal behavior was recorded by a LeCroy digital oscilloscope (Wavepro 7100, 10 G samples/sec, 1 GHz bandwidth) with a fast PIN photodiode.

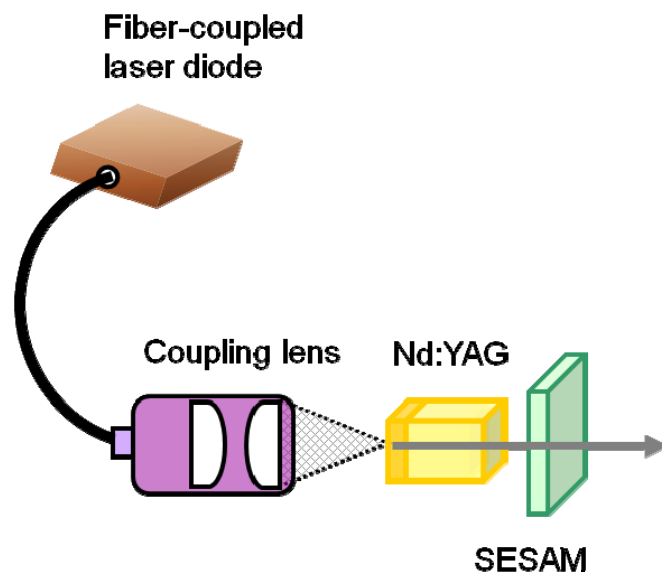


Fig. 2.2.4. Schematic of a diode-pumped passively Q-switched Nd:YAG laser at 946 nm.

2.2.3 Experimental Results and Discussion

The average output powers at 946 nm with respect to the incident pump power in the passively Q-switching operation are depicted in **Fig. 2.2.5**, and the optimum cw performance with the optimum reflectivity of the output coupler of 97% is shown for comparison. The output power in the CW operation reached 1.21 W at an incident pump power of 9.2 W. In the passively Q-switching regime an average output power of 1.1 W was obtained at an incident pump power of 9.2 W. Experimental results indicate that the Q-switching efficiency (ratio of the Q-switched output power to the cw one at the maximum pump power) exceed 90%. The extremely high Q-switching efficiency signifies the nonsaturable losses of the present SESAMOC to be considerably low.

Fig. 2.2.6 shows the pulse repetition rate and the pulse energy versus the incident pump power. It was found that the pulse repetition rate was linearly proportional to the pump power and approximately reached 55 kHz at an incident pump power of 9.2 W. Like typically passively Q-switched lasers, the pulse energy is almost unrelated to the pump power and its value is 20 μJ on average. On the whole, the pulse duration was approximately 38 ns. With the measured pulse energy and pulse width, the peak power can be found to be up to 0.53 kW. A typical oscilloscope trace of a train of output pulses and an expanded shape of a single pulse are shown in **Fig. 2.2.7**. Under the optimum alignment condition, the pulse-to-pulse amplitude fluctuation was less than $\pm 5\%$ for the pump power lower than 6 W and within $\pm 15\%$ at the maximum pump power of 9.2 W.

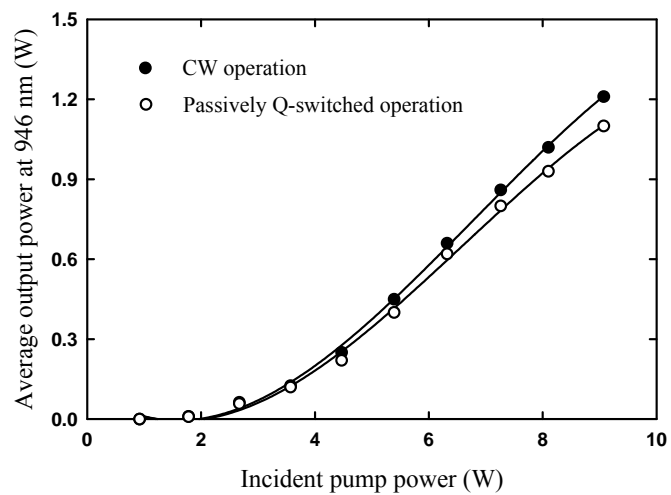


Fig. 2.2.5. The average output powers at 946 nm with respect to the incident pump power in CW and passively Q-switching operations.

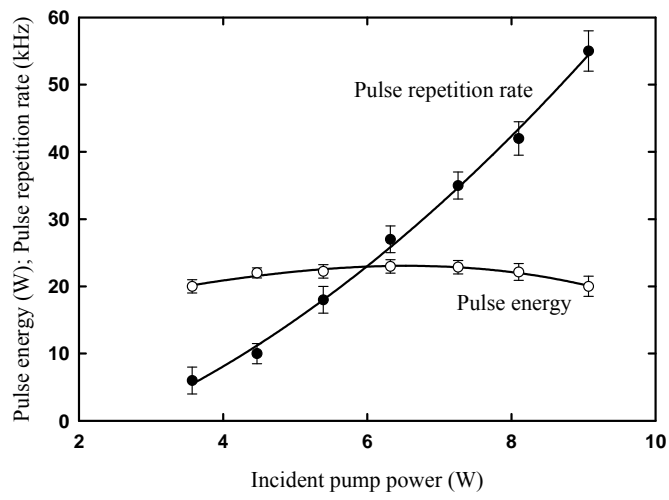


Fig. 2.2.6. Experimental results for pulse repetition rate and pulse energy versus incident pump power.

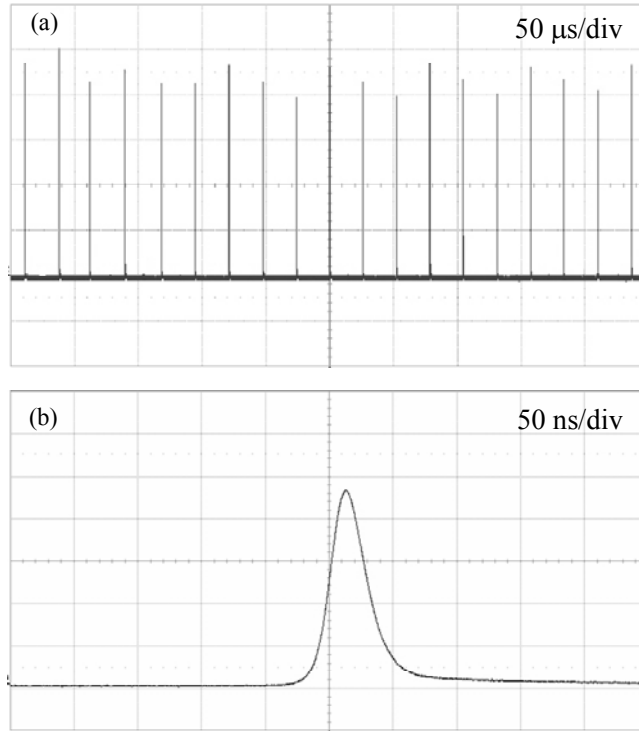


Fig. 2.2.7. (a) Typical oscilloscope trace of a train of output pulses and (b) expanded shape of a single pulse.

2.3 High-Power 946 nm Nd:YAG Laser and Blue Laser at 473 nm in QCW operation

With the rapid development of laser diode, high-power 2 D laser diode arrays (LDA) or diode stacks have been used in diode-pumped solid-state lasers to generate high output pulse energies in free-running or Q-switched operations for several years. Compared with the conventional high-power pump source, flash lamps, the 2D diode stacks, consisting of several diode bars, possess many advantages of higher repetition rates, higher overall efficiency, much lower thermal loading, and higher reliability.

High-power diode stacks are operated in the pulse durations of several hundred micro-seconds, i.e. quasi-cw (QCW) operations, and emit high peak powers (on-time average powers) of several hundred watts. The QCW pumping technique provides not only the high-level power but also the average heat-loading reduction. In this part, we used a 2D diode stack in QCW operation as the pump source. A high-power, QCW diode-pumped Nd:YAG laser operating at 946 nm and its intracavity frequency doubling to 473 nm with a BiBO crystal were demonstrated.

2.3.1 High-Power QCW pump source

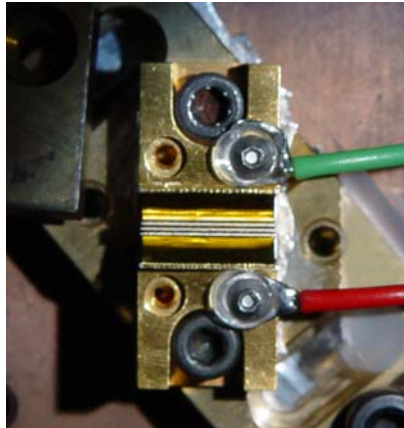
Here, the pump source is a high-power QCW diode stack (Quantel laser diodes) that consists of three 10-mm-long diode bars generating 130 W per bar, for a total of 390 W at the central wavelength of 808 nm. The diode stack is designed with 0.4 mm spacing between the diode bars so the overall area of emission is approximately 10 mm (slow axis) \times 0.8 mm (fast axis). The images of the diode stack are shown in **Fig. 2.3.1**. The full divergence angles in the fast and slow axes are approximately 35° and 10°, respectively. This divergence causes a great loss of pump power. Therefore, the highly efficient and simple optical devices, coupling the output from a laser diode stack into a gain medium, are especially important for the design of high power lasers with large laser diode stack as the pump source.

A lens duct was reported to have good coupling efficiency and was used to

end-pump solid-state lasers [19, 20]. The lens duct is a glass device that can consist of one spherical input surface and five planar surfaces, as shown in **Fig. 2.3.2 (a)**. The spherical surface is designed for efficient collection of the output radiation from a laser diode stack into the duct. Schematic of ray tracing inside a lens duct is depicted in **Fig. 2.3.3**. The light rays are totally reflected from the four side surfaces until they reach the planar output surface, and then injected into the gain medium. The output surface of lens duct has to adjoin the gain medium to reduce the coupling loss. **Fig. 2.3.2 (b)** shows the lens duct assembly. For practical reasons the lens duct has to be made of two pieces glued together. The first piece is a slice of a commercial plano-cylindrical lens, which provides the curved face. The second piece is a lens duct all of whose faces are plane. The curved surface of the plano-cylindrical lens and the lens duct output face are not antireflection coated.

In comparison with other coupling methods such as optical fibers [21], gradient-index (GRIN) lenses [22], or aspheric lenses [23], the lens duct has the benefits of simple structure, high coupling efficiency, and impervious to slight misalignment. These benefits are practically important for the end-pumped solid-state lasers with laser-diode stacks in which there is a significant geometric mismatch between the effective diode emitter area and the available input aperture of the gain medium.

(a)

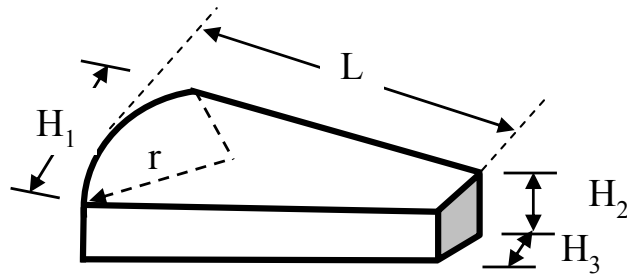


(b)



Fig. 2.3.1. (a) Image of the Quantel laser diode and (b) the near-field image of laser diode emitters at 30 A.

(a)



(b)

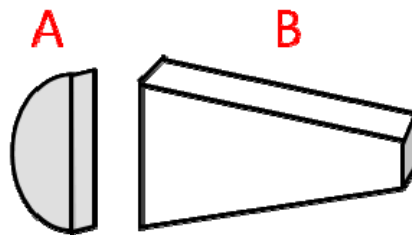
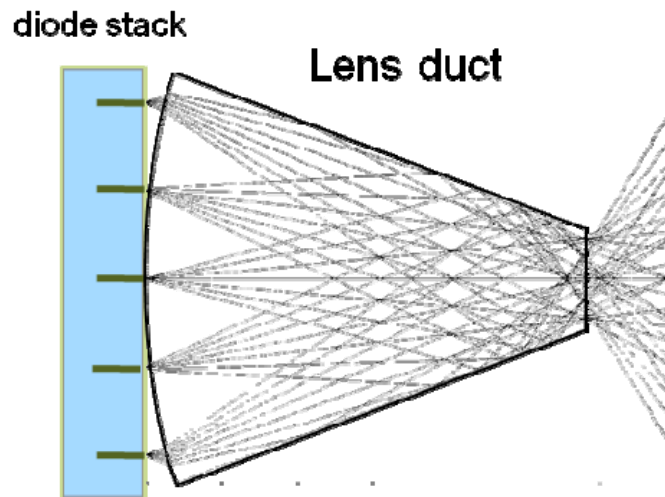


Fig. 2.3.2. (a) Schematic of a lens duct with five geometric parameters of r , L , H_1 , H_2 , and H_3 : r is the radius of the input surface, L is the length of the duct, H_1 is the width of the input surface, H_2 is the width of the output surface, and H_3 is the thickness of the duct. (b) Lens duct assembly.

(a)



(b)

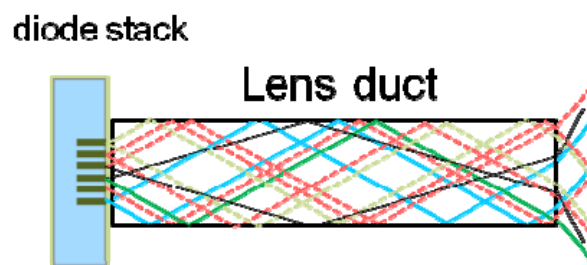


Fig. 2.3.3. Schematic of ray tracing inside a lens duct: (a) top view in the slow-axis plane [20], (b) side view in the fast-axis plane.

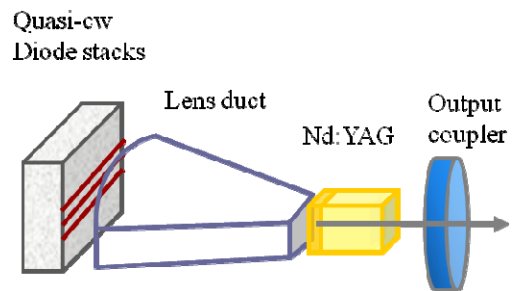
2.3.2 Experimental Setup

In this experiment, the lens ducts were manufactured with the same parameters of $r = 10$ mm, $L = 30$ mm and $H_1 = 12$ mm, but the various output cross-sections with $H_2 \times H_3$ at mm^2 of 2.1×2.1 , 1.6×1.6 and 1.2×1.2 , respectively. The coupling efficiencies of three lens ducts were experimentally found to be approximately 86, 78, and 72%, respectively. The active medium was $3 \times 3 \times 5$ mm^3 Nd:YAG crystal with 1.1 at.%. Approximately 75% of the pump light was absorbed in the active medium. The entrance surface of the laser crystal was coated with high reflection at 946 nm ($R > 99.8\%$) and high transmission at 808 nm ($T > 90\%$) and 1064 nm ($T > 85\%$). The other surface of the laser crystal was coated for antireflection at 946 nm ($R < 0.2\%$).

Fig. 2.3.4 (a) shows the schematic diagram of QCW 946 nm Nd:YAG laser. The output couplers were flat and coated for high transmission at 1064 nm ($T > 90\%$) and partial reflection at 946 nm ($R = 97\%$). The cavity length was approximately 10 mm. **Fig. 2.3.4 (b)** shows the experimental configuration of cw intracavity frequency-doubled Nd:YAG laser. The frequency doubler was a 5-mm-long BiBO crystal, cutting for type-I critical phase-matching ($\theta = 161.7^\circ$, $\phi = 90^\circ$) at room temperature. Both facets of the BiBO crystal were coated for anti-reflection at 946 and 473 nm ($R < 0.2\%$) to reduce the reflection loss in the cavity. The laser crystals were wrapped with indium foil and mounted in a water-cooled copper block. A plano-concave mirror of 50 mm radius was chosen to be the output coupler coated for high reflection at 946 nm ($R > 99.8\%$), high transmission at 1064 nm ($T > 70\%$), and high transmission at 473 nm ($T > 80\%$), respectively. The SHG cavity length of was approximately 30 mm.

The pulse temporal behavior was recorded by a LeCroy digital oscilloscope (Wavepro 7100; 10 G samples/sec; 1 GHz bandwidth) with a fast InGaAs photodiode. The spectral information of the laser was monitored by an optical spectrum analyzer (Advantest Q8381A). The spectrum analyzer employing diffraction grating monochromator can be used for high-speed measurement of pulse light with the resolution of 0.1 nm.

(a)



(b)

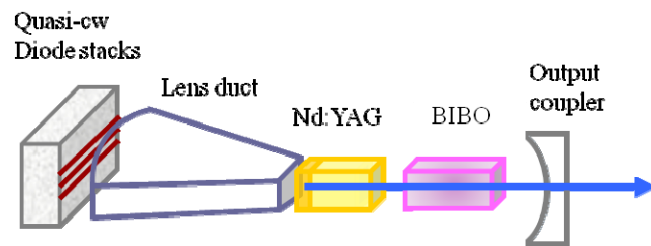


Fig. 2.3.4. Schematics of QCW diode-pumped Nd:YAG lasers at 946 nm in (a), and intracavity frequency-doubling at 473 nm in (b).

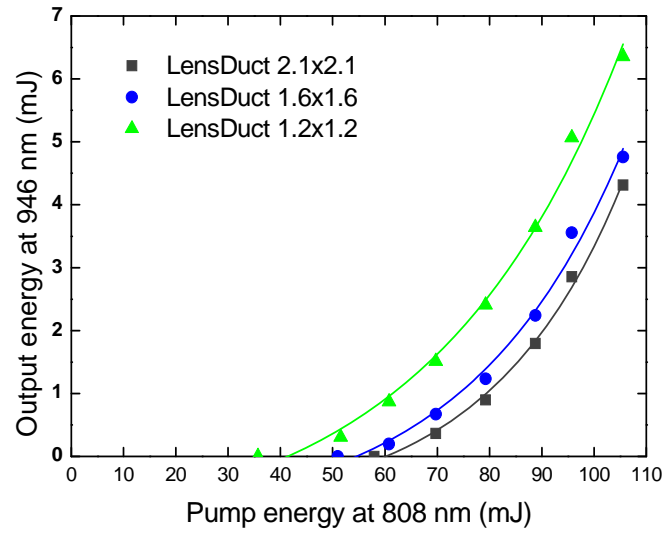
2.3.3 Experimental Results and Discussion

First of all, the QCW free running operation of the Nd:YAG laser at 946 nm was measured without the BiBO crystal in the cavity to confirm the pump efficiency of the lens duct and the quality of the laser crystal. In this experiment, the laser-diode stack was set to emit pump pulses of 270 μs at a repetition rate of 35 Hz, as the duty cycle was approximately 1 %. Three kinds of output cross-sections of lens ducts were employed for comparisons in the quasi-continuous-wave free running operation. **Fig. 2.3.5 (a)** shows the experimental results of the output pulse energy at 946 nm with respect to the pump energy emitted from the laser diode in the free-running operation. It can be found that the lower pump threshold and higher output energy were achieved by employing a lens duct with a smaller output dimension. With the lens duct with the smallest output surface of $1.2 \times 1.2 \text{ mm}^2$, the lower pump threshold of 36 mJ and the maximum output pulse energy of 6.4 mJ were obtained at a pump energy of 105 mJ. The experimental results confirm that a high-intensity pump light is necessary for such quasi-three-level laser. Note that the smallest dimension of a lens duct is limited by the emission area of laser diode stack. **Fig. 2.3.5 (b)** depicts the pulse train at repetition rate of 35 Hz, at the maximum pump energy. **Fig. 2.3.6 (a)-(c)** depict the temporal shapes of the single pulse exhibited relaxation-oscillation driven spikes for the employed lens ducts with output dimensions of 2.1×2.1 , 1.6×1.6 , and $1.2 \times 1.2 \text{ mm}^2$, respectively. It can be seen that the relaxation-oscillation driven spikes and the pulse shape of laser of a single pulse were dominated by the pump intensity. Moreover, due to the laser buildup time, the output laser pulse was shorter than the pump duration of 270 μs in the QCW operation. The on-time average output power can be estimated with the laser output pulse width and pulse energy. The on-time average output power at 946 nm versus the on-time average pump power is plotted in **Fig. 2.3.7**. Using a lens duct with the output dimension of $1.2 \times 1.2 \text{ mm}^2$, the maximum on-time average output power was 34 W at the on-time average pump power of 392 W. The overall slope efficiency of the three curves were nearly similar to be 13 %.

The QCW diode-end-pumped Nd:YAG laser at 473 nm by intracavity frequency

doubling was operated by inserting a nonlinear crystal BiBO and replacing of the above mentioned concave mirror. The experimental results of the output pulse energy at 473 nm versus the pump energy are plotted in **Fig. 2.3.8**. It reveals that the pump intensity is extremely critical for an efficient SHG of the 946-nm low-gain laser. Using a lens duct with the output dimension of $1.2 \times 1.2 \text{ mm}^2$, the maximum output pulse energy of approximately 1.75 mJ was achieved for 105 mJ pump energy from the laser diode stack. **Fig. 2.3.9** shows the estimated on-time average output power at 473 nm as a function of the on-time average pump power. The maximum on-time average output power at 473 nm of approximately 9 W was estimated at 392 W of the on-time average pump power. The conversion efficiency of blue light at 473 nm with respect to the average output power of the free running performance was greater than 26 %. To our best knowledge, it is the highest average power for intracavity frequency-doubling in the blue region at 473 nm of diode-end-pumped Nd:YAG laser. **Fig. 2.3.10 (a)-(b)** depict the pulse train and temporal shape of the single pulse at the maximum pump energy of 105 mJ by using a lens duct with the output dimension of $1.2 \times 1.2 \text{ mm}^2$. Under the optimal alignment condition, the pulse-to-pulse amplitude fluctuation was estimated to be approximately $\pm 10 \%$. The spatial distribution of the output blue-light beam was recorded with a CCD as displayed in **Fig. 2.3.10(c)**. The beam quality factors were measured and found to be $M_x^2 < 12$ and $M_y^2 < 7$, repetitively, where the x and y directions are parallel to the slow and fast axes of the laser-diode stack. The asymmetry of the M^2 factors in the x and y directions was due to the walk-off effect by nonlinear crystal.

(a)



(b)

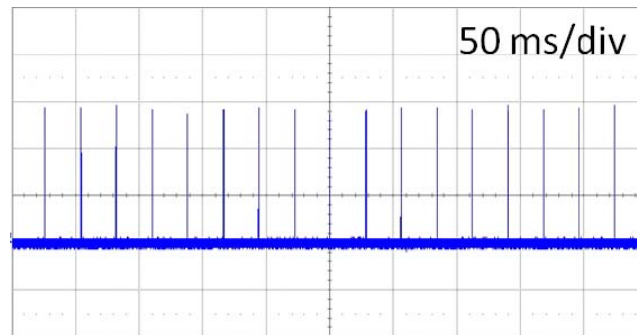


Fig. 2.3.5. Experimental results of (a) the free-running operation for the output pulse energy at 946 nm versus the pump energy for three kinds of output surfaces of lens ducts, and (b) pulse train at the maximum pump energy.

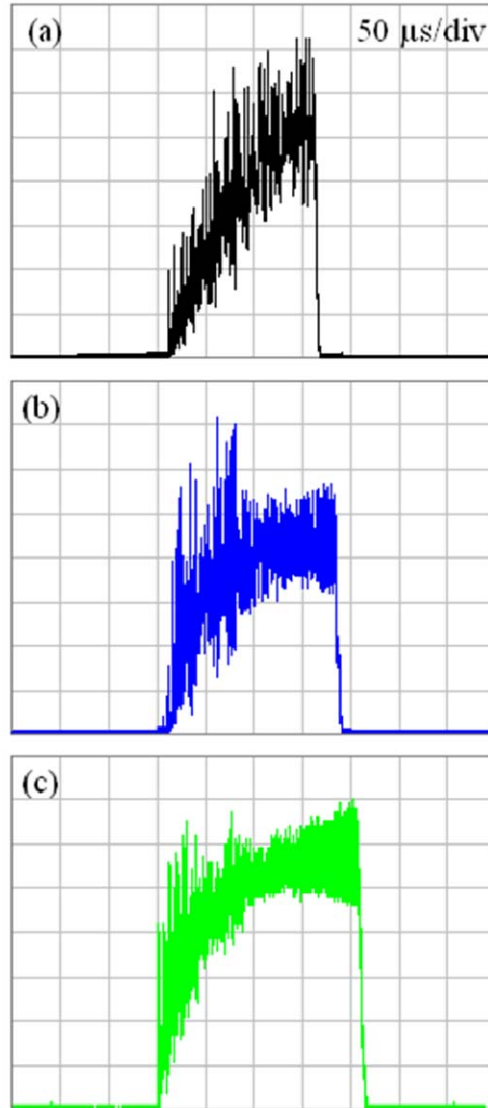


Fig. 2.3.6. Temporal shapes of the single pulse for the lens duct output surface of (a) $2.1 \times 2.1 \text{ mm}^2$; (b) $1.6 \times 1.6 \text{ mm}^2$; (c) $1.2 \times 1.2 \text{ mm}^2$.

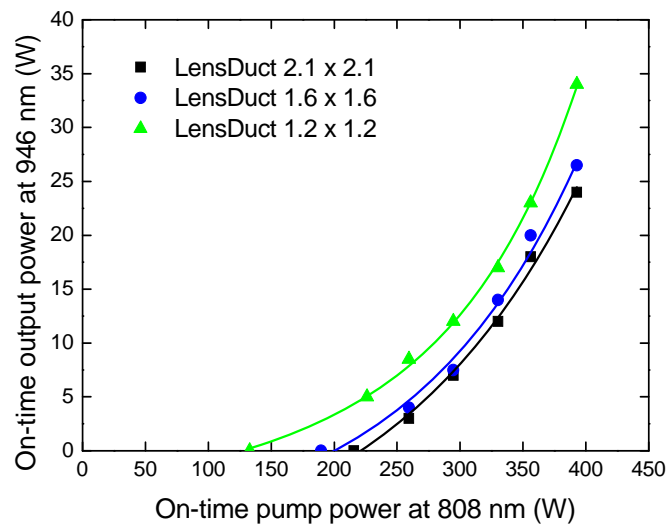


Fig. 2.3.7. Estimated on-time average output power at 946 nm versus the on-time average pump power in the free-running performance, for three kinds of output surfaces of lens ducts.

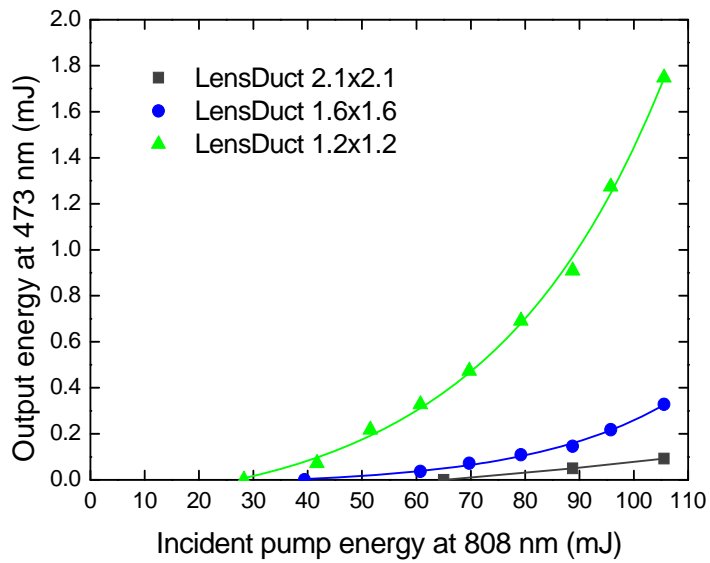


Fig. 2.3.8. Experimental results of the free-running operation for the output pulse energy at 473 nm versus the pump energy for three kinds of output surfaces of lens ducts.

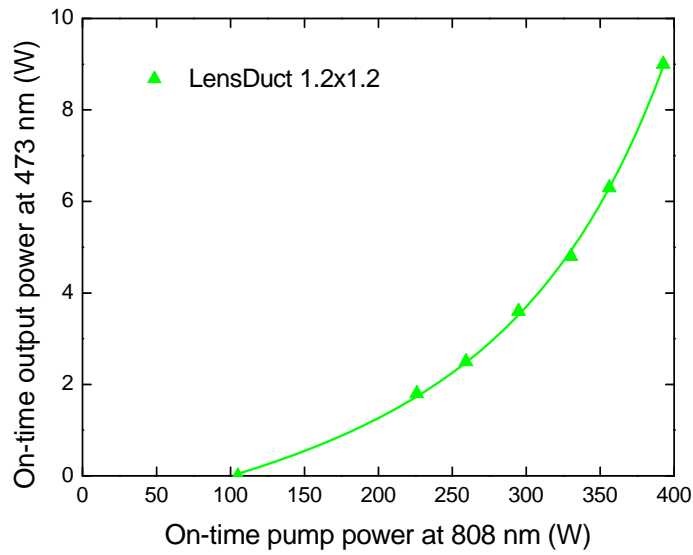
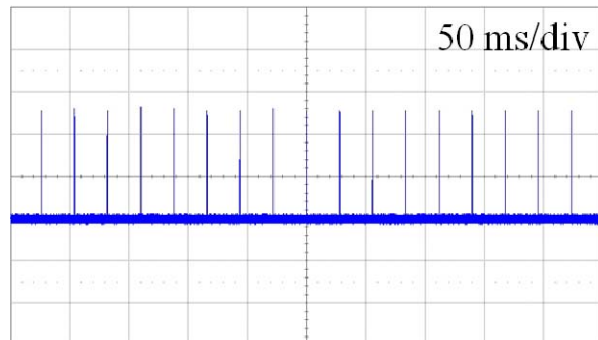
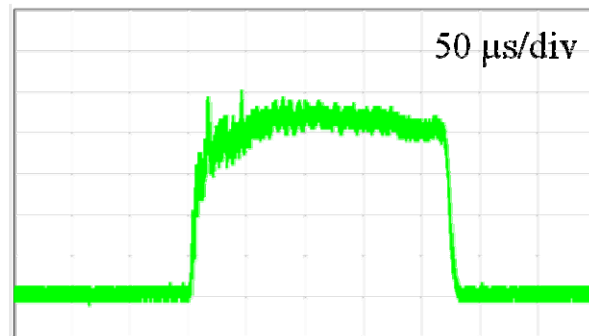


Fig. 2.3.9. Estimated on-time average output power at 473 nm as a function of the on-time average pump power for the lens duct with an output surface of $1.2 \times 1.2 \text{ mm}^2$.

(a)



(b)



(c)

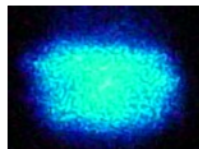


Fig. 2.3.10. Experimental results for the lens duct with an output surface of $1.2 \times 1.2 \text{ mm}^2$: (a) pulse train at the maximum pump energy of 105 mJ; (b) temporal shape of the single pulse at the maximum pump energy of 105 mJ; (c) Spatial distribution of the output blue beam recorded with a CCD.

2.4 High-Peak-Power Passively Q-Switched Nd:YAG Laser at 946 nm

High-peak-power pulsed lasers are highly desirable for some applications such as remote sensing, ranging, and micromachining. Recently, Kellner *et al.* and Kimmelma *et al.* utilized a Cr⁴⁺:YAG crystal as a saturable absorber in a passively Q-switched Nd:YAG 946-nm laser [24,25]. The generated pulse energies were less than 100 μ J with the less than 4 kW peak powers. Besides, semiconductor materials based on the GaAs substrate have been developed to be saturable absorbers in Nd:YAG lasers at 946 nm [26,27]. Up to now, the maximum pulse energy and highest peak power of passively Q-switched Nd:YAG 946-nm lasers with semiconductor saturable absorbers (SESAs) are 20 μ J and 0.53 kW, respectively [27].

In this section, we designed the InGaAs/GaAs QWs similar to that mentioned in **Section 2-2**. In order to generate a high-peak-power and high-pulse-energy Q-switched Nd:YAG laser at 946 nm, the QCW diode stack was used as the pump source. We make a thorough comparison for the output performance between the saturable absorbers of the InGaAs quantum wells (QWs) and the Cr⁴⁺:YAG crystal.

2.4.1 Experimental Setup

Figures 2.4.1 (a)-(b) are the experimental setups for high-power QCW diode-pumped passively Q-switched Nd:YAG lasers at 946 nm with a Cr⁴⁺:YAG crystal and an InGaAs QW structure as a saturable absorber, respectively. The pump source consists of three 10-mm-long diode bars generating 130 W per bar as described in **Section 2.3.1**. In this experiment, the coupling component was a lens duct with the parameters of $r = 10$ mm, $L = 32$ mm, $H_1 = 12$ mm, $H_2 = 1.6$ mm, and $H_3 = 1.6$ mm. The coupling efficiency of this lens duct is experimentally found to be approximately 78%. The active medium was 1.1 at.% Nd:YAG crystal with a length of 5.0 mm and with a transverse aperture of 3×3 mm². The entrance surface of the laser crystal was coated to be high reflection at 946 nm ($R > 99.8\%$) and high transmission at 808 nm

($T > 90\%$) and 1064 nm ($T > 85\%$). The other surface of the laser crystal was coated for antireflection at 946 nm ($R < 0.2\%$). The laser crystal was wrapped with indium foil and mounted in a copper block.

A Cr^{4+} :YAG crystal is used as a saturable absorber for the passive Q-switching operation. The Cr^{4+} :YAG crystal had a thickness of 1 mm with 95% initial transmission at 946 nm. Both sides of the Cr^{4+} :YAG crystal were coated for antireflection at 946 nm. A plane mirror is chosen to be the output coupler whose reflection at 946 and 1064 nm were 95% and $< 20\%$, respectively. The other passive Q-switching operation is to employ a semiconductor saturable-absorber mirror (SESAM) [18,28,29]. The SESAMOC device was monolithically grown on an undoped 350 μm thick GaAs substrate by metalorganic chemical vapor deposition (MOCVD) to comprise three strained $\text{In}_{0.15}\text{Ga}_{0.85}\text{As}/\text{GaAs}$ QWs grown on the Bragg mirror. The QWs have a thickness of 8 nm and are separated by 10 nm thick GaAs layers. The Bragg mirror consists of eight AlAs/GaAs quarter-wavelength layers, designed for a reflectivity in the region of 90~91% at 946 nm. The back side of the GaAs substrate was coated for antireflection at 946 nm ($R < 1\%$). **Fig. 2.4.2** shows the measured result for the low-intensity transmission spectrum of the SESAMOC. The SESAMOC with high transmission at 1064 nm is particularly critical to suppress the ${}^4F_{3/2} \rightarrow {}^4I_{11/2}$ transition and to lead to the lasing 946 nm. The saturation measurements were performed using nanosecond Q-switched laser pulses to coincide with the present Q-switched experiment. Experimental results revealed that the present SESAM device had a modulation depth of 1.5% and a saturation fluence of 20 $\mu\text{J}/\text{cm}^2$.

The pulse temporal behavior was recorded by a LeCroy digital oscilloscope (Wavepro 7100; 10 G samples/sec; 1 GHz bandwidth) with a fast InGaAs photodiode. The spectral information of the laser was monitored by an optical spectrum analyzer (Advantest Q8381A). The spectrum analyzer employing diffraction grating monochromator can be used for high-speed measurement of pulse light with the resolution of 0.1 nm.

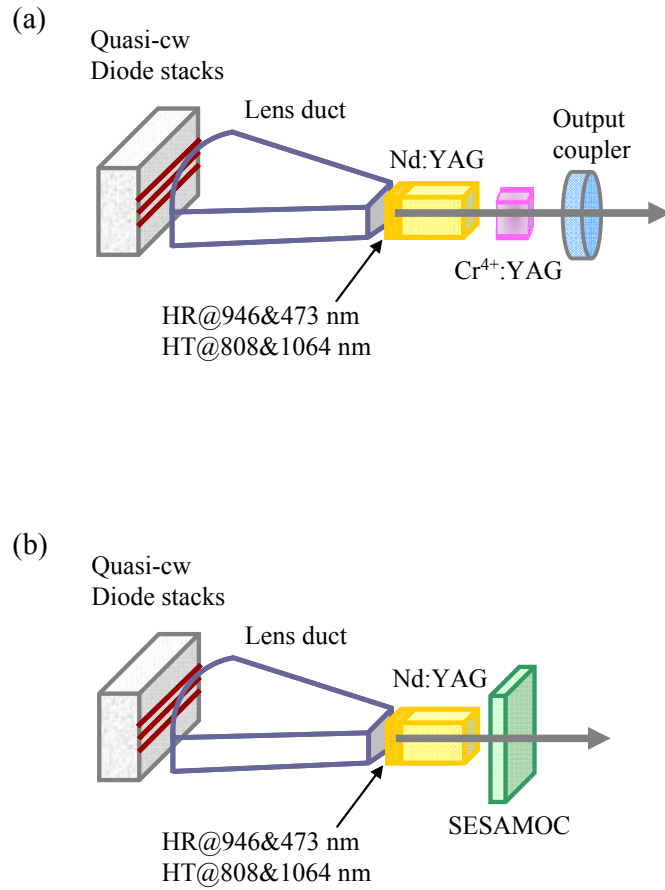


Fig. 2.4.1. Schematic of a diode-pumped passively Q-switched Nd:YAG laser at 946 nm: (a) with the Cr⁴⁺:YAG crystal as a saturable absorber; (b) with the InGaAs QWs as a saturable absorber and an output coupler.

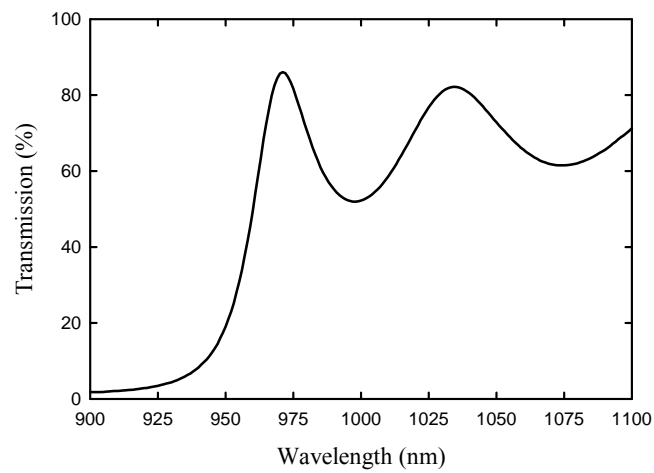


Fig. 2.4.2. The low-intensity transmission spectrum for the InGaAs SESAMOC: transmission at 946 nm and 1064 nm are approximately 10% and 64%, respectively.

2.4.2 Experimental Results and Discussion

The first passively Q-switched Nd:YAG laser at 946 nm was performed by inserting a Cr⁴⁺:YAG crystal into the same plano-plano cavity. The threshold of the Q-switched laser operation was found to be approximately 75 mJ and the output pulse energy at 946 nm was measured to be 95 μ J. The effective pulse width was found to be 28 ns; consequently, the peak power was approximately 3.4 kW. As shown in **Fig.2.3.5 (a)**, the output pulse energy in the free-running regime is 2.1 mJ at 75 mJ of pump energy (Note that the pump energy has been considered the coupling efficiency). Consequently, the extraction efficiency with respect to the output energy from the free-running operation is approximately 4.5%. When the pump energy is higher than 80 mJ, the laser cavity generates double pulses with the pulse characteristics nearly the same as the single pulse output, as shown in **Fig. 2.4.3**.

The second passive Q-switching operation was performed by employing the above-mentioned SESAMOC to replace the Cr⁴⁺:YAG and the output coupler. The threshold of the Q-switched laser operation was found to be approximately 73 mJ and the output pulse energy at 946 nm was measured to be 330 μ J. As shown in **Fig. 2.4.4 (a)**, the effective pulse width was found to be approximately 30 ns; consequently, the peak power was greater than 11 kW. As shown in **Fig.2.3.5 (a)**, the output pulse energy in the free-running regime is 2.1 mJ at 75 mJ of pump energy. Therefore, the extraction efficiency with respect to the output pulse energy from the free-running operation can be found to be approximately 15.8%. Compared to the results obtained with the Cr⁴⁺:YAG saturable absorber, both lasing thresholds are almost equal; however, the output pulse energy and efficiency with the present SESAMOC are three times higher. The superior performance of the present SESAMOC comes from the considerably low nonsaturable losses. When the pump energy is higher than 80 mJ, the laser cavity can generate triple pulses with the pulse characteristics nearly as good as the single pulse output, as depicted in **Fig. 2.4.4 (b)**. Under the optimal alignment condition, the pulse-to-pulse amplitude fluctuation was found to be approximately $\pm 10\%$. The residual pump light radiating on the SESAMOC did not clearly reveal to cause any influence on the output performance. Finally, the spatial

distribution of the output beam was recorded with an infrared CCD and displayed in **Fig. 2.4.5**. The beam quality factor $M_x^2 \times M_y^2$ was measured and found to be 1.3×3.5 , where the x and y directions are parallel to the slow and fast axes of the diode stack. Although the present beam quality is about 4 times worse than the diffraction-limited result reported in the previous Q-switched 946-nm laser generating about $80 \mu\text{J}$ [12], the peak power enhancement leads to the present brightness to be approximately increased 2.7 times.



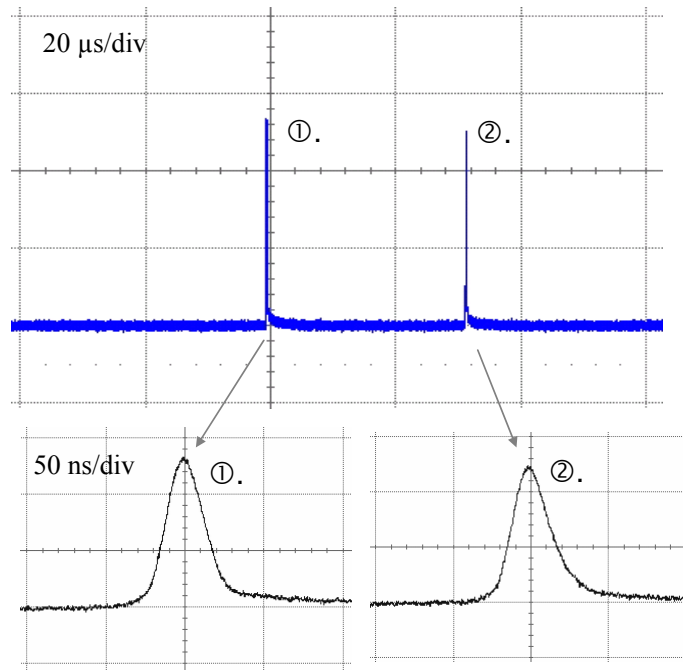


Fig. 2.4.3. Typical result of double pulses in the passively Q-switched Nd:YAG/Cr⁴⁺:YAG laser at 946 nm (upper); expanded shape of each pulse (lower).

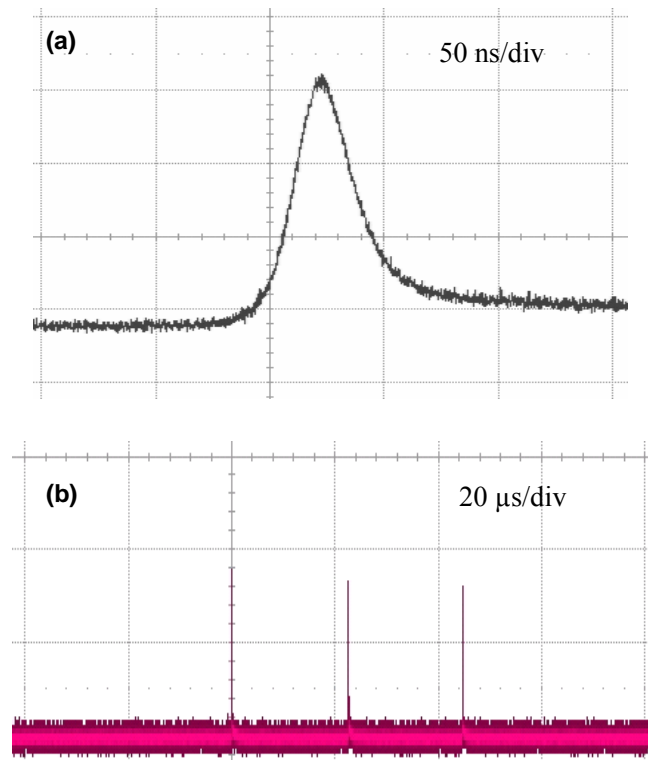


Fig. 2.4.4. (a) typical oscilloscope trace of a single pulse; (b) typical oscilloscope trace of triple pulses with the InGaAs QWs as a saturable absorber.

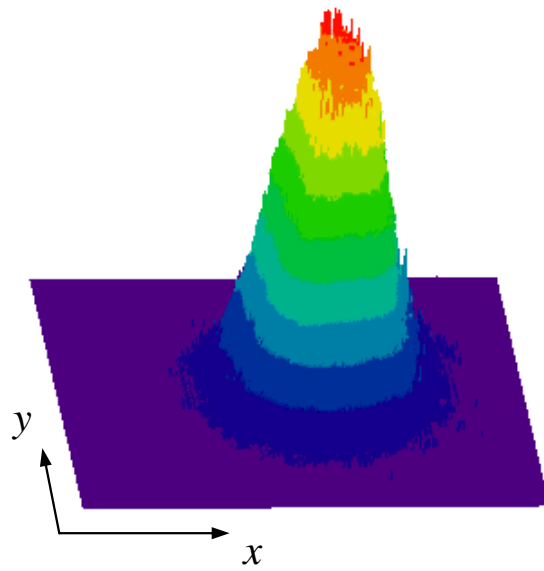


Fig. 2.4.5. 3D spatial distribution of the output beam recorded with an infrared CCD.

2.5 Conclusions

Diode-pumped Nd:YAG lasers at 946 nm, blue light generation at 473 nm by intracavity frequency doubling, and 946-nm passive Q-switching operation have been performed. Two types of pump sources, cw fiber-coupled laser diode and QCW high-power laser diode stack, were used.

A cw diode-pumped Nd:YAG laser at 946 nm and a intracavity frequency doubling to 473 nm with a BiBO crystal were achieved. At an incident power of 19.6 W, the maximum output power at 946 nm can be up to 3 W with an optical-to-optical conversion efficiency of 15%. At a pump power of 13 W, the second harmonic generation (SHG) of 946-nm laser with an output average power of 0.75 W was generated. For passive Q-switching, InGaAs quantum wells (QWs) and a Bragg mirror structure are grown on a GaAs substrate to simultaneously serve as a low-loss saturable absorber and an output coupler for highly efficient Q switching of a diode-pumped Nd:YAG laser operating at 946 nm. Under cw fiber-coupled laser diode pumping, an average output power of 1.1 W was obtained at an incident pump power of 9.2 W. The maximum peak power was found to be up to 0.53 kW and the overall Q-switching efficiency was generally greater than 90%.

In order to generate a high-power Nd:YAG laser, the quasi-continuous-wave (QCW) diode stack was used as the pump source. A lens duct was utilized to efficiently couple the pump radiation from the diode stack into the laser crystal. Three kinds of output cross-sections of lens ducts were used for comparisons. Experimental results reveal that the pump intensity is critical for a low-threshold and high-power quasi-three-level laser, particularly for frequency doubling. Using a lens duct with the output dimension of $1.2 \times 1.2 \text{ mm}^2$, the maximum on-time average output powers at 946 nm and 473 nm were 34 W and 9 W, respectively, at the on-time average pump power of 392 W. The conversion efficiency of blue light at 473 nm with respect to the average output power of the free running performance was greater than 26 %. To our best knowledge, it is the highest average power for intracavity frequency-doubling in the blue region at 473 nm of diode-end-pumped Nd:YAG laser.

In addition, a high-peak-power QCW diode-pumped passive Q-switched Nd:YAG laser at 946 nm. A comparison for the output performance between the saturable absorbers of the InGaAs quantum wells (QWs) and the Cr⁴⁺:YAG crystal was demonstrated. Experimental results reveal that the InGaAs QWs is superior to the Cr⁴⁺:YAG crystal because of the low nonsaturable losses and leads to a pulse energy of 330 μ J with a peak power greater than 11 kW. The experimental results indicate the possibility of using InGaAs QWs structure to generate the high-peak-power blue laser at 473 nm with intracavity second harmonic generation.



References

- [1] T. Y. Fan and R. L. Byer, "Modeling and CW operation of a quasi-three-level 946 nm Nd: YAG laser," *IEEE J. Quantum Electron.* **23**, 605-612 (1987).
- [2] S. Singh, R. G. Smith, and L. G. Van Uitert, "Stimulated-emission cross section and fluorescent quantum efficiency of Nd³⁺ in yttrium aluminum garnet at room temperature," *Phys. Rev. B* **10**, 2566-2572 (1974).
- [3] T. Kellner, F. Heine, and G. Huber, "Efficient laser performance of Nd:YAG at 946 nm and intracavity frequency doubling with LiJO₃, β-BaB₂O₄, and LiB₃O₅," *Appl. Phys. B* **65**, 789-792 (1997).
- [4] P. Zeller and P. Peuser, "Efficient, multiwatt, continuous-wave laser operation on the ⁴F_(3/2)-⁴I_(9/2) transitions of Nd:YVO₄ and Nd:YAG," *Opt. Lett.* **25**, 34-36 (2000).
- [5] C. Czeranowsky, E. Heumann, and G. Huber, "All-solid-state continuous-wave frequency-doubled Nd:YAG-BiBO laser with 2.8-W output power at 473 nm," *Opt. Lett.* **28**, 432-434 (2003).
- [6] N. Pavel, I. Shoji, and T. Taira, "Continuous-wave high-power Nd:YAG-KNbO₃ laser at 473 nm," *Opt. Laser Technol.* **36**, 581-585 (2004).
- [7] R. Zhou, Z. Q. Cai, W. Q. Wen, X. Ding, P. Wang, and J. Q. Yao, "High-power continuous-wave Nd:YAG laser at 946 nm and intracavity frequency-doubling with a compact three-element cavity," *Opt. Commun.* **255**, 304-308 (2005).
- [8] P. X. Li, D. H. Li, and Z. G. Zhang, "Efficient generation of blue light by intracavity frequency doubling of a cw Nd:YAG laser with LBO," *Opt. Laser Technol.* **39**, 1421-1425 (2007).

- [9] M. Ghotbi and M. Ebrahim-Zadeh, "Optical second harmonic generation properties of BiB_3O_6 ," *Opt. Express* **12**, 6002-6019 (2004).
- [10] T. Y. Fan and R. L. Byer, "Modeling and CW operation of a quasi-three-level lasers 946 nm Nd:YAG laser," *IEEE J. Quantum Electron.* **23**, 605-612 (1987).
- [11] T. Y. Fan, "Optimizing the efficiency and stored energy in quasi-three-level lasers," *IEEE J. Quantum Electron.* **28**, 2692-2697 (1992).
- [12] T. Kellner, F. Heine, G. Huber, and S. Kuck, "Passive Q-switching of a diode-pumped 946-nm Nd:YAG with 1.6-W average output power," *Appl. Opt.* **37**, 7076-7079 (1998).
- [13] L. Zhang, C. Y. Li, B. H. Feng, Z. Y. Wei, D. H. Li, P. M. Lu, and Z. G. Zhang, "Diode-pumped passive Q-switched 946-nm Nd:YAG laser with 2.1-W average output power," *Chin. Phys. Lett.* **22**, 1420-1422 (2005).
- [14] S. M. Wang, Q. L. Zhang, L. Zhang, C. Y. Zhang, D. X. Zhang, B. H. Feng, Z. G. Zhang, "Diode-pumped passively Q-switched 946 nm Nd:YAG laser with a GaAs saturable absorber," *Chin. Phys. Lett.* **23**, 619-621 (2006).
- [15] S. Spiekermann, H. Karlsson, and F. Laurell, "Efficient frequency conversion of a passively Q-switched Nd:YAG laser at 946 nm in periodically poled KTiOPO_4 ," *Appl. Opt.* **40**, 1979-1982 (2001).

- [16] X. Zhang, A. Brenier, J. Wang, and H. Zhang, "Absorption cross-sections of Cr^{4+} :YAG at 946 and 914 nm," *Opt. Materials* **26**, 293-296 (2004).
- [17] S. Johansson, S. Bjurshagen, C. Canalias, V. Pasiskevicius, and F. Laurell, "An all solid-state UV source based on a frequency quadrupled, passively Q-switched 946 nm laser," *Opt. Express* **15**, 449-458 (2007).
- [18] G. J. Spühler, S. Reffert, M. Haiml, M. Moser, and U. Keller, "Output-coupling semiconductor saturable absorber mirror," *Appl. Phys. Lett.* **78**, 2733-2735 (2001).
- [19] R. J. Beach, "Theory and optimization of lens ducts," *Appl. Opt.* **35**, 2005-2015 (1996).
- [20] R. Fu, G. Wang, Z. Wang, E. Ba, G. Mu, and X. Hu, "Design of efficient lens ducts," *Appl. Opt.* **37**, 4000-4003 (1998).
- [21] Th. Graf and J. E. Balmer, "High power Nd:YLF laser end pumped by a diode-laser bar," *Opt. Lett.* **18**, 1317-1319 (1993).
- [22] B. Zhou, T. J. Kane, G. J. Dixon, and R. L. Byer, "Efficient, frequency-stable laser-diode-pumped Nd:YAG laser," *Opt. Lett.* **10**, 62-64 (1985).
- [23] L. Turi and T. Juhasz, "High-power longitudinal end-diode-pumped Nd:YLF regenerative amplifier," *Opt. Lett.* **20**, 154-156 (1995).
- [24] L. Zhang, C. Y. Li, B. H. Feng, Z. Y. Wei, D. H. Li, P. M. Lu, and Z. G. Zhang, "Diode-pumped passive Q-switched 946-nm Nd:YAG laser with 2.1-W average output power," *Chin. Phys. Lett.* **22**, 1420-1422 (2005).
- [25] O. Kimmelma, M. Kaivola, I. Tittonen, and S. Buchter, "Short pulse, high peak power, diode pumped, passively Q-switched 946-nm Nd:YAG laser," *Opt. Commun.* **273**, 496-499 (2007).

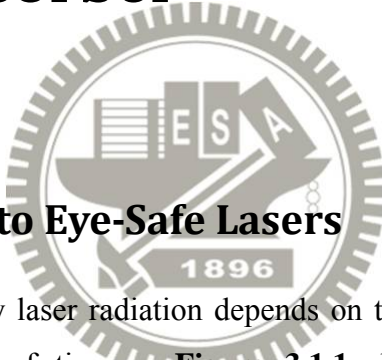
- [26] S. M. Wang, Q. L. Zhang, L. Zhang, C. Y. Zhang, D. X. Zhang, B. H. Feng, Z. G. Zhang, “Diode-pumped passively Q-switched 946 nm Nd:YAG laser with a GaAs saturable absorber,” *Chin. Phys. Lett.* **23**, 619-621 (2006).
- [27] Y. P. Huang, H. C. Liang, J. Y. Huang, K. W. Su, A. Li, Y. F. Chen, and K. F. Huang, “Semiconductor quantum-well saturable absorbers for efficient passive Q switching of a diode-pumped 946 nm Nd:YAG laser,” *Appl. Opt.* **46**, 6273-6276 (2007).
- [28] G. J. Spühler, R. Paschotta, R. Fluck, B. Braun, M. Moser, G. Zhang, E. Gini, and U. Keller, “Experimentally confirmed design guidelines for passively Q-switched microchip lasers using semiconductor saturable absorbers,” *J. Opt. Soc. Am. B* **16**, 376-388 (1999).
- [29] J. Y. Huang, H. C. Liang, K. W. Su, H. C. Lai, Y. F. Chen, and K. F. Huang, “InGaAs quantum-well saturable absorbers for a diode-pumped passively Q-switched Nd:YAG laser at 1123 nm,” *Appl. Opt.* **46**, 239-242 (2007).

Chapter 3

Diode-pumped Eye-Safe Nd:YAG Laser at 1.44 μm with an Intracavity

Selective Absorber

3.1 Introduction to Eye-Safe Lasers



Eye hazards caused by laser radiation depends on the wavelength, laser power, exposition time and type of tissue. **Figure 3.1.1** shows the eye transmission characteristic for the path to retina and the absorption curve of retina [1]. We can see that laser radiation in the range of 400 to 1400 nm is most dangerous for eye, because the retina, lens, aqueous humor and vitreous body transmit this range of radiation. **Figure 3.1.2** depicts the spectral transmission characteristics of the human eye [2]. Laser beam focused by eye lens on the retina, achieve high, dangerous power or energy densities. Radiation in the range of below 400 nm and above 1400 nm is strongly absorbed by the tissues such as cornea and the vitreous humor of eye, which are mainly composed of liquid water. The laser intensity is, therefore, attenuated significantly reaching the retina.

According to the American standard ANSI Z136.1-1986, the wavelength of 1.5 μm is treated as safe. Generally speaking, laser wavelength above 1400 nm which injury-threshold power becomes much higher is termed as “eye-safe laser”.

The methods for generating eye-safe lasers include the solid state lasers with Er^{3+} -doped or Cr^{4+} -doped media [3-6] and the stimulated Raman scattering (SRS) [7-10] or optical parametric oscillators (OPO) [11-13] pumped by Nd-doped lasers. The advent of diode-pumped solid-state lasers (DPSSLs) [14-17] with high peak powers and excellent brightness leads to a renaissance of interest in wavelength conversions with the SRS or OPO process. Alternatively, laser systems based on semiconductor quantum-well (QW) materials including InGaAsP and AlGaInAs are designed for eye-safe lasers [18-23].

Nd:YAG lasers have recently been proposed as candidates for a simpler solid-state system operating at the eye-safe wavelength of 1.444- μm laser transition [24-26]. Since 1.44- μm radiation which the absorption coefficient of water is comparable with that at 2.1- μm [25], it is a natural candidate for many applications not only in the field of surgery but also for many technical applications in LIDAR, communications [26-28], and medical applications [29-36] especially for facial skin rejuvenation. **Fig. 3.1.3** shows that water absorption at 20°C and penetration depth as a function of wavelength [37]. It can be noticed that Nd:YAG provides high water absorption ($a=26\text{cm}^{-1}$). The well-known attempts at line selection in Nd-doped lasers rely on appropriately coated cavity mirrors with a sufficiently large loss difference to suppress the competing transition channels [24].

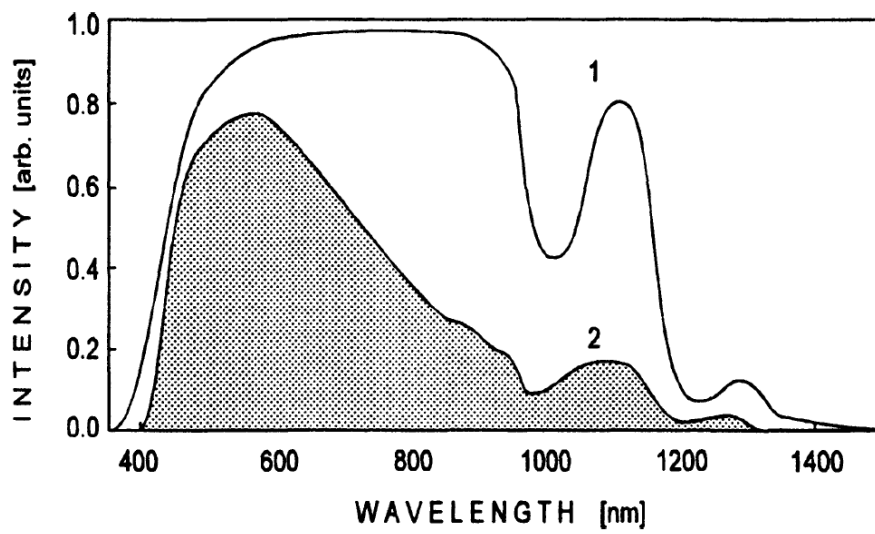


Fig.3.1.1. Penetration of radiation into the eye: 1 - eye transmission to the retina, 2 - radiation absorption in the retina [1].

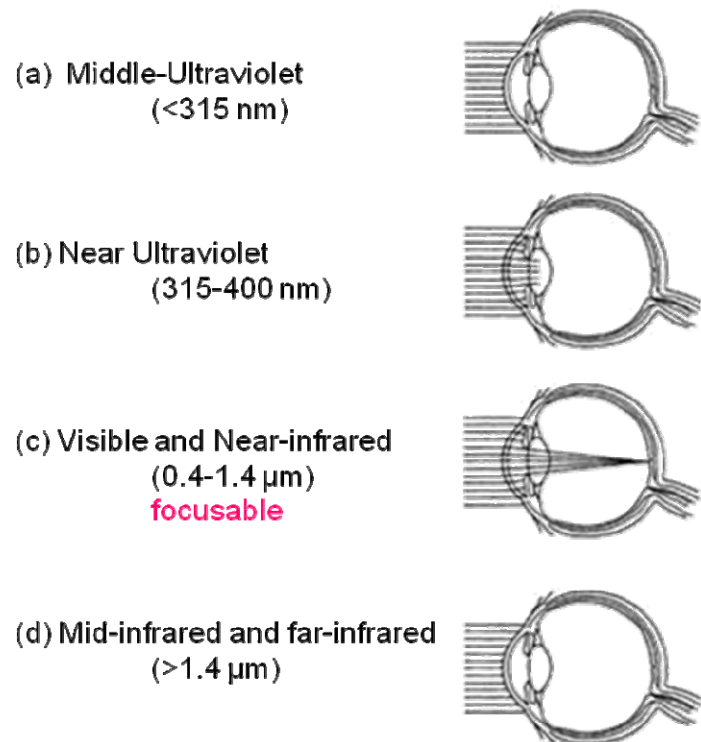


Fig. 3.1.2. Spectral transmission characteristics of the human eye [2].

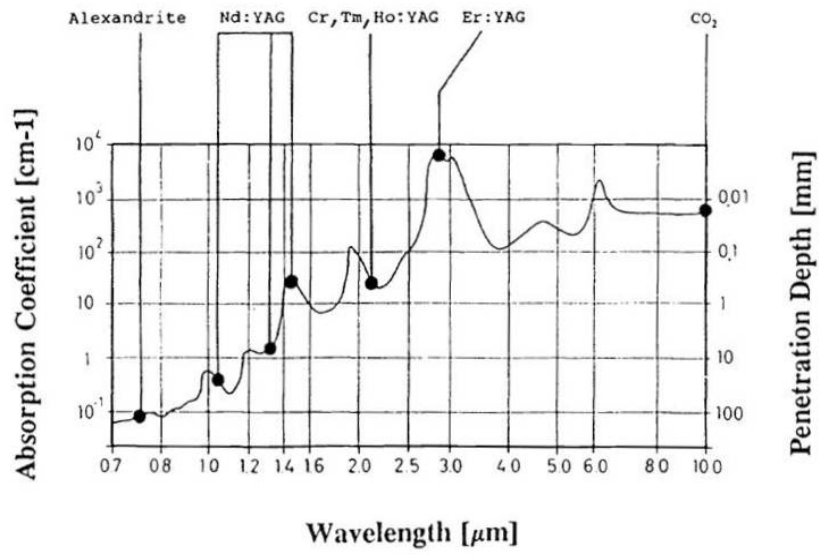


Fig.3.1.3. Water absorption at 20°C / penetration depth as a function of wavelength [37].

3.2 Design of Intracavity Selective Absorber

The fluorescence spectrum of Nd:YAG laser crystal, as shown in **Figure 3.2.1**, reveals that laser transitions in the ${}^4F_{3/2} \rightarrow {}^4I_{13/2}$ manifold. The stimulated cross section of the 1.44- μm transition line, however, is approximately 20 times smaller than 1.06- μm , which it is too weak to carry out. Therefore, the operation of a Nd:YAG laser at 1.44 μm requires a rather tough coating. Even though the coated cavity mirrors with a sufficient reflection contrast can lead to the 1.44 μm emission at low and middle pump powers, the power scaling tends to be hindered by the lasing of the 1.06 μm transition at high pump powers.

A method for overcoming this obstacle is to utilize the three-mirror folded resonator with an additional mirror to increase the loss difference between the lasing and competing channels. An alternative approach is the use of an intracavity selective absorber (ISA) in a simple linear cavity to absorb the competing emissions without introducing substantial losses at the lasing wavelength [38]. Therefore, the development of an ISA is practically beneficial to the power scaling of the weak transition in Nd-doped lasers.

We developed an AlGaInAs material as a promising ISA for an efficient high-power Nd:YAG laser at 1.44 μm . With the ISA to suppress operation at 1.06 μm , the output coupling at 1.44 μm can be flexibly optimized. The present ISA was composed of AlGaInAs quantum wells (QWs) with the barrier structure grown on a Fe-doped InP transparent substrate by metalorganic chemical-vapor deposition. Note that the conventional S-doped InP substrate cannot be used because of its significant absorption in the 1.0-2.0 μm spectral region, whereas the Fe-doped InP substrate is transparent in this spectral region. The absorption region of the ISA consists of 10 groups of two 10-nm QWs with the absorption wavelength around 1.32 μm , spaced at 190-nm intervals by AlGaInAs barrier layers with the absorption wavelength around 1.06 μm , as shown in **Fig. 3.2.2**. An InP window layer was deposited on the gain structure to avoid surface recombination and oxidation. The backside of the substrate was mechanically polished after growth. The both sides of the gain chip

were antireflection (AR) coated to reduce back reflections. The total residual reflectivity of the AR-coated sample is less than 5%. **Fig. 3.2.3** shows the transmittance spectrum for the AR-coated ISA device. It can be seen that the strong absorption of the barrier layers leads to an extremely low transmittance near 1.06 μm . The total absorption efficiency of the barrier layers at 1.06 μm was found to be higher than 96%. On the other hand, the absorption efficiency of the AlGaInAs QWs near 1.32 μm was approximately 35%. To the best of our knowledge, although the AlGaInAs material with a similar structure has been employed as a gain medium or a saturable absorber [39-43], it is designed as an ISA in solid-state lasers for the first time.



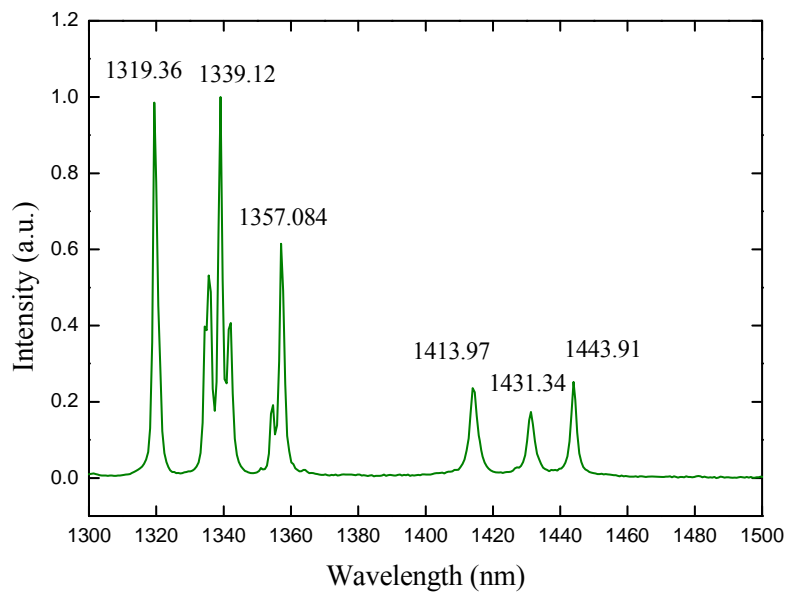


Fig. 3.2.1. The partial fluorescence spectrum of Nd:YAG laser crystal in the ${}^4F_{3/2} \rightarrow {}^4I_{13/2}$ manifold.

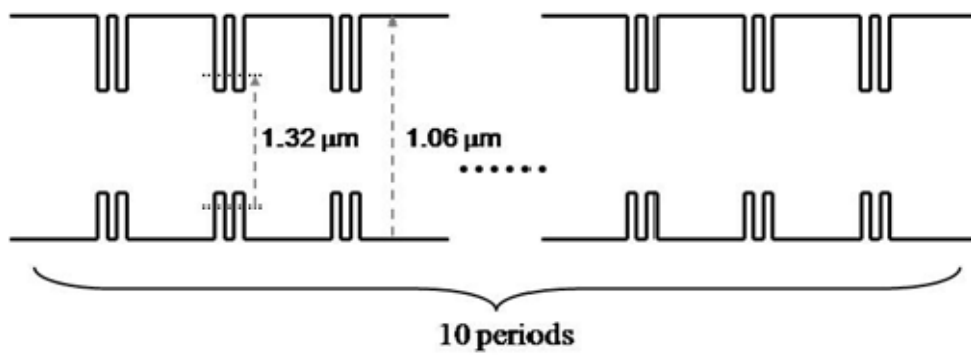


Fig. 3.2.2. Structure of the present ISA: the absorption region including 10 groups of two 10-nm QWs with the absorption wavelength around 1.32 μm , spaced at 190-nm intervals by AlGaInAs barrier layers with the absorption wavelength around 1.06 μm .

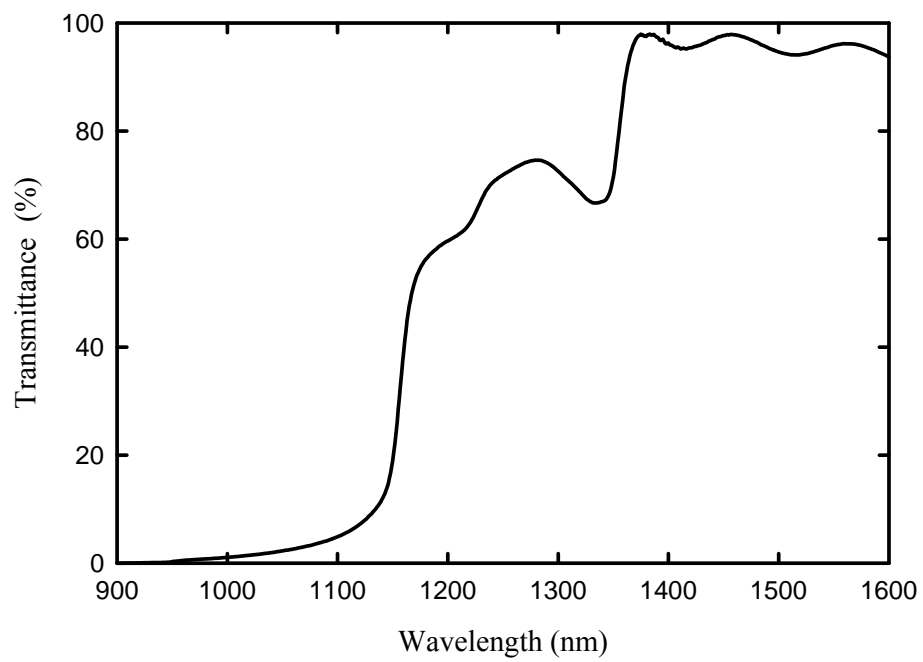


Fig. 3.2.3. Transmittance spectrum for the developed ISA device.

3.3 High-Power Continuous-Wave Nd:YAG Laser at 1.44 μm

3.3.1 Experimental Setup

A schematic of the laser experiment is shown in **Fig. 3.3.1**. The active medium was 1.0 at. % Nd:YAG crystal with a length of 10 mm. The entrance surface of the laser crystal was coated for high reflection at 1.06 μm ($R > 99.5\%$), 1.32 μm ($R > 99.5\%$), and 1.44 μm ($R > 99.5\%$) and for high transmission at 0.81 μm ($T > 85\%$). Note that the high reflection at 1.06 and 1.32 μm on the entrance surface was for the purpose of exploring the suppression ability of the developed ISA. The other surface of the laser crystal was coated for AR in the spectral range of 1.06–1.44 μm ($R < 0.2\%$). The laser crystal was wrapped with indium foil and mounted in a water-cooled copper block. The pump source was a 20 W 808 nm fiber-coupled laser diode with a core diameter of 600 μm and a numerical aperture of 0.16. A focusing lens with a 5 mm focal length and 85% coupling efficiency was used to reimage the pump beam into the laser crystal. The pump spot radius was approximately 200 μm . The cavity length was approximately 15 mm.

Three different flat output couplers were used to test the function of the developed ISA. There are three employed OCs with different reflectivities at 1.06, 1.32, and 1.44 μm , respectively, as listed in **Tab. 3.3.1**.

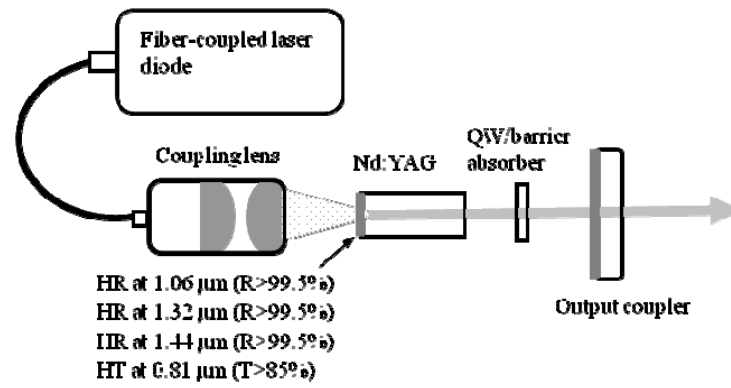


Fig. 3.3.1. Experimental schematic of the laser experiment.

mirrors	Reflectivity		
	1.06 μm	1.32 μm	1.44 μm
OC1	5%	30%	99%
OC2	50%	70%	95%
OC3	99.5%	69%	97%

Tab. 3.3.1. The employed OCs coatings with different reflectivities at 1.06, 1.32, and 1.44- μm , respectively.

3.3.2 Results and Discussion

Figure 3.3.2 shows the average output powers, with and without the ISA inserted into the cavity with the OC1, versus the incident pump power. The reduction in the slope efficiency due to the ISA can be seen to be rather small. With the Findlay–Clay analysis the insertion loss of the ISA is found to be approximately 0.2%. Note that the output efficiency with the OC1 is rather low because the output coupling is not optimal for the operation at 1.44 μm .

The second output coupler (OC2) was used to test the suppression ability of the ISA; its reflectivities at 1.06, 1.32, and 1.44 μm are 50%, 70%, and 95%, respectively. Experimental results reveal that the laser cavity with the OC2 and without the ISA is completely lasing at 1064 nm. With the insertion of the ISA, the laser cavity with the OC2 can be purely lasing at 1444 nm. **Figure 3.3.3** shows the input–output characteristics for the output powers with and without the ISA inserted into the cavity with the OC2. It can be seen that the ISA can make the laser cavity to change the lasing wavelength from 1.06 to 1.44 μm . An output power of 2.5W at 1.44 μm , with a slope efficiency of 23%, was achieved with the ISA inserted into the cavity with the OC2. At a pump power of 10W the present output power is up to 1.7W, which is superior to the previous data of 10W obtained with a 2% output coupler [44-45]. The superiority comes from the advantage that an output coupler with a higher transmission can be used to optimize the output power because of the strong suppression at 1.06 μm transition by the ISA. Finally, the third output coupler (OC3) was used to further investigate the maximum suppression ability of the ISA. The reflectivities of the OC3 at 1.32 and 1.44 μm are nearly the same as those of the OC2; however, the reflectivity of the OC3 at 1.06 μm is up to 99.5%. Experimental results reveal that the ISA can still suppress the 1.06 μm emission and lead to a Nd:YAG laser operating at 1.44 μm . More importantly, the output performance with the OC3 is almost the same as that obtained with the OC2, as seen in the inset of **Fig. 3.3.3**. In other words, the optimum output coupler at 1.44 μm can be straightforwardly designed by means of the ISA to suppress operation at 1.06 μm .

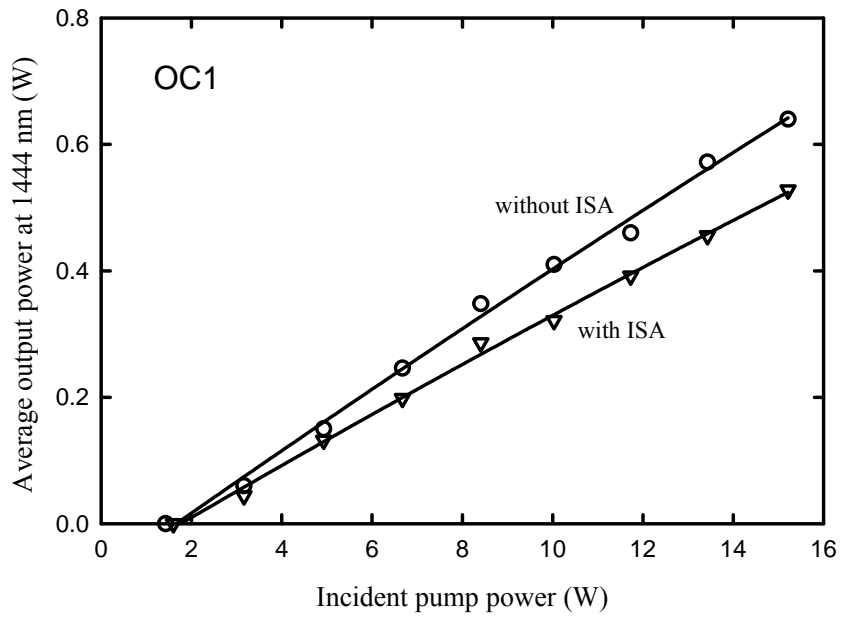


Fig. 3.3.2. Average output powers, with and without the ISA inserted into the cavity with the OC1, versus the incident pump power.

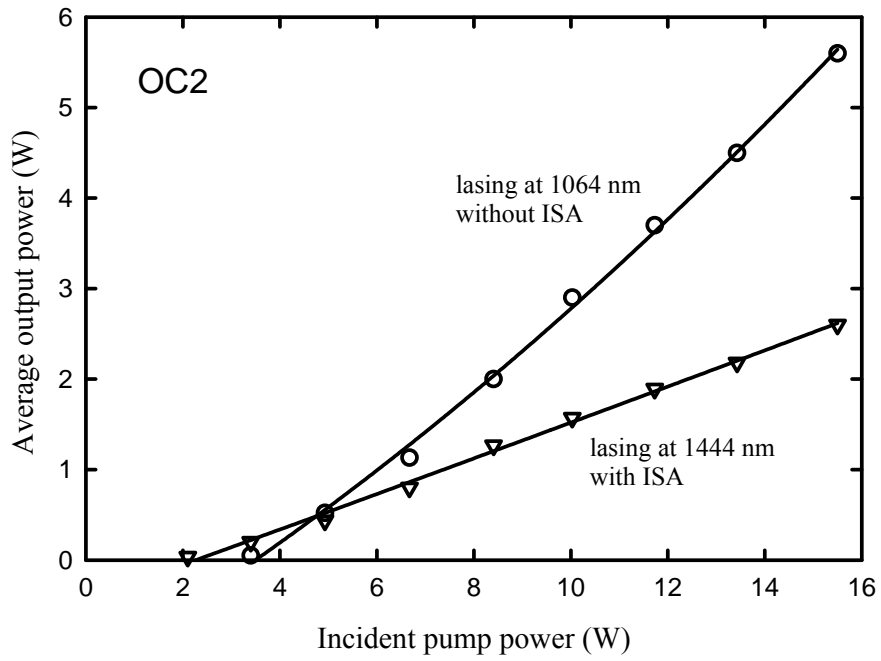


Fig. 3.3.3. Average output powers, with and without the ISA inserted into the cavity with the OC2, versus the incident pump power.

3.4 Conclusions

An AlGaInAs QW–barrier structure grown on a Fe-doped InP transparent substrate was developed to be an ISA for an efficient high-power Nd:YAG laser at 1.44 μm . Experimental results confirm that the developed ISA can still fully suppress the 1.06 μm oscillation even if the cavity mirrors have a high-reflection coating at 1.06 μm . With the ISA to suppress operation at 1.06 μm , the output coupler at 1.44 μm can be straightforwardly optimized. At a pump power of 16W, an output power of 2.5W at 1.44 μm , with a slope efficiency of 23%, was achieved.



References

- [1] K. Kopczynski, Z. Mierczyk, S. M. Kaczmarek, "Miniature, eye-safe solid-state lasers," Proc. SPIE Vol. **3186**, 292-295 (1997).
- [2] W. Koechner, *Solid-State Laser Engineering*, vol. 1, Optical Sciences, 6th ed., (Springer, Berlin, 2006).
- [3] S. Kück, K. Petermann, U. Pohlmann, U. Schönhoff, G. Huber, "Tunable room-temperature laser action of Cr⁴⁺-doped Y₃Sc_xAl_{5-x}O₁₂," Appl. Phys. B **58**, 153-156 (1994).
- [4] N. V. Kuleshov, A. A. Lagatsky, A. V. Podlipensky, V. P. Mikhailov, A. A. Kornienko, E. B. Dunina, S. Hartung, G. Huber, "Fluorescence dynamics, excited-state absorption and stimulated emission of Er³⁺ in KY(WO₄)₂," J. Opt. Soc. Am. B **15**, 1205-1212 (1998).
- [5] I. Sokólska, E. Heumann, S. Kück, T. Łukasiewicz, "Laser oscillation of Er³⁺:YVO₄ and Er³⁺, Yb³⁺:YVO₄ crystals in the spectral range around 1.6 μm," Appl. Phys. B **71**, 893-896 (2000).
- [6] A. Sennaroglu, "Broadly tunable Cr⁴⁺-doped solid-state lasers in the near infrared and visible," Prog. Quantum Electron. **26**, 287-352 (2002).
- [7] P. Cerný, H. Jelínková, P. Zverev, T. T. Basiev, Solid state lasers with Raman frequency conversion. Prog. Quantum Electron. **28**, 113-143 (2004).
- [8] Y. F. Chen, "Compact efficient all-solid-state eye-safe laser with self-frequency Raman conversion in a Nd:YVO₄ crystal," Opt. Lett. **29**, 2172-2174 (2004).

- [9] Y. F. Chen, "Efficient 1521-nm Nd:GdVO₄ Raman laser," *Opt. Lett.* **29**, 2632-2634 (2004).
- [10] J. T. Murray, R. C. Powell, D. Smith, W. Austin, R. A. Stolzenberger, "Generation of 1.5 μm radiation through intracavity solidstate Raman shifting in Ba(NO₃)₂ nonlinear crystals," *Opt. Lett.* **20**, 1017-1019 (1995).
- [11] A. Agnesi, S. Dell'Acqua, G. Reali, "Diode-pumped quasi-cw intracavity optical parametric oscillator at 1.57 μm with efficient pulse shortening," *Appl. Phys. B* **70**, 751-753 (2000).
- [12] Y. F. Chen, S. W. Chen, Y. C. Chen, Y. P. Lan, S. W. Tsai, "Compact efficient intracavity optical parametric oscillator with a passively Q-switched Nd:YVO₄/Cr⁴⁺:YAG laser in a hemispherical cavity," *Appl. Phys. B* **77**, 493-495 (2003).
- [13] Y. F. Chen, L. Y. Tsai, "Comparison between shared and coupled resonators for passively Q-switched Nd:GdVO₄ intracavity optical parametric oscillators," *Appl. Phys. B* **82**, 403-406 (2006).
- [14] Y. F. Chen, "Design criteria for concentration optimization in scaling diode end-pumped lasers to high powers: influence of thermal fracture," *IEEE J. Quantum Electron.* **35**, 234-239 (1999).
- [15] H. J. Zhang, X. L. Meng, L. Zhu, H. Z. Zhang, P. Wang, J. Dawes, C. Q. Wang, Y. T. Chow, "Investigation on the growth and laser properties of Nd:GdVO₄ single crystal," *Cryst. Res. Technol.* **33**, 801-806 (1998).
- [16] T. Ogawa, Y. Urata, S. Wada, K. Onodera, H. Machida, H. Sagae, M. Higuchi, K. Kodaira, "Efficient laser performance of Nd:GdVO₄ crystals grown by the floating zone method," *Opt. Lett.* **28**, 2333-2335 (2003).

- [17] V. Lupei, N. Pavel, Y. Sato, T. Taira, "Highly efficient 1063-nm continuous-wave laser emission in Nd:GdVO₄," *Opt. Lett.* **28**, 2366-2368 (2003).
- [18] J. Minch, S. H. Park, T. Keating, S. L. Chuang, "Theory and experiment of In_{1-x-y}Ga_xAs_yP_{1-y} and In_{1-x-y}Ga_xAl_yAs long-wavelength strained quantum-well lasers," *IEEE J. Quantum Electron.* **35**, 771-782 (1999).
- [19] J. P. Donnelly, J. N. Walpole, S. H. Groves, R. J. Bailey, L. J. Missaggia, A. Napoleone, R. E. Reeder, C. C. Cook, "1.5- μ m tapered-gain region lasers with high-CW output powers," *IEEE Photon. Technol. Lett.* **10**, 1377-1379 (1998).
- [20] N. Nishiyama, C. Caneau, B. Hall, G. Guryanov, M. H. Hu, X. S. Liu, M.-J. Li, R. Bhat, C. E. Zah, "Long-wavelength vertical cavity surface-emitting lasers on InP with lattice matched AlGaInAs-InP DBR grown by MOCVD," *IEEE J. Sel. Top. Quantum Electron.* **11**, 990-998 (2005).
- [21] S. R. Šelmić, G. A. Evans, T. M. Chou, J. B. Kirk, J. N. Walpole, J. P. Donnelly, C. T. Harris, L. J. Missaggia, "Single frequency 1550-nm AlGaInAs-InP tapered high-power laser with a distributed Bragg reflector," *IEEE Photon. Technol. Lett.* **14**, 890-892 (2002).
- [22] S.C. Huang · H.L. Chang · K.W. Su · A. Li · S.C. Liu · Y.F. Chen · K.F. Huang, "AlGaInAs/InP eye-safe laser pumped by a Q-switched Nd:GdVO₄ laser," *Appl. Phys. B* **94**, 483-487(2009).
- [23] H. L. Chang, S. C. Huang, Yi-Fan Chen, K. W. Su, Y. F. Chen, and K. F. Huang, "Efficient high-peak-power AlGaInAs eye-safe wavelength disk laser with optical in-well pumping," *Opt. Express* **17**, 11409-11414 (2009).
- [24] J. Marling, "1.05-1.44 μ m Tunability and performance of the CW Nd³⁺:YAG laser," *IEEE J. Quantum Electron.* **14**, 56-62 (1978).

- [25] H. M. Kretschmann, F. Heine, V. G. Ostroumov, and G. Huber, "High-power diode-pumped continuous-wave Nd³⁺ lasers at wavelengths near 1.44 μm," *Opt. Lett.* **22**, 466-468 (1997).
- [26] A. Agnesi, S. Dell'Acqua, C. Pennacchio, G. Reali, and P. G. Gobbi, "High-Repetition-Rate Q-Switched Diode-Pumped Nd:YAG Laser at 1.444 μm," *Appl. Opt.* **37**, 3984-3986 (1998).
- [27] N. Hodgson, W. L. Nighan, Jr., D. J. Golding, and D. Eisel, "Efficient 100-W Nd:YAG laser operating at a wavelength of 1.444 μm," *Opt. Lett.* **19**, 1328-1330 (1994).
- [28] S. K. Wong, P. Mathieu, and P. Pace, "Eyesafe Nd:YAG laser," *Appl. Phys. Lett.* **57**, 650-652 (1990).
- [29] A. Perez-Maldonado, T. M. Runger, N. Krejci-Papa, "The 1450-nm diode laser reduces sebum production in facial skin: A possible mode of action of its effectiveness for the treatment of acne vulgaris," *Lasers Surg. Med.* **39**, 189-192 (2007).
- [30] V. A. Narurkar, "Lasers, Light Sources, and Radiofrequency Devices for Skin Rejuvenation," *Semin. Cutan. Med. Surg.* **25**, 145-150 (2006).
- [31] S. Hohenleutner, K. Koellner, S. Lorenz, M. Landthaler, U. Hohenleutner, "Results of nonablative wrinkle reduction with a 1,450-nm diode laser: Difficulties in the assessment of "subtle changes," *Lasers Surg. Med.* **37**, 14-18 (2005).
- [32] S. N. Doshi, T. S. Alster, "Combination radiofrequency and diode laser for treatment of facial rhytides and skin laxity," *Journal of Cosmetic and Laser Therapy* **000**, 1-5 (2005).

- [33] S. N. Doshi, T. S. Alster, "1,450 nm Long-Pulsed Diode Laser for Nonablative Skin Rejuvenation," *Dermatol. Surg.* **31**, 1223-1226 (2005).
- [34] D. No, M. McClaren, V. Chotzen, S. L. Kilmer "Sebaceous hyperplasia treated with a 1450-nm diode laser," *Dermatol. Surg.* **30**, 382-384 (2004).
- [35] E. L. Tanzi, T. S. Alster, "Comparison of a 1450-nm Diode Laser and a 1320-nm Nd:YAG Laser in the Treatment of Atrophic Facial Scars: A Prospective Clinical and Histologic Study," *Dermatol. Surg.* **30**, 152-157 (2004).
- [36] D. J. Goldberg, A. S. Rogachefsky, S. Silapunt, "Non-ablative laser treatment of facial rhytides: A comparison of 1450-nm diode laser treatment with dynamic cooling as opposed to treatment with dynamic cooling alone," *Lasers Surg. Med.* **39**, 79-81 (2002).
- [37] J. Eichler, T. Seiler, *Lasertechnik in der Medizin* (Springer-Verlag, Stuttgart) 38-47 (1993).
- [38] V. Klimov, I. A. Shcherbakov, and V. B. Tsvetkov, "Losses in 1.44- μm Nd:YAG laser for medical applications," *Proc. SPIE Int. Soc. Opt. Eng.* **3829**, 165-179 (1999).
- [39] C. E. Zah, R. Bhat, B. N. Pathak, F. Favire, W. Lin, M. C. Wang, N. C. Andreadakis, D. M. Hwang, M. A. Koza, T. P. Lee, Z. Wang, D. Darby, D. Flanders, and J. J. Hsieh, "High-performance uncooled 1.3- μm $\text{Al}_x\text{Ga}_y\text{In}_{1-x-y}\text{As}/\text{InP}$ strained-layer quantum-well lasers for subscriber loop applications," *IEEE J. Quantum Electron.* **30**, 511-521 (1994).
- [40] N. Nishiyama, C. Caneau, B. Hall, G. Guryanov, M. H. Hu, X. S. Liu, M.-J. Li, R. Bhat, and C. E. Zah, "Long-wavelength vertical-cavity surface-emitting lasers

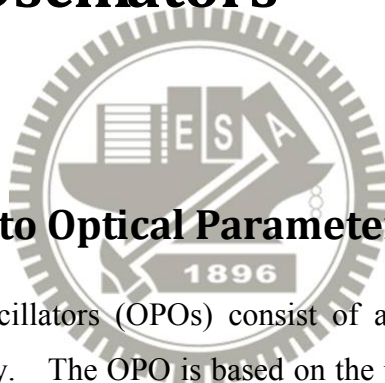
- on InP with lattice matched AlGaInAs–InP DBR grown by MOCVD,” IEEE J. Sel. Topics Quantum Electron **11**, 990-998 (2005).
- [41] O. Hanaizumi, K. T. Jeong, S. Y. Kashiwada, I. Syuaib, K. Kawase, and S. Kawakami, “Observation of gain in an optically pumped surface-normal multiple-quantum-well optical amplifier,” Opt. Lett. **21**, 269-271 (1996).
- [42] K. W. Su, S. C. Huang, A. Li, S. C. Liu, Y. F. Chen, and K. F. Huang, “High-peak-power AlGaInAs quantum-well 1.3- μm laser pumped by a diode-pumped actively Q-switched solid-state laser,” Opt.Lett. **31**, 2009-2011 (2006).
- [43] S. C. Huang, S. C. Liu, A. Li, K. W. Su, Y. F. Chen, and K. F. Huang, “AlGaInAs quantum-well as a saturable absorber in a diode-pumped passively Q-switched solid-state laser,” Opt. Lett. **32**, 1480-1482 (2007)
- [44] H. M. Kretschmann, F. Heine, V. G. Ostroumov, and G. Huber, “High-power diode-pumped continuous-wave Nd³⁺ lasers at wavelengths near 1.44 μm ”, Opt. Lett. **22**, 466-468 (1997).
- [45] A. Agnesi, S. Dell’Acqua, C. Pennacchio, G. Reali, and P. G. Gobbi, “High-Repetition-Rate Q-Switched Diode-Pumped Nd:YAG Laser at 1.444 μm ,” Appl. Opt. **37**, 3984-3986 (1998).

Chapter 4

Design Models and Experiments for

Millijoule Intracavity Optical

Parameter Oscillators



4.1 Introduction to Optical Parameter Oscillator (OPO)

Optical Parameter Oscillators (OPOs) consist of a nonlinear crystal which is inserted in a resonant cavity. The OPO is based on the parametric interaction which is a second-order nonlinear effect. The optical parameter process belongs to three-photon process, as shown in **Fig. 4.1.1 (a)**. When one high-frequency (shorter-wavelength) is chosen, the pump photon breaks down and converts into two lower-frequency photons. Three optical fields called pump, signal and idler with frequencies ω_p , ω_s and ω_i , respectively. They are related by the energy conservation condition:

$$\omega_p = \omega_s + \omega_i .$$

The energy-level diagram of the optical parameter process is shown in **Fig. 4.1.1 (b)**. The top energy level can be chosen by the pump frequency. The middle energy level, the difference between ω_s and ω_i , can be tuned by a phase matching condition.

It is worth to be mentioned that the signal wave is amplified by the nonlinear mixing process, and an idler wave is generated by the process. The gain related to the process of optical parametric amplification (OPA) can be used to form an optical resonator with mirrors placed on the sides of the nonlinear medium, which is known as an OPO. If the end mirrors of an OPO cavity are highly reflecting at both frequencies ω_s and ω_i , it is called a doubly resonant oscillator (DRO). On the other hand, if they are highly reflecting at frequencies ω_s or ω_i but not both, it is known as a singly resonant oscillator (SRO). Configurations for parametric interactions are shown in **Fig. 4.1.2**.

The tunable properties of an OPO have to simultaneously satisfy the energy-conservation condition and momentum conservation condition. To maximize the conversion efficiency, a phase-matching condition (momentum conservation relation) has to be fulfilled by the three fields

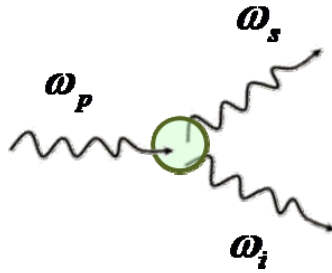
$$\vec{k}_p = \vec{k}_s + \vec{k}_i .$$

Most of the OPO crystals allow birefringence phase-matching. The fields are polarized along the ordinary or the extraordinary direction. The difference between the corresponding indices compensates for the index wavelength dispersion. Two kinds of phase-matching configurations are encountered, as shown in **Fig. 4.1.3**. In type I, the signal and idler field polarizations are parallel to each other and are perpendicular to that of the pump. The other kind of phase-matching is type II phase-matching, i.e. the signal and idler fields have crossed polarizations: (i) the pump and signal fields have parallel polarizations; (ii) the pump and idler fields have parallel polarizations.. An example of type II phase-matching is KTP (KTiOPO₄). The angle tuning curve of type II KTP in the YZ plane for a pump wavelength of 1064 nm is shown in **Fig. 4.1.4 (a)**. For type II x-cut KTP, the signal wavelength with respect to pump wavelength is shown in **Fig. 4.1.4 (b)**. Based on the tuning characteristics from the phase matching conditions, OPOs are tunable over a broad range from the visible to the far infrared, as shown in **Fig. 4.1.5** [1]. In addition, OPOs have the advantages such as the matured technology of pumping lasers and high

efficiency approaching quantum limit. Therefore, to generate eye-safe lasers, OPO should be a good and efficient method.



(a)



(b)

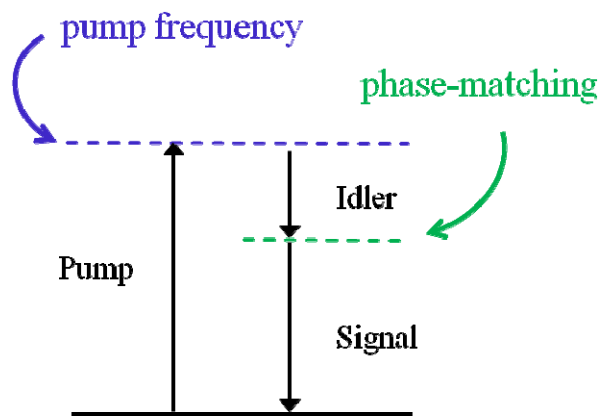
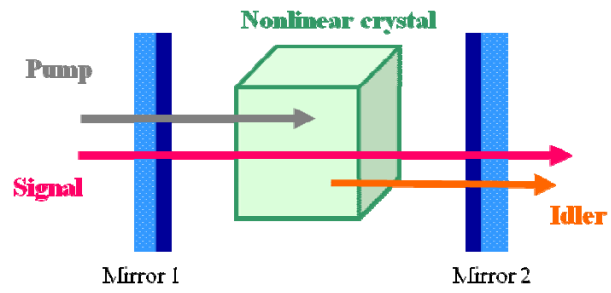
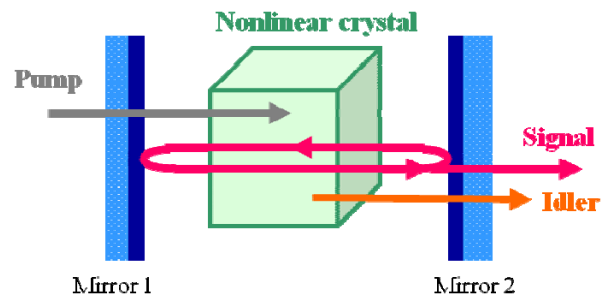


Fig.4.1.1. (a) Diagram of three photons interaction in optical parametric process. (b) The energy-level diagram of the optical parametric process.

(a)



(b)



(c)

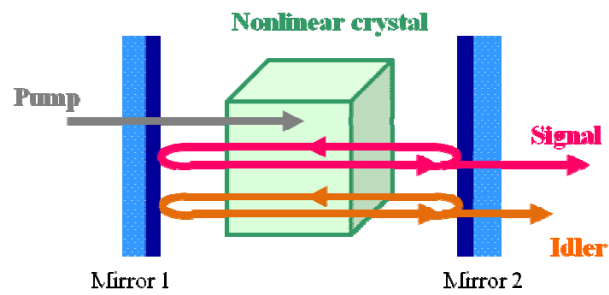
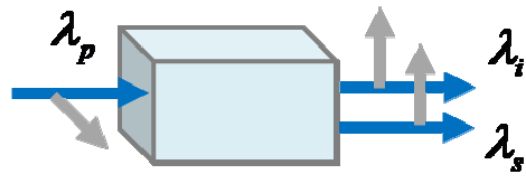


Fig.4.1.2. Configurations for parametric interactions: (a) OPA; (b) SRO; (c) DRO.

(a)



(b)

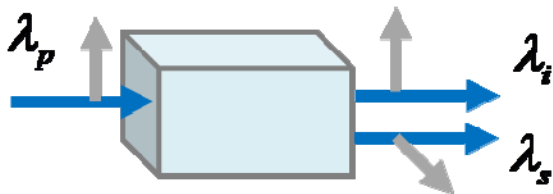
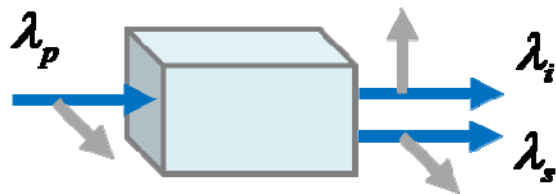


Fig. 4.1.3. Phase-matching configuration of OPOs: (a) type I; (b) type II.

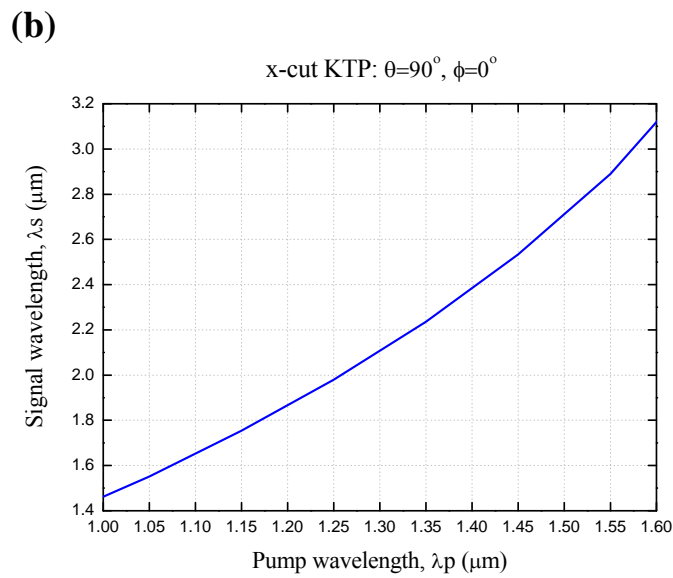
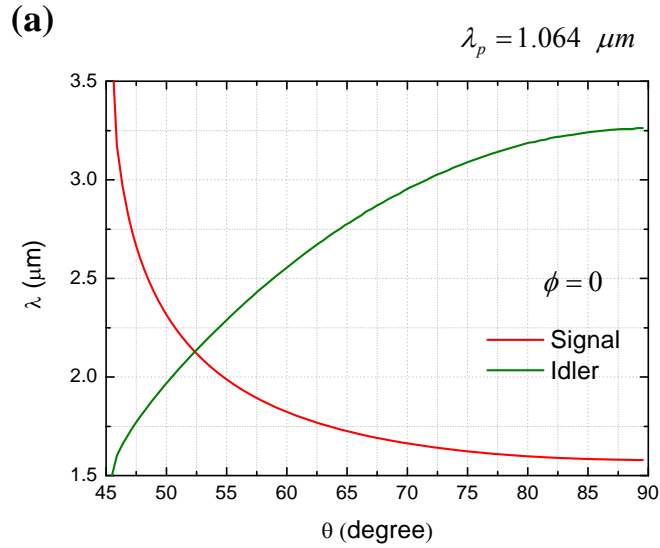


Fig. 4.1.4. (a) Angle tuning curve of type II x-cut KTP for a pump wavelength of 1064 nm. (b) The signal wavelength with respect to pump wavelength for type II x-cut KTP.

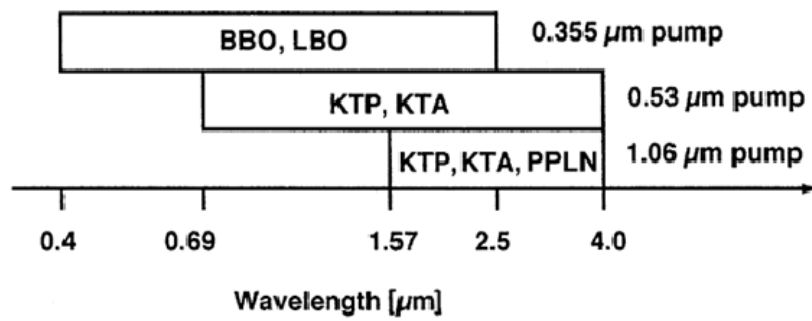
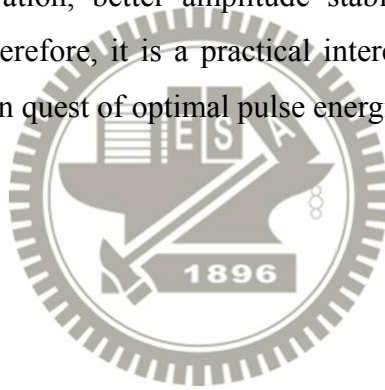


Fig. 4.1.5. Wavelength coverage of Nd:YAG or Nd:YLF pumped OPOs [1].

4.2 Cavity Configurations of Intracavity OPOs

There are two kinds of OPOs; one is extracavity OPO (EOPO), and another is intracavity OPO. In an EOPO, the output coupler of the fundamental laser cavity has to be optimized to maximum output power. IOPO has the advantage of a high power level within the oscillator to allow a low threshold and high efficiency compared to an EOPO.

In 1978, Ammann has proposed a shared resonator configuration for intracavity Raman oscillation [2]. The shared cavity (two mirrors) and coupled cavity (three mirrors) configurations are shown in **Fig. 4.2.1**. Recently, Chen et al. [3] reported the investigation for IOPO revealed the shared cavity provides many advantages including simpler configuration, better amplitude stability, and higher parametric conversion efficiency. Therefore, it is a practical interest to explore an intracavity OPO in a shared resonator in quest of optimal pulse energies and peak powers.



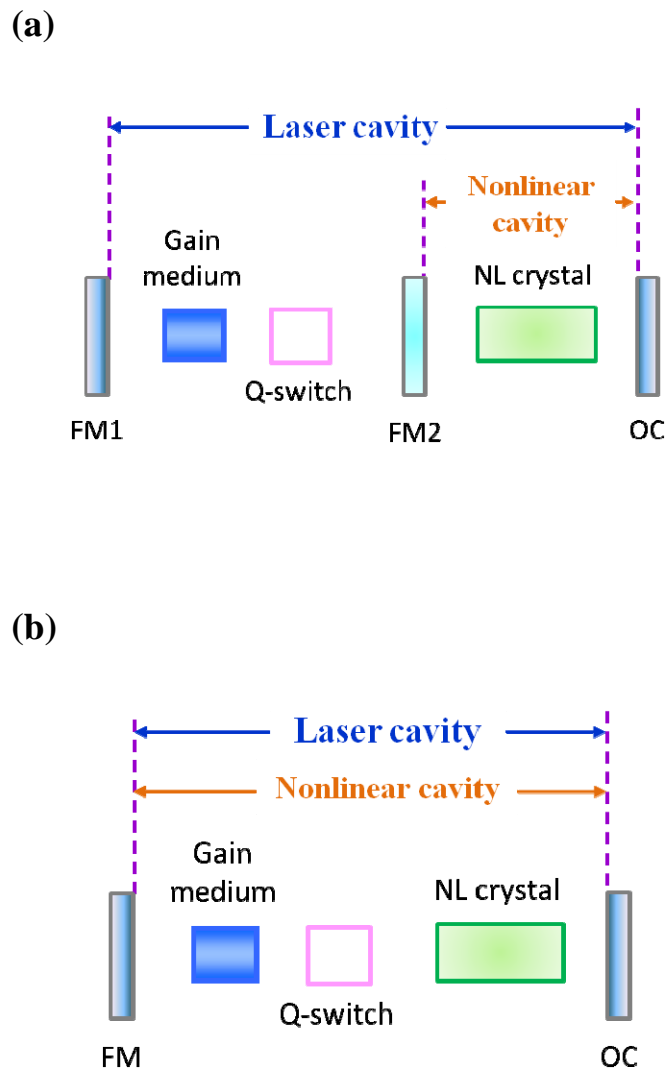
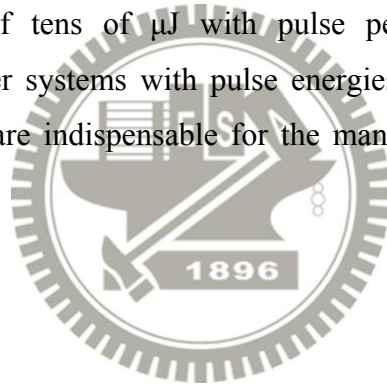


Fig. 4.2.1. Schematic of two kinds of configurations: (a) coupled cavity; (b) shared cavity.

4.3 Subnanosecond Eye-Safe Intracavity OPO

Intracavity OPO has been proposed several decades ago [4-6], but it was restricted by the development of nonlinear crystals. The advent of high damage threshold nonlinear crystals and diode-pumped Nd-doped lasers leads to a renaissance of interest in IOPOs. KTP-based IOPOs pumped by Nd-doped lasers at around 1050-1070 nm generate signal wavelengths around 1.55 μm [7-9]. One advantage of the KTP family is the non-critical phase-matching (NCPM) that allows a good OPO conversion efficiency even with poor-beam-quality pump lasers. Another advantage is the large available crystal size that allows the generation of high energies. In recent years, a number of efficient eye-safe intracavity OPOs pumped by actively [10-12] or passively [13-15] Q-switched Nd-doped lasers have been demonstrated to produce pulse energies of tens of μJ with pulse peak powers of 1-100 kW. Nevertheless, eye-safe laser systems with pulse energies in the mJ range and peak powers greater than MW are indispensable for the many long-distance applications [16-20].



4.3.1 Experimental Setup

Figure 4.3.1 shows the experimental setup for an intracavity OPO pumped by a high-power quasi-continuous-wave (QCW) diode-pumped passively Q-switched Nd:YAG laser in a shared resonator. The fundamental laser cavity was formed by a coated Nd:YAG crystal and an output coupler. The OPO cavity entirely overlapped with the fundamental laser cavity. The pump source is a high-power QCW diode stack (Quantel Laser Diodes) that consists of three 10-mm-long diode bars generating 130 W per bar, for a total of 390 W at the central wavelength of 808 nm. The diode stack is designed with 0.4 mm spacing between the diode bars so the overall area of emission is approximately 10 mm (slow axis) \times 0.8 mm (fast axis). The full divergence angles in the fast and slow axes are approximately 35° and 10°, respectively. A lens duct was exploited to couple the pump light from the diode stack into the laser crystal. The geometric parameters of a lens duct include r , L , $H1$, $H2$, and $H3$, where r is the radius of the input surface, L is the length of the duct, $H1$ is the width of the input surface, $H2$ is the width of the output surface, and $H3$ is the thickness of the duct. Here a lens duct with the parameters of $r = 10$ mm, $L = 32$ mm, $H1 = 12$ mm, $H2 = 2.7$ mm, and $H3 = 2.7$ mm was manufactured and used in the experiment. The coupling efficiency of this lens duct is found to be approximately 85%.

The gain medium was a 1.0 at. % Nd:YAG crystal with a diameter of 5 mm and a length of 10 mm. The incident surface of the laser crystal was coated to be highly reflective at 1064 nm and 1573 nm ($R > 99.8\%$) and highly transmitted at the pump wavelength of 808 nm ($T > 90\%$). The other surface of the laser crystal was coated to be antireflective at 1064 nm and 1573 nm ($R < 0.2\%$). The nonlinear material for the intracavity OPO was an x-cut KTP crystal with a size of $4 \times 4 \times 20$ mm³. The saturable absorber for the passive Q-switching was a Cr⁴⁺:YAG crystal with a thickness of 3 mm and an initial transmission of 60% at 1064 nm. Both surfaces of the KTP and Cr⁴⁺:YAG crystals were coated for antireflection at 1573 nm and 1064 nm. All crystals were wrapped with indium foil and mounted in conductively cooled copper blocks. The output coupler had a dichroic coating that was highly reflective at 1064

nm ($R > 99.8\%$) and partially reflective at 1573 nm. Several output couplers with different reflectivities ($10\% \leq R_s \leq 70\%$) at 1573 nm were used in the experiment to investigate the output optimization. The total cavity length was approximately 5.5 cm. The pulse temporal behavior at 1063 nm and 1571 nm was recorded by a LeCroy digital oscilloscope (Wavepro 7100; 10 G samples/sec; 1 GHz bandwidth) with a fast InGaAs photodiode. In all investigations, the diode stack was derived to emit optical pulses 250 μ s long, at a repetition rate less than 40 Hz, with a maximum duty cycle of 1%.



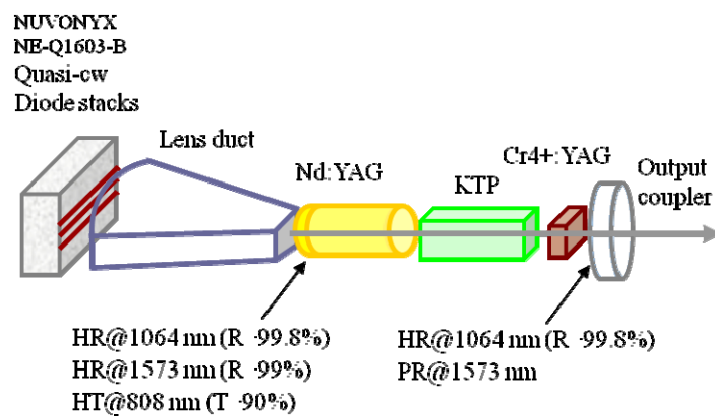


Fig. 4.3.1. Experimental setup for an intracavity OPO pumped by a high-power QCW diode-pumped passively Q-switched Nd:YAG laser in a shared resonator.

4.3.2 Theoretical Analysis

The advantage of the intracavity OPO mainly consists in the exploit of high photon density of the fundamental wave. First of all, we analyze the maximum value of the intracavity photon density for the fundamental wave in a passively Q-switched laser. Next, we verify that the intracavity photon density of the present laser can exceed the threshold of a singly resonant intracavity OPO in a shared cavity by far, even when the reflectivity of the output mirror at the signal wavelength is nearly zero. In a passively Q-switched laser with a fast Q-switching condition, the maximum value of the intracavity photon density of the fundamental wave can be expressed as [21]

$$\varphi_{f,\max} = \frac{l_{gm}}{l_{cav}} \left\{ n_i - n_t \left[1 + \ln \left(\frac{n_i}{n_t} \right) \right] \right\} \quad (1)$$

where

$$n_i = \frac{1}{2\sigma l_{gm}} \left[\ln(1/T_o^2) + \ln(1/R) + L \right] ;$$

$$n_t = \frac{1}{2\sigma l_{gm}} \left[\beta \ln(1/T_o^2) + \ln(1/R) + L \right] ;$$

$$\beta = \frac{\sigma_{es}}{\sigma_{gs}} ;$$

n_i is the initial population density in the gain medium; σ is the stimulated emission cross section of the gain medium; l_{gm} is the length of the gain medium; l_{cav} is the cavity length; T_o is the initial transmission of the saturable absorber; σ_{gs} and σ_{es} are the ground-state and excited-state absorption cross sections in the saturable absorber,

respectively; R is the reflectivity of the output mirror at the fundamental wavelength; and L is the nonsaturable intracavity round-trip loss. With the properties of the Nd:YAG and Cr⁴⁺:YAG crystals and the typical cavity parameters: $\sigma = 2.8 \times 10^{-19} \text{ cm}^2$, $\sigma_{gs} = 8.7 \times 10^{-19} \text{ cm}^2$, $\sigma_{es} = 2.2 \times 10^{-19} \text{ cm}^2$, $l_{cav} = 5.5 \text{ cm}$, $R = 99.8\%$, $T_o = 0.6$, and $L = 0.01$, it can be found that $\varphi_{f,max}$ can be up to $1.56 \times 10^{17} \text{ cm}^{-3}$.

With Brosnan and Byer's equation [22], the threshold photon density for the double-pass pumped, single resonant OPO is derived to be given by

$$\varphi_{f,th}(R_s) = \left(\frac{8 \hbar \omega_3 \omega_1 \omega_2 d_{eff}^2 l_{nl}^2}{n_3 n_1 n_2 \varepsilon_0 c^2} \right)^{-1} \left[\ln \left(\frac{1}{R_s} \right) + L_s \right] \quad (2)$$

with the gain coefficient

$$G = \frac{8 \hbar \omega_3 \omega_1 \omega_2 d_{eff}^2 l_{nl}^2}{n_3 n_1 n_2 \varepsilon_0 c^2} \varphi_f \quad (3)$$

where g_s is the mode coupling coefficient, γ is the ratio of backward to forward pump amplitude in the cavity; ω_1 , ω_2 and ω_3 are the signal, idler and pump frequencies, respectively; n_2 and n_3 are the refractive indices at the signal, idler and pump wavelengths, respectively; τ_p is the FWHM of the pump pulse; d_{eff} is the effective non-linear coefficient; ε_0 is the vacuum permittivity; c is the speed of light; l_{nl} is the length of the nonlinear crystal; L_s is the round-trip signal wave intensity loss in the cavity; and R_s is the output reflectivity at the signal wavelength.

Fig. 4.3.2 depicts the calculated results for the dependence of the threshold photon density $\varphi_{f,th}(R_s)$ on the output reflectivity R_s with the properties of the KTP crystal and the typical cavity parameters: $\omega_1 = 1.198 \times 10^{15} \text{ sec}^{-1}$, $\omega_2 = 5.712 \times 10^{14} \text{ sec}^{-1}$, $\hbar \omega_3 = 1.865 \times 10^{-19} \text{ J}$, $d_{eff} = 3.64 \text{ pm/V}$, $l_{nl} = 20 \text{ cm}$, $n_1 = 1.737$, $n_2 = 1.771$, $n_3 = 1.748$, $\varepsilon_0 = 8.854 \text{ pF/m}$, $L_s = 0.01$, and $c = 3 \times 10^8 \text{ m/s}$. It can be seen that the threshold photon density $\varphi_{f,th}$ increases from $1.9 \times 10^{13} \text{ cm}^{-3}$ to $5.6 \times 10^{15} \text{ cm}^{-3}$ for the reflectivity R_s varying from 99.9% to 0.1%. As analyzed earlier, the obtainable intracavity photon

density of the fundamental wave generally exceeds 10^{17} cm^{-3} . Therefore, the intracavity OPO for any value of R_s can be promisingly generated in the shared cavity, as long as the pump energy can excite the fundamental wave to bleach the saturable absorber and to overcome the lasing threshold.



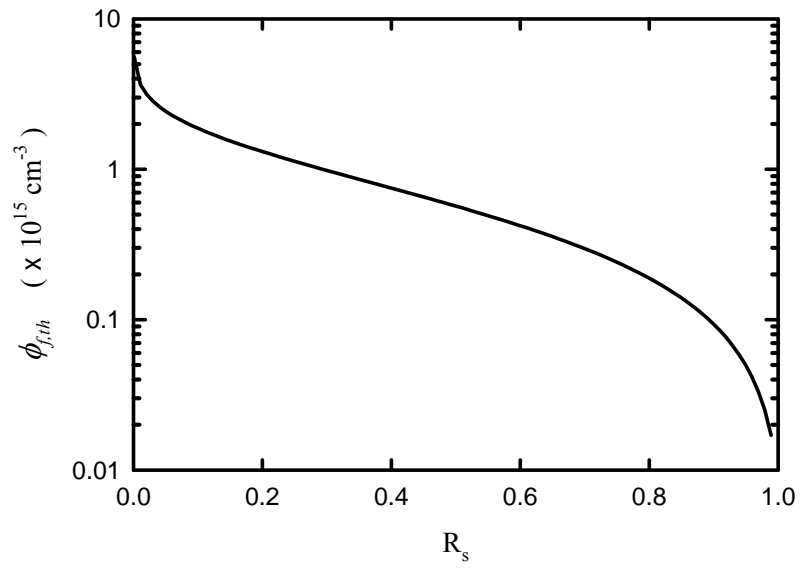


Fig. 4.3.2. Calculated results for the dependence of the threshold photon density on the output reflectivity R_s .

4.3.3 Results and Discussion

Fig. 4.3.3 shows the experimental results for the threshold pump energy versus the OPO output reflectivity. Experimental results confirm that the threshold pump energy is determined by the bleach of the saturable absorber not by the signal output reflectivity. Consequently, a wide range of the signal output reflectivity can be used to optimize the output performance. **Fig. 4.3.4** depicts the experimental results for the pulse energy of the signal output versus the signal output reflectivity. The optimal output reflectivity for the output pulse energy can be found to be within $R_s = 40\text{--}50\%$. With the optimum output coupler, the conversion efficiency from the diode input energy to the signal output energy is approximately 7%, which is slightly superior to the efficiency of 4–6% obtained in a coupled cavity [23].

Figures 4.3.5 (a)-(c) show the experimental results for the temporal shapes of the fundamental and the signal pulses obtained with three different output couplers. It can be seen that the pulse durations of the signal output are 4.4 ns, 2.1 ns, and 0.85 ns for $R_s = 60\%$, 50%, and 15%, respectively. The pulse width obtained with $R_s = 15\%$ is 2.4 times shorter than that obtained with $R_s = 50\%$; however, the pulse energy is only 20% less than the maximum value. In other words, the peak power reached with $R_s = 15\%$ can be nearly two times higher than that obtained with $R_s = 50\%$. To be more accurate, the output peak power was calculated with the experimental pulse energy and the numerical integration of the measured temporal pulse profile. **Figure 4.3.6** depicts the experimental results for the peak power of the signal output versus the OPO output reflectivity. The optimal output reflectivity for the output peak power can be found to be within $R_s = 10\text{--}20\%$. With the optimum output coupler, the maximum peak power can be up to 1.5 MW.

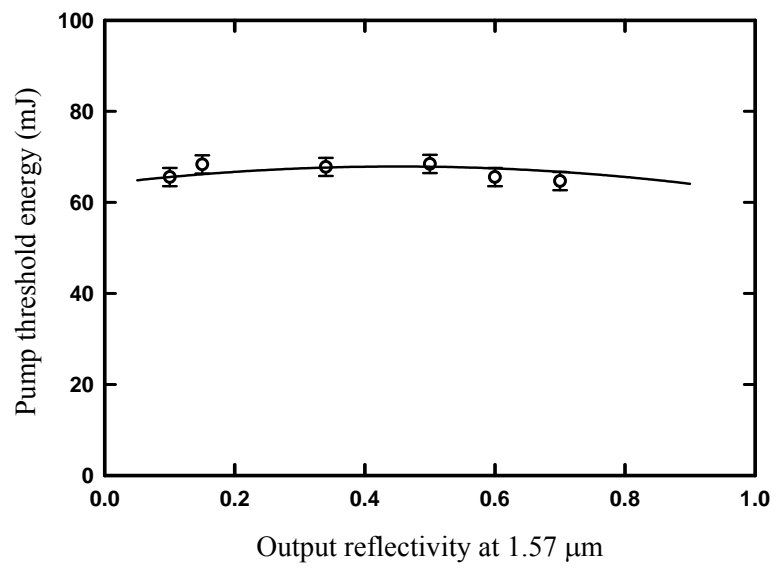


Fig. 4.3.3. Experimental results for the threshold pump energy versus the OPO output reflectivity.

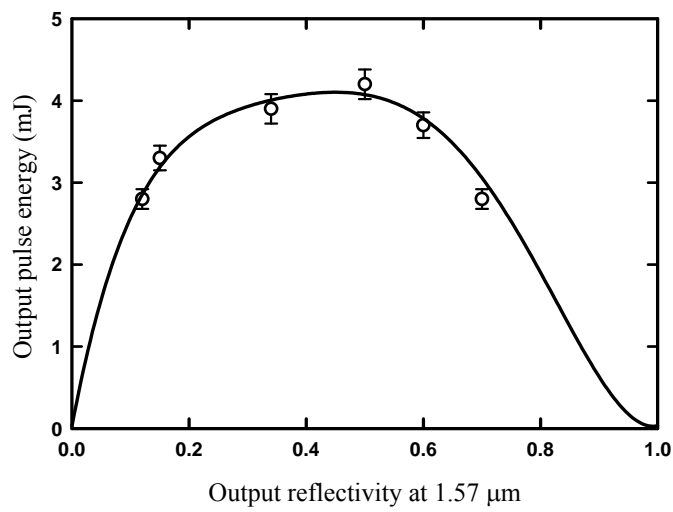


Fig. 4.3.4. Experimental results for the pulse energy of the signal output versus the OPO output reflectivity.

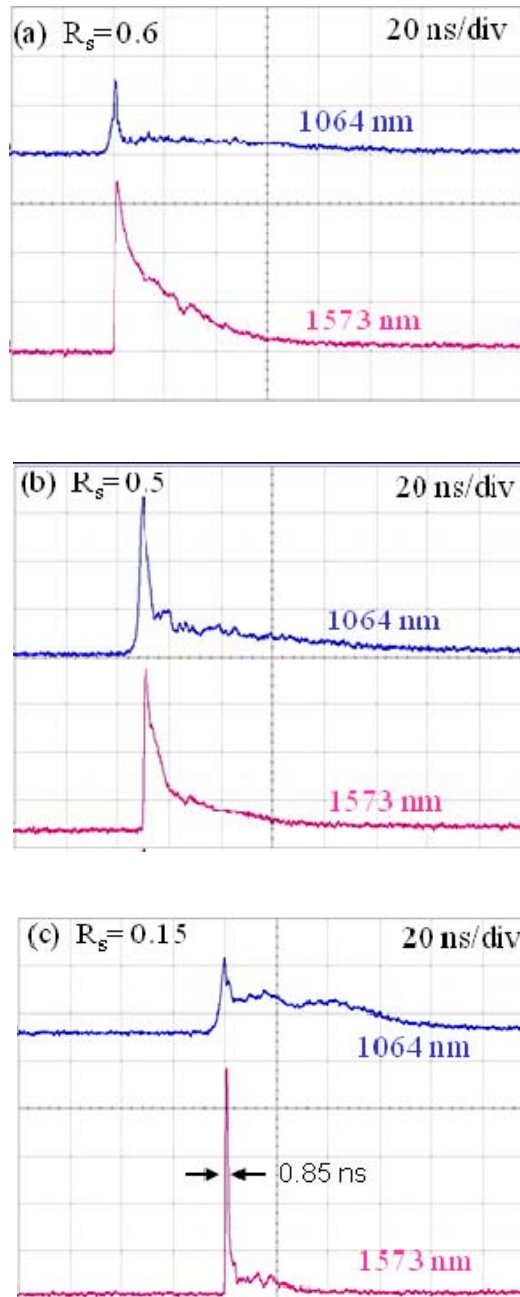


Fig. 4.3.5. Experimental results for the temporal shapes of the fundamental and the signal pulses.

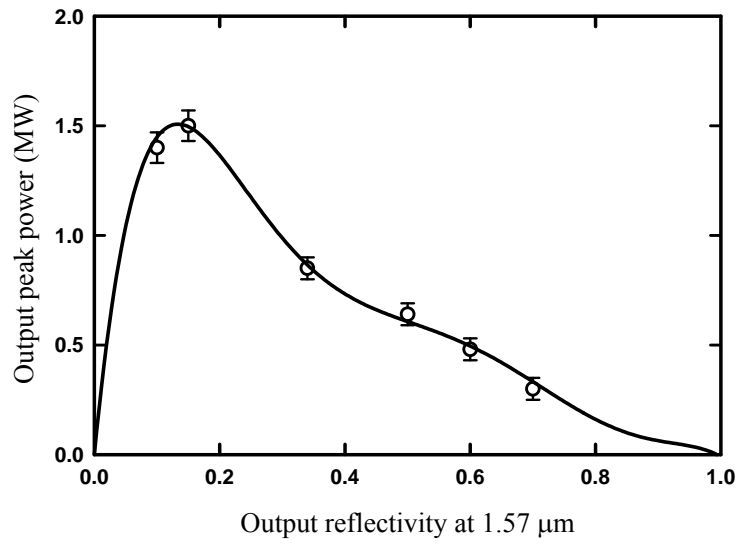


Fig. 4.3.6. Experimental results for the peak power of the signal output versus the OPO output reflectivity.

4.4 Analytical Model for Simultaneous Emission of Fundamental and Signal Waves

The OPO device is simple and provides the wavelength tenability to eye-safe region by phase matching condition [24-26]. The dual-signal OPOs generated in the eye-safe wavelength region, utilizing the quasi-phase-matched periodically poled crystals, have been realized [27,28]. High-pulse-energy solid-state lasers combined with Nd³⁺-doped lasers operating near 1.0 μm and OPO converted eye-safe lasers are potentially valuable for some applications, especially in target ranging of airborne laser systems. The attainment of high-pulse-energy laser increases the risk of optical damage to cavity components because higher pump level is required to exceed pump threshold. Therefore, the demand for damage threshold of the coatings becomes severer.

Intracavity singly-resonant OPO (SRO) takes the advantages of high photon density of fundamental wave, and the good spatial overlapping of fundamental laser and OPO signal. Moreover, the use of output mirrors with partial reflection at fundamental laser instead of a highly reflective mirror is not only to generate a dual-wavelength laser but also to reduce the risk of optical damage [29]. Rate-equation model for the passively Q-switched IOPO has been used to analyze the temporal behavior of fundamental laser and OPO signal pulses [30,31]. The output energy characteristic of the simultaneous emission including the fundamental laser and the OPO signal, however, has not been analyzed and modeled. Nevertheless, to the best of our knowledge, the systematic investigation of the simultaneous emission based on an intracavity SRO has not also been performed.

In this part, we firstly use the rate-equation model of a passively Q-switched IOPO to calculate the output pulse energies of the fundamental laser and OPO signal as functions of the initial transmission of the saturable absorber and the reflectivity at the fundamental laser wavelength. With a nonlinear regression fit to the numerical calculations, we extend the analytical expression for the pulse energy of passively Q-switched lasers reported by Chen *et al.* [32] to develop an analytical model for the

output pulse energies of passively Q-switched IOPOs including both the fundamental laser and the OPO signal. To verify the accuracy of the analytical model, based on a passively Q-switched IOPO using a Cr^{4+} :YAG crystal as the saturable absorber, simultaneous generation of the fundamental laser output at $1.06 \mu\text{m}$ and the OPO signal at $1.57 \mu\text{m}$ is performed. Various output couplers with different reflectivity at the fundamental laser wavelength, R , are employed to systematically investigate the variation of the output pulse energies of both fundamental laser and OPO signal wavelengths. Experimental results show that the output energy characteristic of a dual-wavelength (fundamental laser/OPO signal) laser agrees very well with the present model. The present model provides design criteria of the dual-wavelength laser with a passively Q-switched intracavity OPO.



4.4.1 Theoretical Analysis

In **Section 4.3**, we have employed the rate equation model developed by Debuisschert et al. [30] to confirm the experimental results of an actively Q-switched intracavity OPO. Here the initial population of the passively Q-switched laser is employed in the same rate equation model to calculate the pulse energies of the fundamental laser and OPO signal outputs for passively Q-switched IOPOs with a shared-resonator configuration. In a passively Q-switched laser, the initial population inversion density in the gain medium, $n(0) = n_i$, can be determined from the condition that the roundtrip gain is exactly equal to the roundtrip losses just before the Q-switch opens, i.e.

$$n_i = \frac{\ln\left(\frac{1}{T_o^2}\right) + \ln\left(\frac{1}{R}\right) + L}{2\sigma l} \quad (1)$$

where T_o is the initial transmission of the saturable absorber, L is the round-trip fundamental wave intensity loss in the cavity, and R is the reflectivity of the output mirrors at the fundamental wavelength. Since SRO only resonates fundamental laser and signal fields, the evolution equation of the idler wave is eliminated. The rate equations for the four-level Q switched laser with IOPO are given by:

$$\frac{dn}{dt} = -c\sigma\phi_p n \quad (2)$$

$$\frac{d\phi_p}{dt} = \frac{l_{cr}}{l_{ca}} c\sigma n (\phi_p + \Delta\phi_p) - \frac{l_{nl}}{l_{ca}} \sigma_{opo} \phi_s \phi_p - \frac{\phi_p}{t_r} \left[\ln\left(\frac{1}{R}\right) + L \right] \quad (3)$$

$$\frac{d\phi_s}{dt} = \frac{l_{nl}}{l_{ca}} c \sigma_{opo} \phi_p (\phi_s + \Delta\phi_s) - \frac{\phi_s}{t_r} \left[\ln\left(\frac{1}{R_s}\right) + L_s \right], \quad (4)$$

where n is the inversion population density of the gain medium, σ is the stimulated emission cross section of the gain medium, c is the speed of light; ϕ_p is the fundamental laser photon density, ϕ_s is the OPO signal photon density, l_{ca} is the optical length of the laser cavity, l_{cr} is the length of the gain medium, l_{nl} is the length of the nonlinear crystal, σ_{opo} is the effective OPO conversion cross section, t_r is the round-trip time in the resonator cavity, $\Delta\phi_p$ is the spontaneous emission intensity, $\Delta\phi_s$ is the noise signal intensity, L_s is the round-trip signal wave intensity loss, and R_s is the output reflectivity at the signal wavelength. The effective OPO cross section, σ_{opo} , is used to describe the conversion rate and derived from the parametric gain coefficient for small gains of the single resonator oscillator:

$$2\sigma_{opo} l_{nl} = \frac{8\omega_i \omega_s d_{eff}^2 l_{nl}^2}{n_i n_s n_p \epsilon_0 c^2} \frac{A_p}{A_s + A_p}, \quad (5)$$

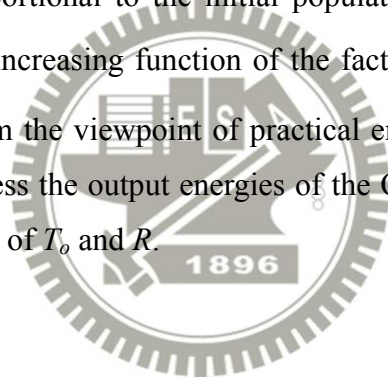
where ω_i and ω_s are the idler and signal frequencies, respectively; n_1 , n_2 and n_3 are the refractive indices at the idler, signal and fundamental laser wavelengths, respectively; d_{eff} is the effective nonlinear coefficient; ϵ_0 is the vacuum permittivity; A_s and A_p are the mode areas for the OPO signal and fundamental laser, respectively. The output pulse energy can be expressed as [33]

$$E_j = \frac{h\nu_j A_j}{2\sigma} \ln\left(\frac{1}{R}\right) \int \phi_j(t) dt, \quad (6)$$

where $h\nu$ is the photon energy, A is the beam area and ϕ is the above-mentioned photon density. The subscripts $j=s, p$ represents the OPO signal and fundamental laser, respectively.

Without loss of generality, we calculate the output pulse energies of the

dual-wavelength laser for a practical example of an intracavity OPO at 1572 nm with a type-II non-critically phase-matched x-cut KTP crystal pumped by a passively Q-switched Nd:YAG laser with a Cr⁴⁺:YAG crystal as a saturable absorber. With the properties of the Nd:YAG, KTP crystals and the typical cavity parameters: $h\nu_s=1.26\times 10^{-19}$ J, $h\nu_p=1.86\times 10^{-19}$ J, $\omega_i = 5.712\times 10^{14}$ sec⁻¹, $\omega_s = 1.198\times 10^{15}$ sec⁻¹, $l_{cr}=2.0$ cm, $l_{nl} = 2.0$ cm, $d_{eff} = 3.64$ pm/V, $n_i = 1.771$, $n_s = 1.737$, $n_p = 1.748$, $\varepsilon_0 = 8.854$ pF/m, $A_s = 0.108$ cm², $A_p = 0.16$ cm², $l_{ca} = 5.5$ cm, $R_s = 0.25$, $L = L_s = 0.01$, and $c = 3\times 10^8$ m/s, the calculated results for the output pulse energies with respect to R and T_o are depicted by the solid lines in **Fig. 4.4.1**. It can be seen that for a given T_o the OPO signal output energy increases with increasing the value of the reflectivity R , whereas the output energy of fundamental laser decreases with increasing the value of the reflectivity R . Physically, both the output energies of the OPO signal and fundamental laser are proportional to the initial population inversion density in the gain medium n_i that is an increasing function of the factor $\ln(1/T_o^2) + \ln(1/R) + L$, as shown in Eq. (1). From the viewpoint of practical engineering applications, it is of great usefulness to express the output energies of the OPO signal and fundamental laser as analytical functions of T_o and R .



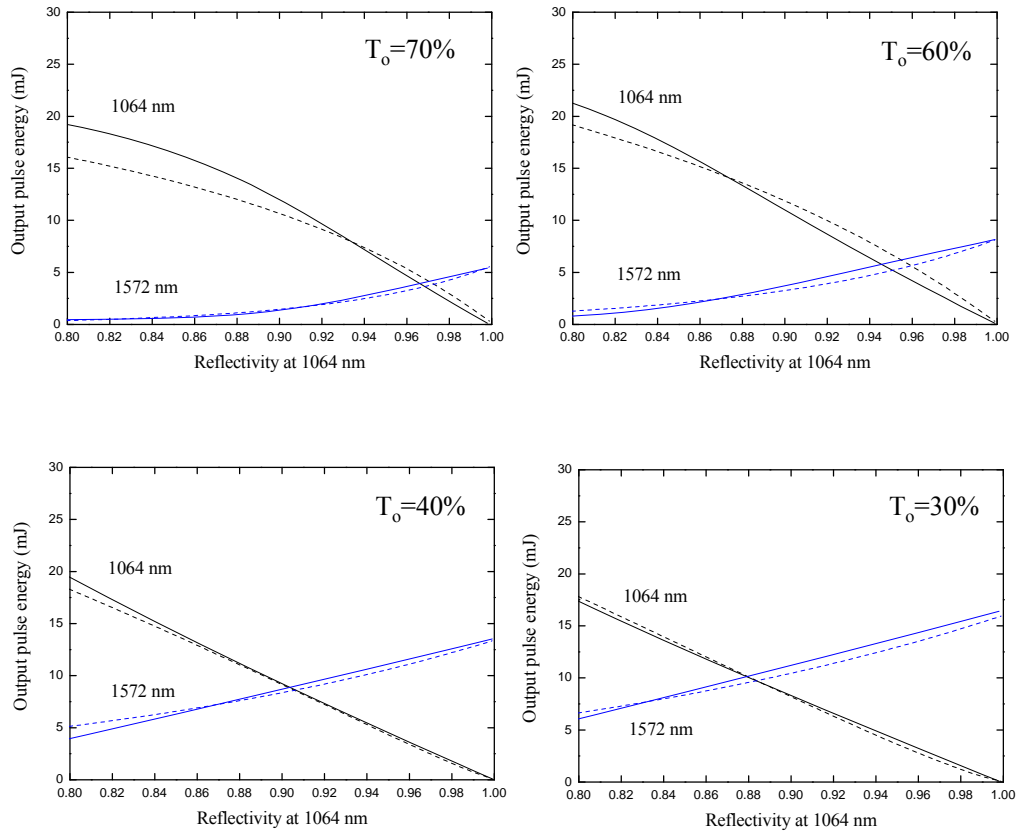


Fig. 4.4.1. Calculated results for the output pulse energy as a function of the reflectivity R for several values of T_o ; solid lines: theoretical results calculated from Eqs. (1)-(6); dashed lines: modeling results obtained with the analytical expressions of Eqs. (7)-(15).

4.4.2 Analytical Model

For the passively Q-switched laser, the output pulse energy has been numerically calculated as an analytical function of the parameters α , β , T_o , and $\ln(1/R)+L$ by Chen *et al.* [32], where $\alpha = \sigma_{gs} A / \gamma \sigma A_{sa}$, $\beta = \sigma_{es} / \sigma_{gs}$, A/A_{sa} is the ratio of the effective area in the gain medium and in the saturable absorber, σ_{gs} is the ground-state absorption cross-section of the saturable absorber, σ is the stimulated emission cross-section of the gain medium, γ is the inversion reduction factor ($\gamma=1$ and $\gamma=2$ correspond to, respectively, four-level and three-level systems; see Ref. [21]). Based on the model of Chen *et al.* [32] and using a nonlinear regression to fit the calculated results obtained with Eqs. (1)-(6), the output pulse energy at fundamental laser wavelength in the dual-wavelength operation can be analytically expressed as

$$E_f = E_p (1-R)^{q(T_o)} \quad (7)$$

with

$$q(T_o) = 0.73 - 1.84T_o + 1.14T_o^2 \quad (8)$$

where E_p is the pulse energy in the passive Q-switching operation and its expression in the model of Chen *et al.* [32] is given by

$$E_p = \frac{h\nu A}{2\sigma\gamma} \ln\left(\frac{1}{R}\right) \frac{(1-\beta) \ln\left(\frac{1}{T_o^2}\right)}{\beta \ln\left(\frac{1}{T_o^2}\right) + \ln\left(\frac{1}{R}\right) + L} \left[1 - \left(\frac{T_o}{(T_o)_{upper}}\right)^\eta \right] f(\alpha, \beta) \quad (9)$$

where

$$(T_o)_{upper} = \exp \left[-\frac{\ln(1/R) + L}{2(\alpha(1-\beta) - 1)} \right], \quad (10)$$

$$\eta = \frac{1}{\ln(1/R) + L} \left[\frac{1 + 3e^{-50\alpha^{-3}}}{\beta + 0.08} \right] (1 - e^{1-\alpha+\alpha\beta}), \quad (11)$$

$$f(\alpha, \beta) = 1.15 - 0.2e^{-5\beta} - 0.9\beta^2 - \frac{e^{1-\alpha}}{\sqrt{\alpha-1}} + \frac{(0.15 + 0.9\beta)}{e^{150\alpha^{-3}}}. \quad (12)$$

On the other hand, the output pulse energy at signal wavelength in the dual-wavelength operation can be fitted to be given by

$$E_s = E_p B(R, T_o) R^{p(T_o)} \quad (13)$$

with

$$B(R, T_o) = \frac{1}{\ln(1/R)} (0.25 e^{-0.96T_o} - 0.091) \quad (14)$$

and

$$p(T_o) = 9 - 35T_o + 50T_o^2 \quad (15)$$

To reveal the accuracy of the analytical function, we use the analytical model in Eqs. (7)-(15) to calculate the output pulse energies for the case given in **Fig. 4.4.1**. The

calculated results based on Eqs. (7)-(15) are shown by the dashed lines in **Fig. 4.4.1**. The results obtained with the analytical model can be found to agree very well with the numerical calculation for all cases. As a consequence, a straightforward model is successfully developed for the design of passively Q-switched dual-wavelength 1.06 μm /1.57 μm lasers.



4.4.3 Experimental Results and Discussion

To demonstrate the utilization of the analytical model, a dual-wavelength 1064 nm/1572 nm laser based on an IOPO pumped by a passively Q-switched Nd:YAG laser in a shared resonator was performed, as shown in **Fig. 4.4.2**. The structure of the shared resonator is that the OPO cavity completely overlaps with the fundamental laser cavity. The pump source was a quasi-cw high-power diode stack (Coherent G-stack package, Santa Clara, Calif., USA) which consisted of six 10-mm-long diode bars with a maximum output power of 120 W per bar at the central wavelength of 808 nm. The diode stack was constructed with 400 μm spacing between the diode bars so the whole emission area was approximately 10 mm (slow axis) \times 2.4 mm (fast axis). The full divergence angles in the fast and slow axes are approximately 35° and 10°, respectively. In the experiment, the diode stack was driven to emit optical pulse durations of 300 μs at a repetition rate less than 30 Hz with a maximum duty cycle of 1%. The pump radiation was delivered into the gain medium with a lens duct that was possessed of the advantages of simple fabrication, high coupling efficiency, and insensitivity to slight misalignment. In our experiment, the lens duct was manufactured with the parameters of $r = 10$ mm, $L = 29$ mm, $H_1 = 12$ mm, $H_2 = 3.5$ mm, and $H_3 = 3.5$ mm. The coupling efficiency of the lens duct was experimentally measured to be approximately 85%.

The gain medium was a 1.0 at. % Nd:YAG crystal with a diameter of 6 mm and a length of 20 mm. The entrance surface of the laser crystal was coated with high reflection at 1064 nm and 1573 nm ($R > 99.8\%$) and high transmission at 808 nm ($T > 90\%$). The other surface of the laser crystal was coated with antireflection at 1064 nm and 1573 nm ($R < 0.2\%$). The saturable absorber for the passively Q-switching was a Cr^{4+} :YAG crystal with a thickness of 2 mm and an initial transmission of 50% at 1064 nm. The nonlinear crystal for the OPO was a KTP crystal with a cross section of 4 mm \times 4 mm and a length of 20 mm. The KTP crystal was x -cut ($\theta = 90^\circ$, and $\phi = 0^\circ$) for type II noncritical phase-matching to eliminate walk-off effect between the fundamental, signal, and idler beams. The polarization of fundamental laser has a preferred linear polarization along the y axis of

KTP crystal which is the ordinary wave. The OPO signal is also polarized parallel to the y axis, whereas the idler is polarized along the z axis. Intracavity pumped by the 1.064 μm radiation, the OPO produces a signal wavelength at 1.57 μm , and the idler wavelength is 3.3 μm . Because of the strong absorption of the idler wave (3–4 μm) in the KTP crystal and in the BK7 glass mirror, the OPO is resonant on the signal frequency only. In general, the reflectivity of the output coupler made from BK7 glass for idler wave is less than 10%. No idler wave was extracted from the cavity and detected. Both surfaces of the KTP and Cr^{4+} :YAG crystals were coated for anti-reflection at 1064 and 1572 nm. All crystals were wrapped with indium foil and mounted in conductively cooled copper blocks. To investigate the dual-wavelength operation, we used several flat output couplers with the reflectivity of 99.8%, 98%, 94%, and 90% at 1064 nm, and the respective corresponding reflectivity at 1572 nm are 10%, 26%, 10%, and 24%. Note that the optimal output reflectivity at the signal wavelength for the IOPO has been verified to be approximately 10-30% in **Section 4.3**. The optical resonator was a plane-parallel cavity. The total cavity length was approximately 55 mm. The dielectric mirror coated with high transmission at 1064 nm ($T > 95\%$) and high reflection at 1573 nm ($R > 99.5\%$) was used to separate the fundamental laser and OPO signal. Two Filters, F1 and F2, were utilized in the experimental measurement. A LeCroy digital oscilloscope (Wavepro 7100; 10 G samples/sec; 1 GHz bandwidth) with the fast InGaAs photodiodes was used to record the pulse temporal behavior at 1064 nm and 1572 nm. The spectral information was monitored by an optical spectrum analyzer (Advantest Q8381A) that employs a diffraction grating monochromator to for measure high-speed light pulses with the resolution of 0.1 nm.

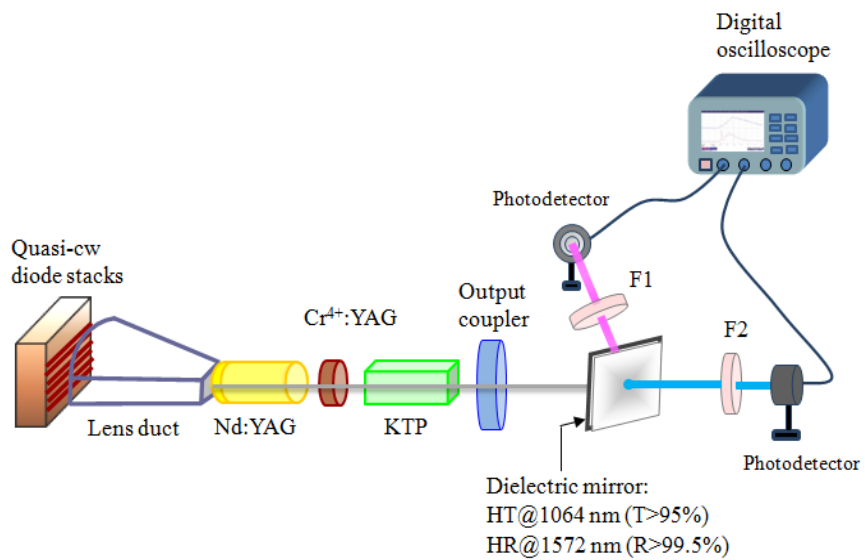


Fig. 4.4.2. Experimental setup for an intracavity OPO pumped by a diode-pumped passively Q-switched Nd:YAG / Cr⁴⁺:YAG laser in a shared resonator.

Experimental results revealed that the pump threshold energies were 170, 175, 182, and 188 mJ for the reflectivity of 99.8%, 98%, 94%, and 90% at 1064 nm, respectively. The pump threshold energy can be found to increase linearly with decreasing the output reflectivity. It was also found that the laser threshold for the reflectivity of 80% was greater than the maximum pump energy that was approximately 195 mJ from the diode stack through the lens duct. The dependence of the pump threshold energy on the reflectivity can be calculated with [34]

$$E_{th} = \frac{Ah\nu_p}{\eta_p 2\sigma} \left[\ln\left(\frac{1}{T_o^2}\right) + \ln\left(\frac{1}{R}\right) + L \right], \quad (16)$$

where η_p is the pump efficiency including the overlapping efficiency and the absorption efficiency, and $h\nu_p$ is the pump photon energy. With the properties of the Nd:YAG and Cr⁴⁺:YAG crystals and the typical cavity parameters: $\sigma = 2.8 \times 10^{-19} \text{ cm}^2$, $h\nu_p = 2.46 \times 10^{-19} \text{ J}$, $\eta_p = 0.54$, $A = 0.16 \text{ cm}^2$, $R = 99.8\%$, $T_o = 0.5$, and $L = 0.01$, the theoretical threshold energies were calculated to compare with the experimental results, as shown in **Fig. 4.4.3**. It can be seen that the experimental results agree very well with the theoretical values. Note that the pump threshold energy with respect to the reflectivity at the fundamental laser wavelength in different T_o cases can be theoretically calculated with Eq. (16).

Figure 4.4.4 shows the calculated and experimental results for the output pulse energy with respect to the reflectivity at the fundamental wavelength of 1064 nm. The calculated results obtained from theoretical Eqs. (1)-(6) and from the analytical expressions of Eqs. (7)-(15), respectively, are also shown in **Fig. 4.4.4** for comparison. It can be seen that the analytical model is in good agreement with the experimental data and the theoretical calculation. Lowering the reflectivity at 1064 nm can be found to lead to an increase in the output pulse energy at 1064 nm and a relative decrease in the signal output pulse energy. With the reflectivity of 99.8%, 98%, 94%, and 90%, the output pulse energies at 1064 nm were 0.1, 1.9, 5.3, and 8.9 mJ, respectively and the corresponding pulse energies at 1572 nm were 10.8, 9.1, 7.7, and 6.6 mJ, respectively. As a result, the total pulse energy of fundamental and

signal outputs increased from 10.9 mJ up to 15.5 mJ for the reflectivity decreasing from 99.8% to 90%. Divided by the pump threshold energy, the overall conversion efficiency was enhanced from 6.4% to 8.2% for the reflectivity decreasing from 99.8% to 90%. In other words, the dual-wavelength output efficiency for the signal and fundamental waves was considerably greater than the output efficiency for only the OPO signal wave.

Typically temporal shapes for the depleted fundamental laser and OPO signal pulses were simultaneously detected for the reflectivity of 99.8%, 98%, 94% at 1064 nm, and 90%, as shown in **Figures 4.4.5 (a)-(d)**. It can be seen that the pulse width of the fundamental laser output conspicuously decreases with decreasing with the reflectivity at the fundamental laser wavelength. On the other hand, the pulse shape of the OPO signal output generally displayed a sharp peak accompanied by a much longer long tail. Experimental results revealed that the long tail mainly determined the magnitude of the OPO signal pulse energy, whereas the sharp peak had a dominant influence on the peak power. **Figure 4.4.6** shows the output peak powers for the fundamental laser and OPO signal with respect to the reflectivity at 1064 nm. The peak powers were precisely deduced by the numerical integration for the measured temporal pulse profiles to fit the experimental pulse energies. It can be seen that the peak power at 1064 nm is enhanced up to 0.3 MW by lowering the reflectivity at 1064 nm. In contrast, the peak power at 1572 nm could be maintained in the range of 0.62 to 0.82 MW on account of the sharp peak. In general, the central part of the fundamental laser beam converts to the OPO signal beam only, which acts as a naturally spatial filter. Higher order transverse modes were not observed in this experiment.

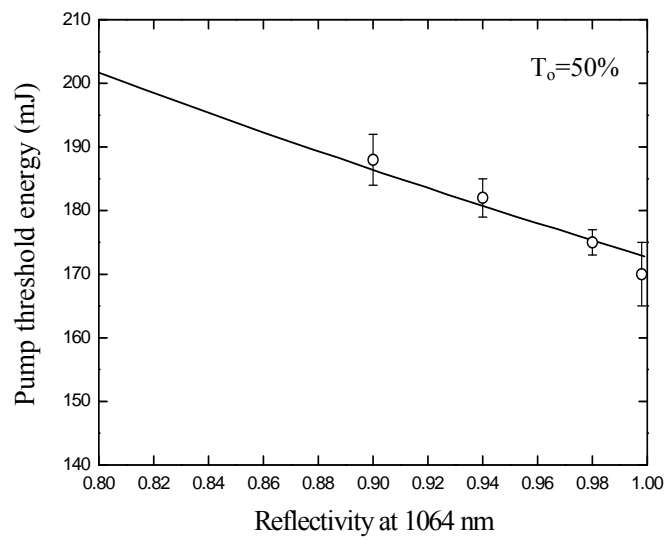


Fig. 4.4.3. The pump threshold energy with respect to the reflectivity at the fundamental laser wavelength of 1064 nm in $T_o=50\%$ case; solid lines: theoretical results; symbols: experimental values.

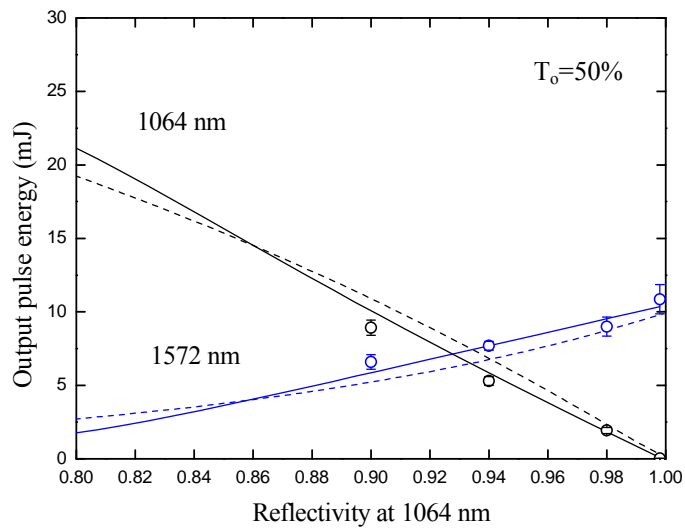


Fig. 4.4.4. Calculated and experimental results for the output pulse energy with respect to the reflectivity at the fundamental laser wavelength of 1064 nm in $T_o=50\%$ case; solid lines: theoretical results calculated from Eqs. (1)-(6); dashed lines: modeling results obtained with the analytical expressions of Eqs. (7)-(15); symbols: experimental results.

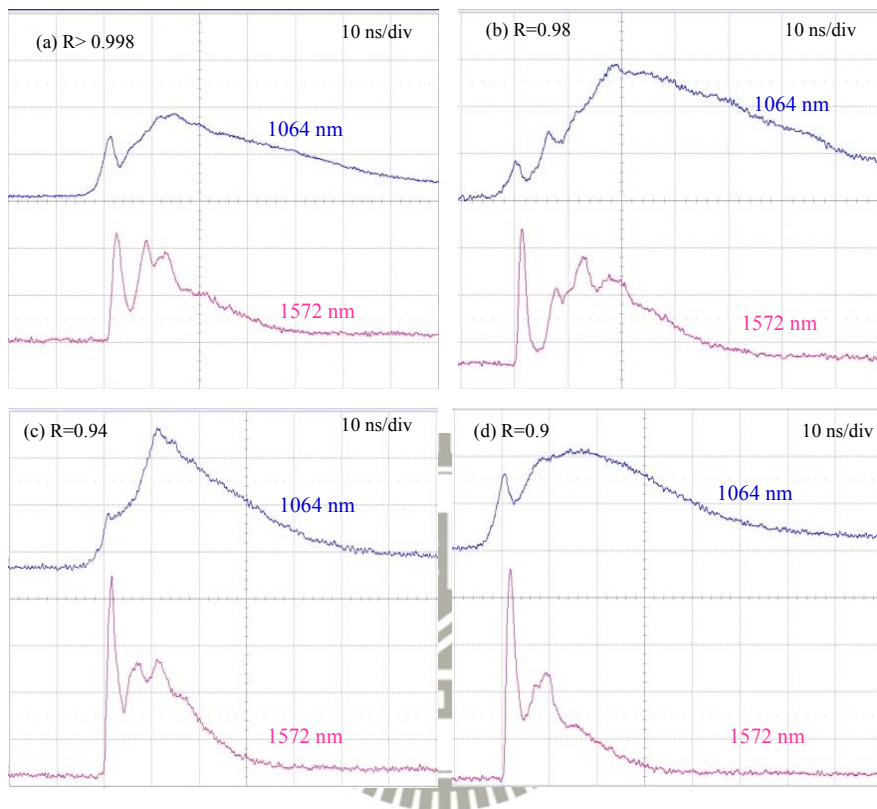


Fig. 4.4.5. Experimentally temporal shapes of the fundamental laser (1064 nm) and OPO signal (1572 nm) pulses generated in $T_o = 50\%$ case for the reflectivity of (a) 0.998, (b) 0.98, (c) 0.94, and (d) 0.9.

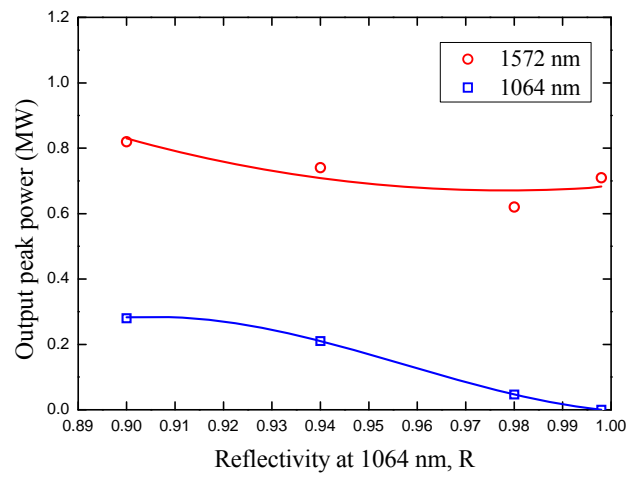


Fig. 4.4.6. The output peak power as a function of the reflectivity at the fundamental laser wavelength of 1064 nm in $T_o=50\%$ case.

4.5 Efficient Intracavity OPO with an AlGaInAs

Quantum-Well (QW) Saturable Absorber

Owing to the excellent optical properties of large stimulated emission cross-section, large absorption coefficient, wider absorption bandwidth, and short fluorescence lifetime, Nd:YVO₄ laser crystal is a candidate to generate an efficient Q-switched laser with high pulse repetition rates as well as short pulse. Cr⁴⁺:YAG crystal is the popular saturable absorber for Nd-doped lasers in the spectral region of 1.0–1.1 μm [35-42]. However, the passively Q-switched Nd:YVO₄ laser with a Cr⁴⁺:YAG saturable absorber is not effectively realized, because the absorption cross-section of the Cr⁴⁺:YAG crystal (in the order of 10⁻¹⁹ cm² [43]) is not large enough for the good Q-switching [32].

One solution for good passively Q-switching is to provide the proper spot size on the Cr⁴⁺:YAG saturable absorber through special cavity design [40-42]. Alternatively, semiconductor saturable absorber mirrors (SESAMs) have been demonstrated as useful devices for solid-state lasers [44-47]. Compared with Cr⁴⁺:YAG crystals, the saturation fluence and maximum modulation depths of SESAMs can be flexibly designed, and they can be adapted to different laser wavelengths. Additionally, the SESAM has large absorber cross section (in the range of 10⁻¹⁴ to 10⁻¹⁵ cm² [48]), and therefore is more suited for Nd:YVO₄ lasers. InGaAs/GaAs quantum wells (QWs) have been used as SESAMs for above 1.0-μm solid-state lasers. However, the modulation depth is restricted to the lattice mismatch resulting in large insertion loss. The quaternary alloy of AlGaInAs can be grown epitaxially on a transparent InP substrate without lattice mismatch and offer a superior electron confinement in the 0.84-1.65 μm spectral range [49-51].

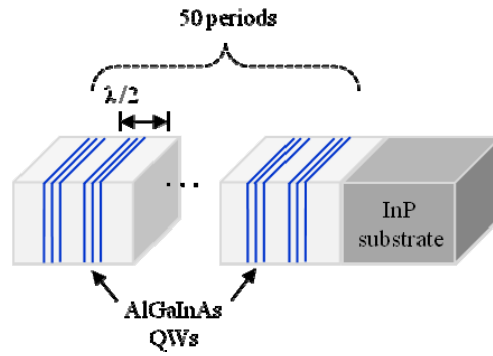
In this section, we demonstrate a mJ passively Q-switched Nd:YVO₄ laser with an AlGaInAs/InP QWs saturable absorber under quasi-continuous-wave (QCW) diode pumping. Furthermore, we use a coupled resonator configuration to construct a compact intracavity OPO, consisting of a convex lens.

4.5.1 AlGaInAs QWs Saturable Absorber

The AlGaInAs QW saturable absorber consisted of 50 groups of three QWs, spaced at half-wavelength intervals by InAlAs barrier layers with a bandgap wavelength around 805 nm, as depicted in **Fig. 4.5.1 (a)**. The luminescence wavelength of the saturable absorber was designed to be near 1066 nm. An InP window layer was deposited on the QW/barrier structure to avoid surface recombination and oxidation. The backside of the substrate was mechanically polished after growth. Each side of the semiconductor saturable absorber was anti-reflection coated to reduce back reflections and the couple-cavity effects.

Figure 4.5.1 (b) shows the measured result for the low-intensity transmittance spectrum of the QW saturable absorber. The initial transmission of the absorber at the wavelength of 1066 nm was found to be approximately 26%. The operation bandwidth of the absorber is approximately 8 nm. The saturation transmission of the AlGaInAs saturable absorber was measured with a nanosecond Nd:YAG Q-switched laser as the pump source, as shown in **Fig. 4.5.2**. The transmission of Cr⁴⁺:YAG crystal was displayed for comparison. The Cr⁴⁺:YAG crystal was highly doped with a small signal transmission of 28% and was coated for antireflection at 1064 nm ($R < 0.2\%$) on each side. The 95% final transmission of AlGaInAs QWs indicated the low nonsaturable loss induced by the facet reflection and absorption by the substrate. The Cr⁴⁺:YAG crystal with a small final transmission of 85% was attributed to the excited-state absorption (ESA) [52]. The modulation depths (Δ) of AlGaInAs QWs and Cr⁴⁺:YAG crystal were 68% and 57%, respectively. The pulse energy fluence of AlGaInAs QWs was two orders of magnitude smaller than that of Cr⁴⁺:YAG crystal. It reveals that a much larger absorption cross section of AlGaInAs QWs than that of Cr⁴⁺:YAG crystal. Furthermore, the relaxation time of the AlGaInAs QWs the Cr⁴⁺:YAG crystal were estimated to be on the order of 100 ns and 3 μ s, respectively. Consequently, AlGaInAs QWs is an attractive choice as a passive Q-switch for Nd:YVO₄ lasers.

(a)



(b)

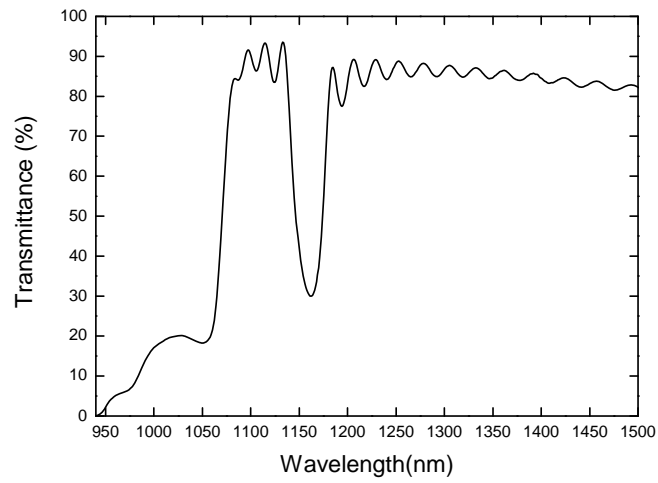


Fig. 4.5.1. (a) Structure of the present AlGaInAs material; (b) transmittance spectrum at room temperature for the AR-coated AlGaInAs/InP saturable absorber.

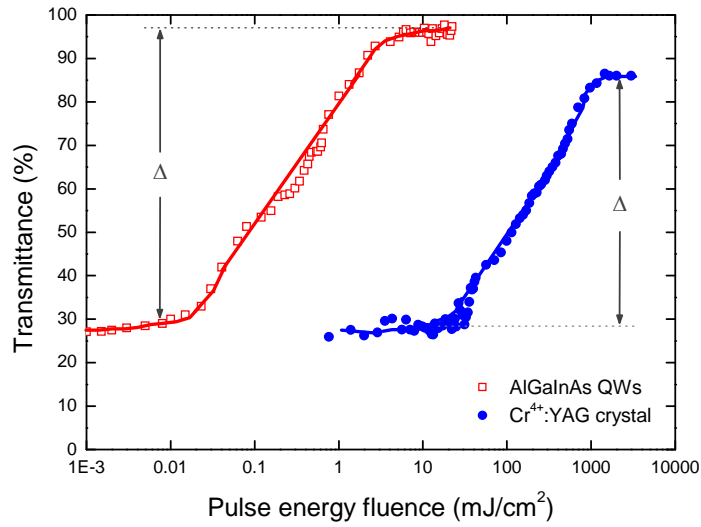


Fig. 4.5.2. Transmittance of AlGaInAs material and Cr⁴⁺:YAG crystal as a function of the incident pulse energy fluence.

4.5.2 Cavity Design and Setup

The pump source was a QCW high-power diode stack (Coherent G-stack package, Santa Clara, Calif., USA) which consisted of six 10-mm-long diode bars with a maximum output power of 120 W per bar at the central wavelength of 808 nm. The diode stack was constructed with 400 μm spacing between the diode bars so the whole emission area was approximately 10 mm (slow axis) \times 2.4 mm (fast axis). The full divergence angles in the fast and slow axes are approximately 35° and 10° , respectively. A lens duct was utilized to efficiently couple the pump radiation from the diode stack into the laser crystal. In this experiment, a lens duct was manufactured with $r = 10$ mm, $L = 29$ mm, $H_1 = 12$ mm, $H_2 = 3.8$ mm, and $H_3 = 3.8$ mm. Note that a lens duct with a large output dimension of $H_2 \times H_3$ was used to enhance the laser mode volume in this plane-parallel cavity. The coupling efficiency of the lens duct was experimentally measured to be approximately 80%.

Figure 4.5.3 depicts the experimental configuration of a QCW diode-pumped passively Q-switched Nd:YVO₄ laser with AlGaInAs QWs as a saturable absorber. The active medium was an a-cut 0.5 at.% Nd³⁺, 7-mm long Nd:YVO₄ crystal. The entrance surface of the laser crystal was coated with highly reflective at 1064 and 1573 nm ($R > 99.8\%$) and highly transmittance at the pump wavelength of 808 nm ($T > 90\%$). The other side of the laser crystal was coated to be antireflective at 1064 and 1573 nm ($R < 0.2\%$). The laser crystal was wrapped with indium foil and mounted in a copper block. The reflectivity of the flat output coupler is 50% at 1064 nm. In this experiments, the pump duration of QCW laser diode stack was 100 μs to match the upper-level lifetime of Nd:YVO₄ laser crystal.

On the other hand, we design a linear three-element cavity to achieve a high conversion efficiency intracavity OPO by an internal convex lens. The three-element cavity is shown in **Fig. 4.5.4 (a)**, where L_1 is the distance between the front mirror and the convex lens, L_2 is the distance between the convex lens and the output coupler, and f is the focal length of the convex lens. Due to the nonlinear crystal phase-match acceptance angle, tight focusing limits the nonlinear conversion efficiency. The focal length of the convex lens was chosen to be 10 cm. With a pump area of $3.8 \times 3.8 \text{ mm}^2$,

the mode size on the KTP crystal is aimed to be $1.9 \times 1.9 \text{ mm}^2$ to achieve a high conversion efficiency intracavity OPO. Thus, the appropriate values of L_1 and L_2 can be found to approximately 351 mm and 124 mm, respectively. **Fig. 4.5.4 (b)** shows the experimental setup of the intracavity OPO pumped by a passively Q -switched Nd:YVO₄ laser in a coupled cavity configuration. The OPO cavity was formed by two flat mirrors. The first mirror had a dichroic coating with highly reflective at 1573 nm ($R > 99.8\%$) and highly transmittance at 1064 nm ($T > 95\%$). The output coupler had a dichroic coating that was highly reflective at 1064 nm ($R > 99.8\%$) and partially reflective at 1573 nm. Several output couplers with different reflectivities ($34\% \leq R_s \leq 90\%$) at 1573 nm were used in the experiment to study the output optimization. A KTP crystal was used to be the nonlinear crystal of the OPO. The KTP crystal, $5 \times 5 \times 30 \text{ mm}^3$, was employed in a type II noncritical phase-matching configuration along the x axis ($\theta = 90^\circ$, and $\varphi = 0^\circ$) to have both a maximum effective nonlinear coefficient and no walk off between the pump, signal, and idler beams. The longer of KTP crystal is used to increase the interaction length to achieve higher conversion efficiency.

The overall Nd :YVO₄ laser cavity length was approximately 1.5 cm and the intracavity OPO cavity length was about 47.5 cm. A LeCroy digital oscilloscope (Wavepro 7100; 10 G samples/sec; 1 GHz bandwidth) with the fast InGaAs photodiodes was used to record the pulse temporal behavior at 1064 nm and 1572 nm. The spectral information was monitored by an optical spectrum analyzer (Advantest Q8381A) that employs a diffraction grating monochromator to for measure high-speed light pulses with the resolution of 0.1 nm.

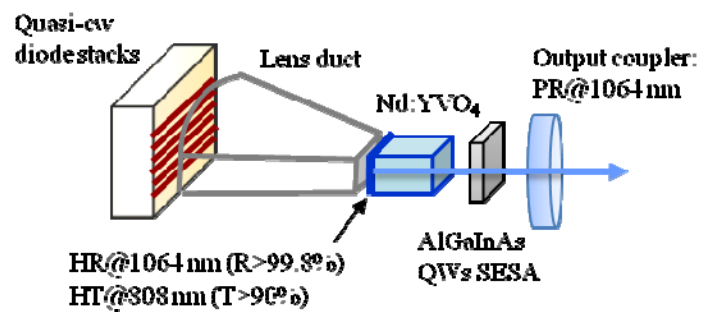
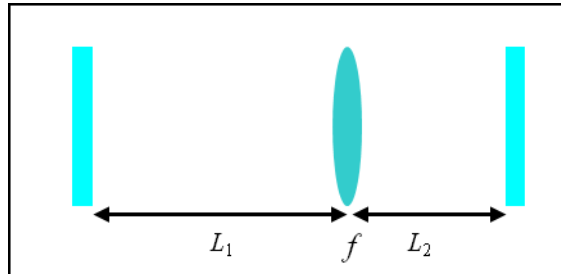


Fig. 4.5.3. Experimental schematic of the passively Q-switched Nd:YVO₄ laser with AlGaInAs QWs as a saturable absorber.

(a)



(b)

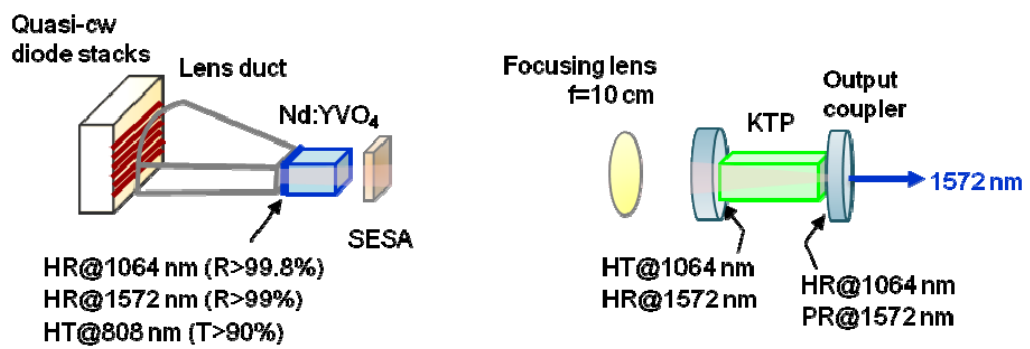


Fig. 4.5.4. Schematic diagrams of (a) a linear three-element cavity, (b) an intracavity OPO with AlGaInAs QWs as a saturable absorber in a coupled-cavity configuration.

4.5.3 Results and Discussion

First of all, the quasi-cw free-running operation without saturable absorber was performed to confirm the pumping efficiency of the lens duct and the quality of the laser crystal. A flat output coupler with 90% reflectivity at 1064 nm was utilized to substitute the above-mentioned PQS output coupler. **Figure 4.5.5** shows the experimental results of the output pulse energy with respect to the pump energy in the free-running operation. At 59 mJ of pump energy, the output energy at 1064 nm is found to be approximately 33 mJ.

We estimated the performance of the passively Q-switched Nd:YVO₄ laser with the AlGaInAs QWs before the intracavity OPO experiment. The optimum Q-switched performance at 1064 nm provides the baseline for evaluating the conversion efficiency of the intracavity OPO. The optimum reflectivity of the output coupler was found to be approximately 50%. The threshold of the Q-switched laser operation was found to be approximately 34 mJ. A output pulse energy of 3.5 mJ was generated with an optical-to-optical efficiency of 10.3% with respect to incident pump energy. In order to accurately investigate the stability of the Q-switched Nd:YVO₄ laser with the AlGaInAs QWs, the 1064-nm output pulse energy was recorded at a repetition rate of 200 Hz, depicted in **Figure 4.5.6 (a)**. It can be found that the fluctuation of the output pulse energy was smaller than 2%. **Figure 4.5.6 (b)** shows the temporal shape of the laser pulse. The pulse width was less than 5 ns. By the numerical integration for the measured temporal pulse profile to fit the experimental pulse energy, the peak power was deduced to be about 1.03 MW. The excellent performances reveal that the AlGaInAs QW with a low nonsaturable loss and a large modulation depth is a promising material for an efficient Q-switched operation. To our best our knowledge, these are the largest pulse energy and the highest peak power obtained in diode-pumped Nd:YVO₄ lasers at 1.06 μm [38-42,53].

With a convex lens and an OPO output coupler, the intracavity OPO experiment was performed. The threshold of the intracavity OPO was found to be nearly the same as that of the passively Q-switched laser. **Figure 4.5.7** shows the output pulse

energy at 1573 nm as a function of the OPO output reflectivity. It can be seen that the optimum output coupler for the maximum OPO pulse energy is found to be approximately $R_s = 80\%$. With the optimum output coupler of $R_s = 80\%$, the OPO pulse energy was measured to be 1.53 mJ. The effective conversion efficiency with respect to the optimized pulse energy from the passively Q-switched laser is up to 44%. With the optimum output coupler of $R_s=80\%$, the stability of the Nd:YVO₄ intracavity OPO was also recorded. At a repetition rate greater than 50 Hz, the OPO output pulse energy dropped rapidly due to the damage of an AlGaInAs material. The possible reason is ascribed to the severer thermal lensing at a higher repetition rate, resulting in smaller spot size on the AlGaInAs material, and the intense 1064-nm energy within the OPO cavity. Therefore, compared with the stability of 1064-nm PQS performance at 200 Hz, the OPO output pulse energy was maintained at a lower repetition rate of 50 Hz. The OPO output pulse energy was recorded at a repetition rate of 50 Hz, as shown in **Figure 4.5.8**. It can be found that the fluctuation of the OPO output pulse energy was smaller than 4%. With actively cooling system for laser diode stack, active medium, and the AlGaInAs saturable absorber, the stability of the output pulse energy will be improved.

Typical oscilloscope trace of a train of the laser and OPO pulses with $R_s=80\%$ is shown in **Fig. 4.5.9 (a)**. The pulse-to-pulse amplitude was within $\pm 10\%$. **Fig. 4.5.9 (b)** shows the temporal shapes of 1064 nm and 1573 nm pulses with $R_s=80\%$. By the numerical integration, the OPO peak power was calculated and found to be approximately 60 kW. For the first time to our knowledge, a passively Q-switched Nd:YVO₄ intracavity OPO with semiconductor saturable absorber is achieved.

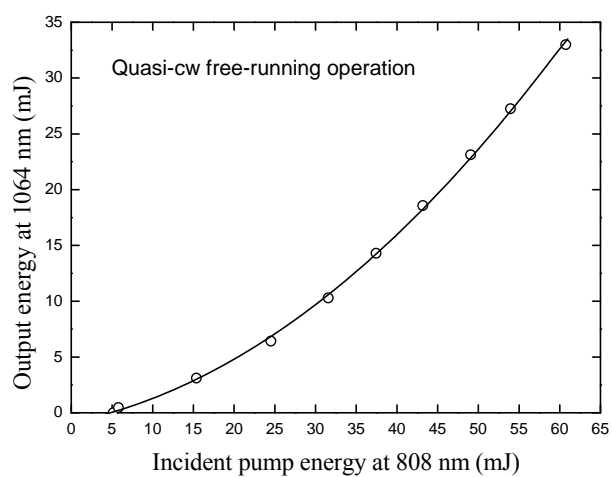
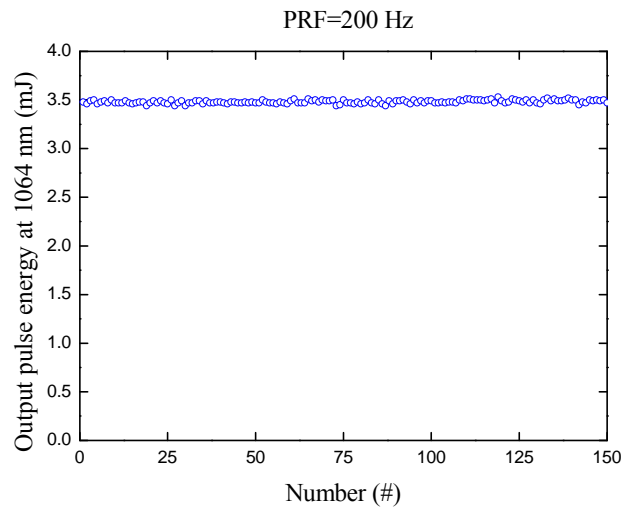


Fig. 4.5.5. Output energy at 1064 nm with respect to the incident pump energy at 808 nm for QCW free-running operation.

(a)



(b)

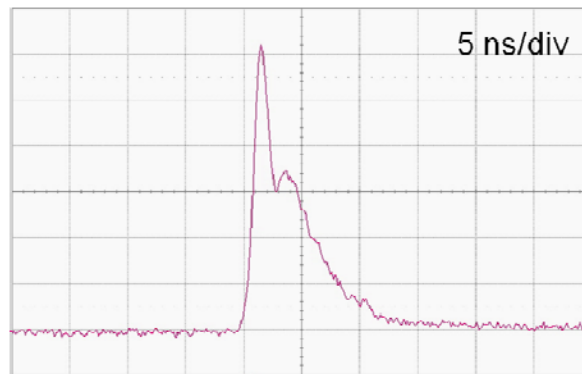


Fig. 4.5.6. (a) Energy stability of the passively Q-switched Nd:YVO₄ laser under a repetition rate of 200 Hz and (b) temporal shape for the passively Q-switched Nd:YVO₄ laser with an AlGaInAs QW saturable absorber.

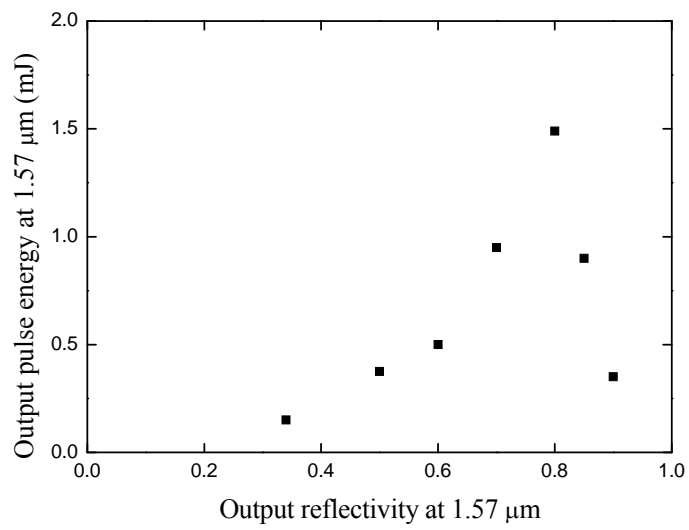


Fig. 4.5.7. Experimental results for the output pulse energy at 1573 nm versus the OPO output reflectivity.

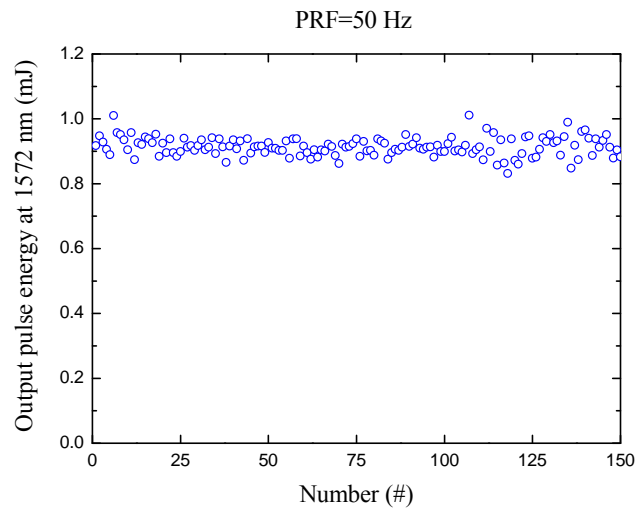


Fig. 4.5.8. Energy stability of the Nd:YVO₄ OPO with an AlGaInAs QW saturable absorber at a repetition rate of 50 Hz with the optimum output coupler of $R_s = 80\%$.

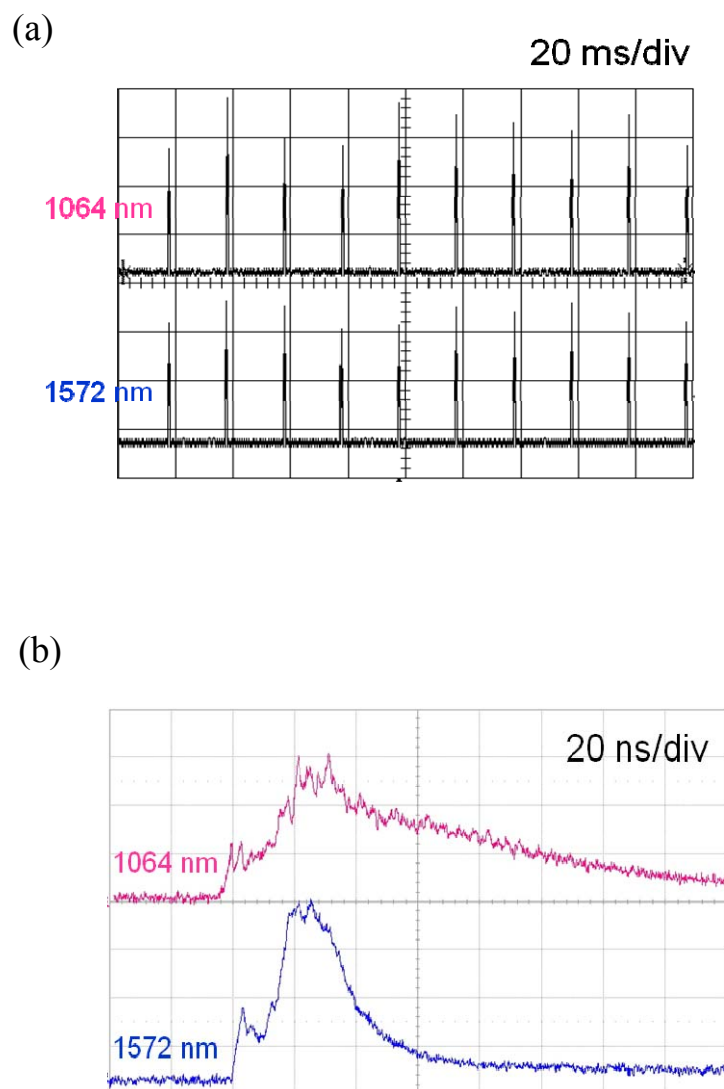


Fig. 4.5.9. (a) Typical oscilloscope trace of a train of the laser and OPO pulses with $R_s = 80\%$; (b) temporal shapes of the laser and OPO pulses with $R_s = 80\%$.

4.6 Conclusions

First, we have theoretically and experimentally explored the output performance of an intracavity OPO in a shared cavity configuration. The threshold of an intracavity OPO pumped by a passively Q-switched Nd:YAG laser has been verified to be utterly controlled by the bleach of the saturable absorber not by the signal output reflectivity. Based on thorough experimental studies, we found that an efficient subnanosecond eye-safe laser with 3.3 mJ pulse energy and 1.5 MW peak power could be achieved with a signal output reflectivity of 15% at a diode pump energy of 65 mJ.

Moreover, the use of output mirrors with partial reflection at fundamental laser instead of a highly reflective mirror is not only to generate a dual-wavelength (fundamental laser/ OPO signal) laser but also to reduce the risk of optical damage. An analytical model for designing the simultaneous emission of fundamental laser and OPO signal with a passively Q-switched IOPO has been developed. An efficient dual-wavelength 1.06 μm /1.57 μm laser in a compact IOPO with a type-II non-critically phase-matched x-cut KTP crystal pumped by a passively Q-switched Nd:YAG laser was performed and systematically investigated to demonstrate the utilization of the present model. With the reflectivity of 99.8%, 98%, 94%, and 90%, the output pulse energies at 1064 nm are found to be 0.1, 1.9, 5.3, and 8.9 mJ, respectively; the corresponding pulse energies at 1572 nm are 10.8, 9.1, 7.7, and 6.6 mJ, respectively. Experimental results show that the output energies of the dual-wavelength laser agree very well with the results obtained with the analytic model.

An AlGaInAs material with a periodic QW/barrier structure grown on a Fe-doped InP structure has developed to be a saturable absorber in a QCW diode-pumped Nd:YVO₄ intracavity OPO. At first, the excellent PQS performances reveal that the AlGaInAs QW material with a low nonsaturable loss and a large modulation depth. Stable Q-switched pulse energy of 3.5 mJ at a repetition rate of 200 Hz, with a peak power greater than 1 MW, was generated at a pump energy of 34 mJ. To our best our knowledge, these are the largest pulse energy and the highest peak power obtained in

diode-pumped Nd:YVO₄ lasers at 1.06 μm. A convex lens was used in the intracavity OPO cavity. The threshold of the intracavity OPO was found to be nearly the same as that of the passively Q-switched laser. With the optimum output coupler of R_s = 80%, the OPO pulse energy was measured to be 1.53 mJ with a peak power of 60 kW. The effective conversion efficiency with respect to the optimized pulse energy from the passively Q-switched laser is up to 44%. To our knowledge, a passively Q-switched Nd:YVO₄ intracavity OPO with semiconductor saturable absorber is achieved for the first time.



References

- [1] W. Koechner, Solid-State Laser Engineering, vol. 1, Optical Sciences, 6th ed., (Springer, Berlin, 2006).
- [2] E.O. Ammann, "High-average-power Raman oscillator employing a shared-resonator configuration," Appl. Phys. Lett. **32**, 53-54 (1978).
- [3] Y. F. Chen and L. Y. Tsai, "Comparison between shared and coupled resonators for passively Q-switched Nd:GdVO₄ intracavity optical parametric oscillators," Appl. Phys. B **82**, 403-406 (2006).
- [4] E.O. Amman, J.M. Yarborough, M.K. Oshman, P.C.Montgomery, "Efficient internal optical parametric oscillation," Appl.Phys. Lett. **16**, 309-312 (1970).
- [5] M.K. Oshman, S.E. Harris, "Theory of optical parametric oscillation internal to the laser cavity," IEEE J. Quantum Electron. **4**, 491-502 (1968).
- [6] J. Falk, J.M. Yarborough, E.O. Amman, "Internal optical parametric oscillation," IEEE J. Quantum Electron. **7**, 359-369 (1971).
- [7] L.R. Marshall, A. Kaz, "Eye-safe output from noncritically phase-matched parametric oscillators," J. Opt. Soc. Am. B **10**, 1730-1736 (1993).
- [8] G. Xiao, M. Bass, M. Acharekar, "Passively Q-switched solid-state lasers with intracavity optical parametric oscillators," IEEE J. Quantum Electron. **34**, 2241-2245 (1998).
- [9] R. Dabu, C. Fenic, A. Stratan, "Intracavity pumped nanosecond optical parametric oscillator emitting in the eye-safe range," Appl. Opt. **40**, 4334-4340 (2001).
- [10] Z. Liu, Q. Wang, X. Zhang, Z. Liu, J. Chang, H. Wang, S. Fan, W. Sun, G. Jin, X. Tao, S. Zhang, and H. Zhang, "Efficient acoustic-optically Q-switched

- intracavity Nd:YAG/ KTiOAsO₄ parametric oscillator,” Appl. Phys. B **92**, 37-41 (2008).
- [11] H. T. Huang, J. L. He, X. L. Dong, C. H. Zuo, B. T. Zhang, G. Qiu, and Z. K. Liu, “High-repetition-rate eye-safe intracavity KTA OPO driven by a diode-end-pumped Q-switched Nd:YVO₄ laser,” Appl. Phys. B **90**, 43-45 (2008).
- [12] Y. F. Chen, S. W. Chen, S. W. Tsai, and Y. P. Lan, “High repetition-rate eye-safe optical parametric oscillator intracavity pumped by a diode-pumped Q-switched Nd:YVO₄ laser,” Appl. Phys. B **76**, 263–266 (2003).
- [13] J. Miao, J. Peng, B. Wang, H. Tan, and H. Bian, “Compact low threshold Cr:YAG passively Q-switched intracavity optical parametric oscillator,” Opt. Commun. **281**, 2265–2270 (2008).
- [14] Y. F. Chen, S. W. Chen, Y. C. Chen, Y. P. Lan, and S. W. Tsai, “Compact efficient intracavity optical parametric oscillator with a passively Q-switched Nd:YVO₄/Cr⁴⁺:YAG laser in a hemispherical cavity,” Appl. Phys. B **77**, 493-495 (2003).
- [15] Y. F. Chen, S. W. Chen, L. Y. Tsai, Y. C. Chen, and C. H. Chien, “Efficient subnanosecond intracavity optical parametric oscillator pumped with a passively Q-switched Nd:GdVO₄ laser,” Appl. Phys. B **79**, 823–825 (2004).
- [16] R. Dabu, C. Fenic, and A. Stratan, “Intracavity pumped nanosecond optical parametric oscillator emitting in the eye-safe range,” Appl. Opt. **40**, 4334-4340 (2001).
- [17] Y. Yashkir and H. M. van Driel, “Passively Q-switched 1.57- μm intracavity optical parametric oscillator,” Appl. Opt. **38**, 2554-2559 (1999).

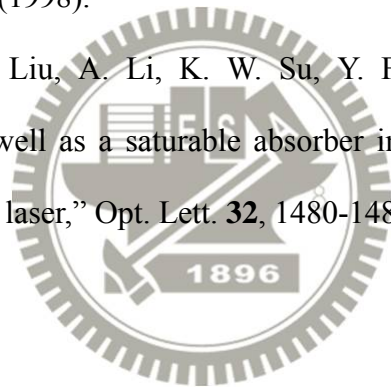
- [18] A. Agnesi, S. Dell'Acqua, and G. Reali, "Diode-pumped quasi-cw intracavity optical parametric oscillator at 1.57 μm with efficient pulse shortening," *Appl. Phys. B* **70**, 751-753 (2000).
- [19] W. Zendzian, J. K. Jabczyński, and J. Kwiatkowski, "Intracavity optical parametric oscillator at 1572-nm wavelength pumped by passively Q-switched diode-pumped Nd:YAG laser," *Appl. Phys. B* **76**, 355-358 (2003).
- [20] B. W. Schilling, S. R. Chinn, A. D. Hays, L. Goldberg, and C. W. Trussell, "End-pumped 1.5 μm monoblock laser for broad temperature operation," *Appl. Opt.* **45**, 6607-6615 (2006).
- [21] J. J. Degnan, "Optimization of passively Q-switched lasers," *IEEE J. Quantum Electron.* **31**, 1890-1901 (1995).
- [22] S. J. Brosnan and R. L. Byer, "Optical parametric oscillator threshold and linewidth studies," *IEEE J. Quantum Electron.* **15**, 415-431 (1979).
- [23] B. W. Schilling, S. R. Chinn, A. D. Hays, L. Goldberg, and C. W. Trussell, "End-pumped 1.5 μm monoblock laser for broad temperature operation," *Appl. Opt.* **45**, 6607-6615 (2006).
- [24] F. Q. Liu, H. R. Xia, Y. Zhong, S. Q. Sun, Z. C. Ling, D. G. Ran, W. L. Gao, J. L. He, H. J. Zhang, and J. Y. Wang, "Intracavity optical parametric oscillator at 1.57 μm by a diode-pumped Q-switched Nd:LuVO₄ laser," *Laser Phys. Lett.* **5**, 585-588 (2008).
- [25] Z. J. Liu, Q. P. Wang, X. Y. Zhang, Z. J. Liu, H. Wang, J. Chang, S. Z. Fan, F. S. Ma, and G. F. Jin, "Intracavity optical parametric oscillator pumped by an actively Q-switched Nd:YAG laser," *Appl. Phys. B* **90**, 439-443 (2008).

- [26] Y. F. Chen, S. W. Chen, S. W. Tsai, and Y. P. Lan, "Output optimization of a high-repetition-rate diode-pumped Q-switched intracavity optical parametric oscillator at 1.57 μm ," *Appl. Phys. B* **77**, 505-508 (2003).
- [27] T. L. Zhang, J. Q. Yao, X. Y. Zhu, B. G. Zhang, E. B. Li, P. Zhao, H. F. Li, F. Ji, and P. Wang, "Widely tunable, high-repetition-rate, dual signal-wave optical parametric oscillator by using two periodically poled crystals," *Opt. Commun.* **272**, 111-115 (2007).
- [28] L. Tartara, "Simple and versatile dual-signal wave optical parametric oscillator," *Opt. Lett.* **32**, 1105-1107 (2007).
- [29] P. B. Phua, K. S. Lai, and R. F. Wu, "Multiwatt high-repetition-rate 2- μm output from an intracavity KTiOPO₄ optical parametric oscillator," *Appl. Opt.* **39**, 1435-1439 (2000).
- [30] T. Debuisschert, J. Raffy, J. P. Pocholle, and M. Papuchon, "Intracavity optical parametric oscillator: study of the dynamics in pulsed regime," *J. Opt. Soc. Am. B* **13**, 1569-1587 (1996).
- [31] G. H. Xiao, M. Bass, and M. Acharekar, "Passively Q-switched solid-state lasers with intracavity optical parametric oscillators," *IEEE J. Quantum Electron.* **34**, 2241-2245 (1998).
- [32] Y. F. Chen, Y. P. Lan, and H. L. Chang, "Analytical model for design criteria of passively Q-switched lasers," *IEEE J. Quantum Electron.* **37**, 462-468 (2001).
- [33] J. J. Degnan, D. B. Coyle, and R. B. Kay, "Effects of thermalization on Q-switched laser properties," *IEEE J. Quantum Electron.* **34**, 887-899 (2001).

- [34] Y. F. Chen, J. L. Lee, H. D. Hsieh, and S. W. Tsai, "Analysis of passively Q-switched lasers with simultaneous modelocking" IEEE J. Quantum Electron. **38**, 312-317 (2002).
- [35] Y. Kalisky, "Cr⁴⁺-doped crystals: their use as lasers and passive Q-switches," Prog. Quantum Electron. **28**, 249-303 (2004).
- [36] S. Forget, F. Druon, F. Balembois, P. Georges, N. Landru, J.-P. Fève, J. Lin, and Z. Weng, "Passively Q-switched diode-pumped Cr⁴⁺:YAG/Nd³⁺:GdVO₄ monolithic microchip laser," Opt. Commun. **259**, 816-819 (2006).
- [37] A. R. Bijanzaden, and R. Khordad, "Study of output energy of Cr⁴⁺:YAG passively Q-switched Nd:YAG laser: using different setup," Opt. Commun. **282**, 2595-2603 (2009).
- [38] A. Agnesi, and S. Dell'acqua, "High-peak-power diode-pumped passively Q-switched Nd:YVO₄ laser," Appl. Phys. B **76**, 351-354 (2003).
- [39] J. Liu, J. M. Yang, and J. L. He, "High repetition rate passively Q-switched diode-pumped Nd:YVO₄ laser," Opt. Laser Technol. **35**, 431-434 (2003).
- [40] Y. F. Chen, S. W. Tsai, and S. C. Wang, "High-power diode pumped Q-switched and mode-locked Nd:YVO₄ laser with a Cr⁴⁺:YAG saturable absorber," Opt. Lett **25**, 1442-1444 (2000).
- [41] Y. F. Chen, S. W. Chen, Y. C. Chen, Y. P. Lan, and S. W. Tsai, "Compact efficient intracavity optical parametric oscillator with a passively Q-switched Nd :YVO₄/Cr⁴⁺ :YAG laser in a hemispherical cavity," Appl. Phys. B **77**, 493-495 (2003).

- [42] H. Chen, E. Wu, and H. P. Zeng, "Comparison between a-cut and off-axially cut Nd:YVO₄ lasers passively Q-switched with a Cr⁴⁺:YAG crystal," *Opt. Commun.* **230**, 175-180 (2004).
- [43] H. Ridderbusch and T. Graf, "Saturation of 1047- and 1064nm absorption in Cr⁴⁺:YAG crystals," *IEEE J. Quantum Electron.* **43**, 168-173 (2007).
- [44] G. J. Spühler, R. Paschotta, R. Fluck, B. Braun, M. Moser, G. Zhang, E. Gini, and U. Keller, "Experimentally confirmed design guidelines for passively Q-switched microchip lasers using semiconductor saturable absorbers," *J. Opt. Soc. Am. B* **16**, 376-388 (1999).
- [45] R. Häring, R. Paschotta, R. Fluck, E. Gini, H. Melchior, and U. Keller, "Passively Q-switched microchip laser at 1.5 μm," *J. Opt. Soc. Am. B* **18**, 1805-1812 (2001).
- [46] G. J. Spühler, S. Reffert, M. Haiml, M. Moser, and U. Keller, "Output-coupling semiconductor saturable absorber mirror," *Appl. Phys. Lett.* **78**, 2733-2735 (2001).
- [47] B. Y. Zhang, G. Li, M. Chen, G. J. Wang, and Y. G. Wang, "Passively Q-switched Nd:GdVO₄ laser with In_{0.25}Ga_{0.75}As being an output coupler," *Opt. Laser Technol.* **39**, 1094-1097 (2007).
- [48] M. Haiml, R. Grange, and U. Keller, "Optical characterization of semiconductor saturable absorbers," *Appl. Phys. B* **79**, 331-339 (2004).
- [49] K. Alavi, H. Temkin, W. R. Wagner, and A. Y. Cho, "Optically pumped 1.55-μm double heterostructure Ga_xAl_yIn_{1-x-y}As/Al_uIn_{1-u}As lasers grown by molecular beam epitaxy," *Appl. Phys. Lett.* **42**, 254-256 (1983).

- [50] W. T. Tsang and N. A. Olsson, "New current injection 1.5- μm wavelength $\text{Ga}_x\text{Al}_y\text{In}_{1-x-y}\text{As}/\text{InP}$ double-heterostructure laser grown by molecular beam epitaxy," *Appl. Phys. Lett.* **42**, 922-924 (1983).
- [51] N. Nishiyama, C. Caneau, B. Hall, G. Guryanov, M. H. Hu, X. S. Liu, M.-J. Li, R. Bhat, and C. E. Zah, "Long-wavelength vertical-cavity surface-emitting lasers on InP with lattice matched AlGaInAs-InP DBR grown by MOCVD," *IEEE J. Sel. Top. Quantum Electron.* **11**, 990-998 (2005).
- [52] Z. Burshtein, P. Blau, Y. Kalisky, Y. Shimony, and M. R. Kokta, "Excited-state absorption studies of Cr^{4+} ions in several garnet host crystals," *IEEE. J. Quantum Electron.* **34**, 292-299 (1998).
- [53] S. C. Huang, S. C. Liu, A. Li, K. W. Su, Y. F. Chen, and K. F. Huang, "AlGaInAs quantum-well as a saturable absorber in a diode-pumped passively Q-switched solid-state laser," *Opt. Lett.* **32**, 1480-1482 (2007).




Chapter 5

Beam-Quality Improvement of Millijoule

Q-Switched Lasers with an Unstable Cavity

Stabilized by Thermal-Lensing Effect

5.1 Unstable Cavity Design



Many lidar applications require laser radiation with high pulse energy, a short pulse duration, and low beam divergence. Plano-parallel resonators are the most commonly used cavities with simple configuration and excellent efficiency. Such a resonator can extract high energy but leads to a large beam divergence and poor beam quality. Practical resonator designs are typically a compromise between energy extraction and beam quality. A stable convex-concave resonator geometry has been proposed to achieve a large TEM₀₀ mode volume [1,2]. Kogan *et al.* [1] reported a cw 1-J frequency-doubled Nd:YAG laser. Chesler *et al.* [2] reported a cw Nd:YAG laser and mentioned that resonators designed for use with laser rods as large as 0.2-0.7 cm in diameter represent a compromise between large mode radius, insensitivity to perturbations, and compact resonator length. However, such stable convex-concave resonator requires either a long cavity length (>17 cm) or an optical resonator operating near the limit of stability. Therefore, the resonator becomes very sensitive to a misalignment of the mirrors. Thermal lensing in the laser crystal greatly

changes the size of the laser mode, which affects the overlap integrals, diffraction losses, pump threshold, laser slope efficiency, and TEM₀₀ mode output power [3]. Therefore, thermal lensing is not beneficial for stable resonators.

Recently, unstable resonators have been proposed to have not only large mode volumes but also the spatial mode selection [4,5], and experimentally demonstrated improved beam quality over that obtained with plano-parallel resonators [6,7]. Unstable resonators provide many advantages such as large mode volume, automatically collimated output beams, efficient power extraction, and good far-field beam patterns [8]. In this part, we design an unstable convex-concave resonator stabilized by thermal-lensing effect to generate a large fundamental mode volume in a passively Q-switched Nd:YAG/ Cr⁴⁺:YAG laser. By this unstable convex-concave resonator, a high-pulse-energy, high-peak-power, passively Q-switched laser with low beam divergence was achieved.

Fig.5.1.1 (a) shows the unstable resonator consisting of a plano-convex mirror and a meniscus mirror to be the front mirror and the output coupler, respectively. Note that the meniscus mirror provides a collimated output. The parameters of R_1 , R_2 , and L are the radii of curvature of cavity mirrors and cavity length, respectively. An optical resonator with an internal thermal lens (lens resonator) is shown in **Fig. 5.1.1 (b)**, where d_1 and d_2 the distances between the cavity mirrors and the principal planes of the laser crystal, and f is the focal length of the thermal lens. Note that the principal planes of the thermal lens can be approximated to be located inside the laser crystal at a distance $h = l/2n$ [9]. Such lens resonator exhibits the same Gaussian beam radii on the mirrors as the equivalent empty resonator with the equivalent g-parameters g_i^* and the equivalent resonator length L^* with [9]:

$$g_i^* = g_i - \frac{d_j}{f} \left(1 - \frac{d_i}{R_i} \right) \quad i, j = 1, 2; i \neq j \quad (1)$$

$$g_i = 1 - \frac{(d_1 + d_2)}{R_i} \quad (2)$$

$$L^* = d_1 + d_2 - \frac{d_1 d_2}{f}. \quad (3)$$

The mode beam radii ω_1 on the front mirror and ω_2 on the output coupler can be given by

$$\omega_i^2 = \frac{\lambda L^*}{\pi} \sqrt{\frac{g_j^*}{g_i^* (1 - g_1^* g_2^*)}} \quad i, j = 1, 2; i \neq j \quad (4)$$

Moreover, for a passively Q-switched laser as shown in **Fig.5.1.1 (c)**, the length of a saturable absorber has to be considered. Therefore the optical length $d_2^* = d_2 + l_s(1/n_s - 1)$ is used, where n_s is the refractive index of the saturable absorber, and l_s is the length of the saturable absorber.

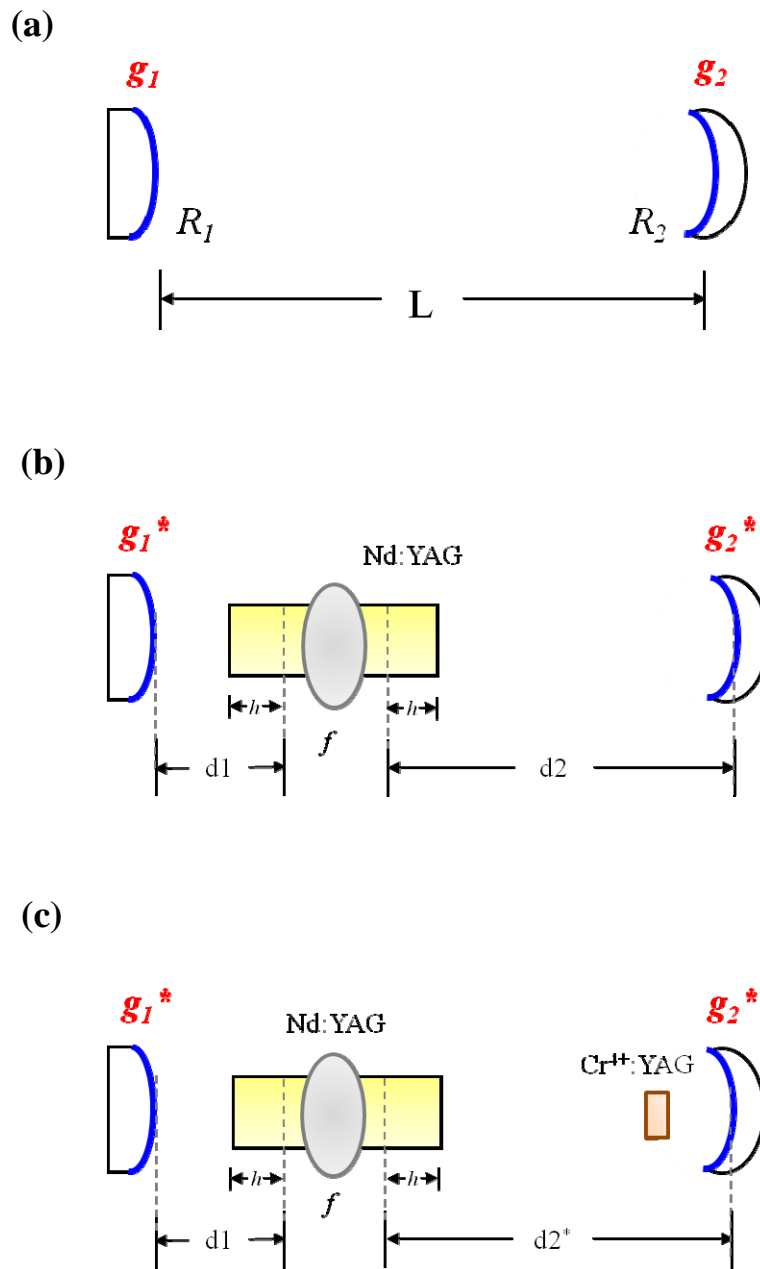


Fig.5.1.1. Schematic of (a) an unstable resonator configuration; (b) an unstable resonator with an internal lenslike laser rod; (c) an unstable resonator for a passively Q-switched laser with an internal lenslike laser rod and a Cr^{4+} :YAG crystal.

With Eqs. (1)-(4), the dependence of the mode size ω_i on the thermal focal length f for the present cavity configuration was calculated and shown in **Fig. 5.1.2**. In order to have a large mode volume in a compact cavity configuration, the cavity parameters are chosen to be $R_1 = -500$ mm, $R_2 = 600$ mm, and $L = 90$ mm. The other parameters used in the calculation are as follows: $d_1 = 35$ mm, $d_2 = 55$ mm, $n_s = 1.82$, and $l_s = 2$ mm. It can be seen that the mode size ω_i is insensitive to the thermal-lens focal length in the range of 3 m to 16 m. The parameters of $g_1 \cdot g_2$ for the present unstable cavity configuration are $g_1 \cdot g_2 > 1$ and $g_1 \cdot g_2 < 1$ without and with a thermal lens, respectively. In other words, the empty unstable cavity was transferred to a stable cavity by the thermal lensing effect. Using the ABCD-matrix method, the laser spot radius $\omega(z)$ propagating along the z-axis can be analyzed. The calculated results for the present unstable cavity configuration are shown in **Fig. 5.1.3**. The laser spot radius within laser cavity varies slightly in any case of the thermal focal length. Note that the thermal-lens focal length of quasi-cw diode pumped laser system is estimated to be about 10 m, corresponding to mode radius of 0.8 mm approximately.

On the other hand, the radius of curvature (ρ_3) of the output surface of the meniscus output coupler is designed to collimate the output laser beam. In order to avoid confusion, we redefined the symbols of the radii of curvature of cavity mirrors as ρ . Based on the intracavity laser spot size on output coupler and a transformation rule, the extracavity laser spot size can be analyzed. The transformation rule is called the ABCD law of Gaussian optics. The ABCD law relates the complex beam parameters, q_2 of a Gaussian beam at plane 2 to the value q_1 at plane 1 by using the ABCD ray matrix, which is given by

$$q_2 = \frac{Aq_1 + B}{Cq_1 + D} . \quad (5)$$

The complex beam parameter q is expressed as

$$\frac{1}{q(z)} = \frac{1}{R(z)} - i \frac{\lambda}{\pi \omega^2(z)} \quad (6)$$

where $R(z)$ represents the radius of curvature of the phase front and $\omega(z)$ is the beam radius.

If a light beam passes from air with index of refractive n_1 to a spherical interface with index of refractive n_2 and the radius of curvature ρ , the ray transfer matrix for refraction at a spherical interface is given by

$$M(\rho) = \begin{pmatrix} 1 & 0 \\ \frac{n_1 - n_2}{n_2 \rho} & \frac{n_1}{n_2} \end{pmatrix}. \quad (7)$$

Note that the radius of curvature ρ is positive for a convex mirror surface and negative for a concave mirror surface. The schematic of the backward laser beam transformation is show in **Fig. 5.1.4 (a)**. Therefore, the ray transfer matrix for the light beam q_2 passes two concave surfaces (ρ_2 and ρ_3) of this meniscus mirror and propagates a distance of z_2 is

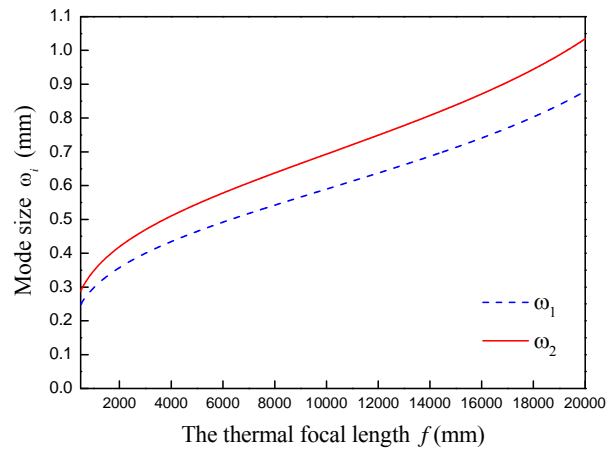
$$M(z_2) = \begin{pmatrix} 1 & z_2 \\ 0 & 1 \end{pmatrix} \begin{pmatrix} 1 & 0 \\ \frac{n_2 - n_1}{n_1 \rho_3} & \frac{n_2}{n_1} \end{pmatrix} \begin{pmatrix} 1 & 0 \\ \frac{n_1 - n_2}{n_2 \rho_2} & \frac{n_1}{n_2} \end{pmatrix} \quad (8)$$

Substituting $n_1 = 1$, $n_2 = 1.5$, $\rho_2 = -600$ mm, and $\rho_3 = -160$ mm into Eq. (8) and with Eqs. (5)–(6), the dependence of extracavity backward laser beam q_3 on position z_2 for several thermal focal lengths is shown in **Fig. 5.1.4 (b)**. The extracavity laser beams are collimated at different distances of z_2 for different thermal focal lengths f . The external beam waist position z_2 gets farther while larger thermal focal length f is given. However, the external beam is focused but not collimated when the thermal focal length is as large as 15 m. In conclusion, the radius of curvature of ρ_3 can be designed to fit in with the desired collimation conditions (collimated spot size and

position) in any cavity configuration case. This design concept, the output concave surface of an output coupler, is fairly significant for many practical applications.



(a)



(b)

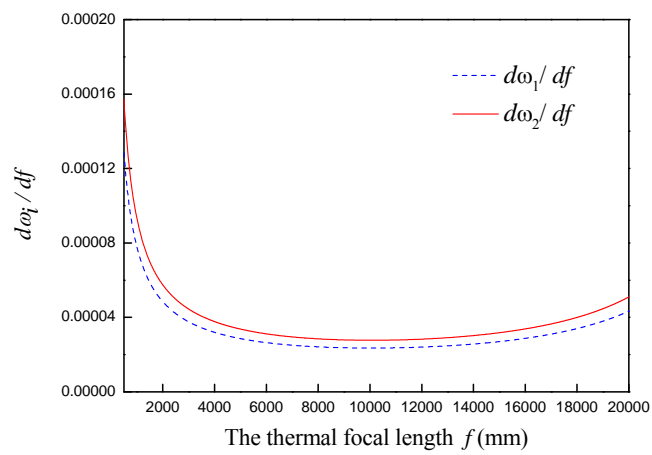


Fig.5.1.2. Calculated results for the dependence of (a) the mode size and (b) the mode-size gradient on the thermal focal length.

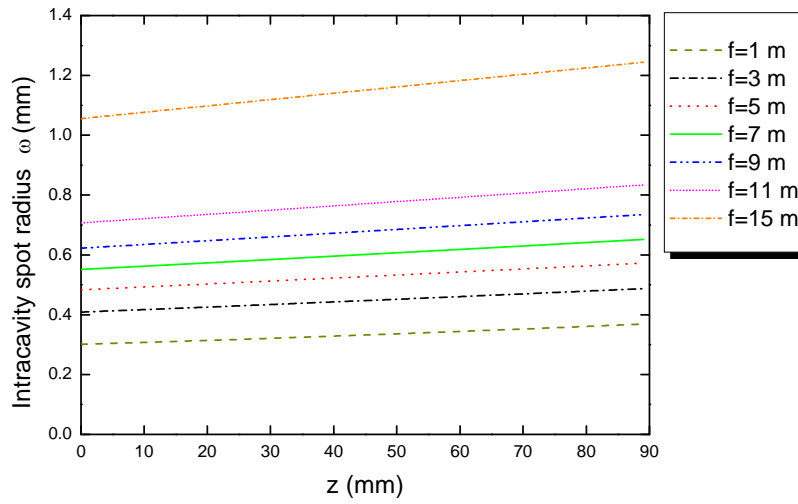


Fig. 5.1.3. The laser spot radius $\omega(z)$ varied along the laser propagation for various values of the thermal focal length f for this present unstable cavity configuration.

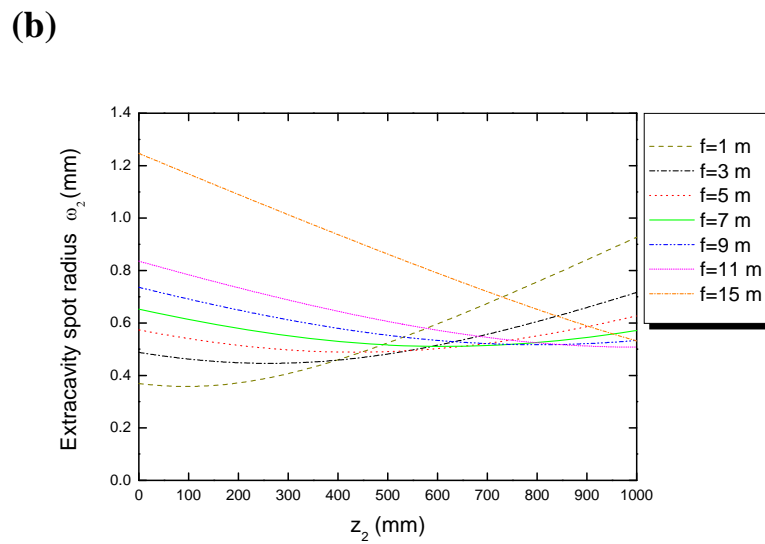
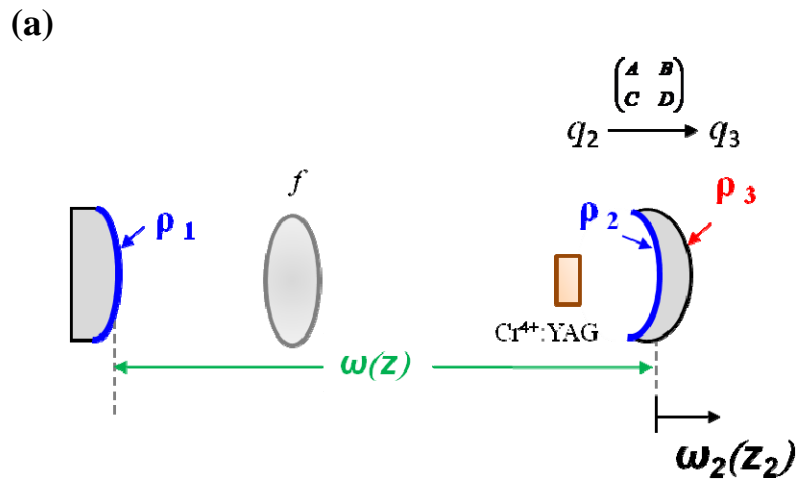


Fig. 5.1.4. (a) Schematic of the extracavity backward laser beam transformation, propagating along z_2 for the present cavity configuration; (b) the calculated results of the dependence of extracavity backward laser beam on position z_2 for several thermal focal lengths f .

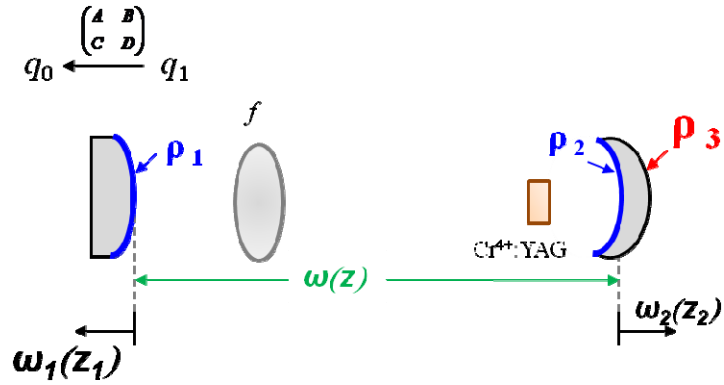
By the similar analytical method, the external forward laser beam q_0 can be also calculated. The schematic of the forward laser beam transformation is show in **Fig. 5.1.5 (a)**. The ray transfer matrix for the light beam q_1 passes a convex surface (ρ_1) of the front mirror and propagates a distance of z_1 is

$$M(z_1) = \begin{pmatrix} 1 & -z_1 \\ 0 & 1 \end{pmatrix} \begin{pmatrix} 1 & 0 \\ 1 & \frac{n_2}{n_1} \end{pmatrix} \begin{pmatrix} 1 & 0 \\ \frac{n_1 - n_2}{n_2 \rho_1} & \frac{n_1}{n_2} \end{pmatrix} \quad (9)$$

Substituting $n_1=1$, $n_2=1.5$, and $\rho_1 = +500$ mm into Eq. (9) and with Eqs. (5)–(6), the dependence of extracavity forward laser beam q_0 on position z_1 for several thermal focal lengths is shown in **Fig. 5.1.5 (b)**. It can be seen that the beam waist exists the front of the front mirror but not within the laser cavity for the present cavity configuration. This analyzed result is consistent with the beam propagation within the cavity.

In summary, we analyze an unstable cavity with a lens-like gain medium, in which carries a large mode volume. Additionally, a collimated laser beam can be accomplished by the output concave surface of an output coupler.

(a)



(b)

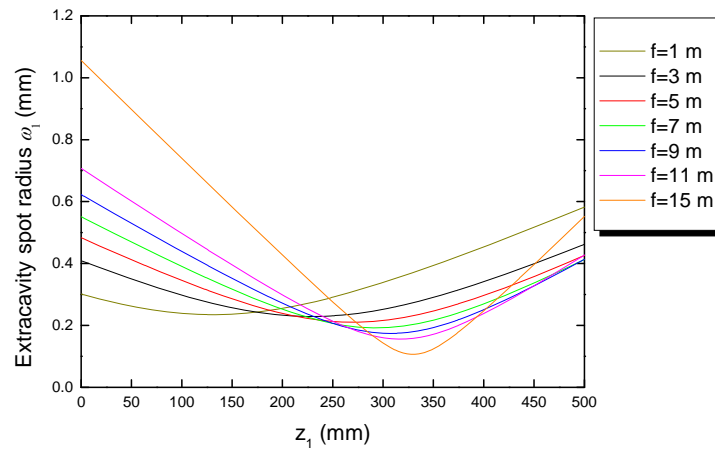


Fig. 5.1.5. (a) Schematic of the extracavity forward laser beam transformation, propagating along z_1 for the present cavity configuration; (b) the calculated results of the dependence of extracavity forward laser beam on position z_1 for several thermal focal lengths f .

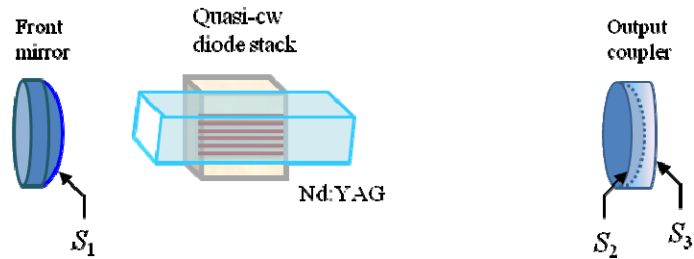
5.2 Experimental Setup

Figure 5.2.1 (a)-(c) show the experimental setups for a free-running Nd:YAG laser and a passively Q-switched Nd:YAG/Cr⁴⁺:YAG laser, respectively. The Nd:YAG crystal side-pumped by a quasi-cw high-power diode stack (Coherent G-stack package, Santa Clara, Calif., USA) which consisted of six 10-mm-long diode bars with a maximum output power of 120 W per bar at the central wavelength of 808 nm. The diode stack was constructed with 400 μm spacing between the diode bars so the whole emission area was approximately 10 mm (slow axis) \times 2.4 mm (fast axis). The full divergence angles in the fast and slow axes are approximately 35° and 10°, respectively. The diode stack was close to the lateral surface of the Nd:YAG crystal to have good pump efficiency.

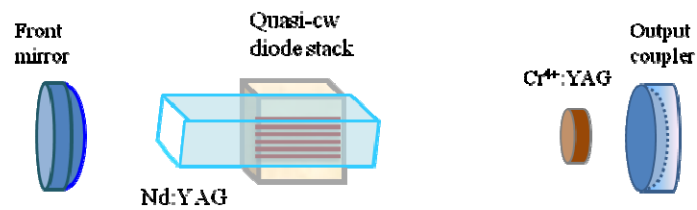
The Nd:YAG crystal dimensions are 4 \times 4 \times 25 mm³ with Nd³⁺ concentration of 1 at. %. Both end faces of the laser crystal were antireflection coated at 1064 nm ($R < 0.2\%$) and wedged 2° to avoid interference effects. The lateral surface of the laser crystal was polished and coated to be antireflective at 808 nm ($R < 0.2\%$). The Cr⁴⁺:YAG crystal with a thickness of 2 mm. Both surfaces of the Cr⁴⁺:YAG crystal were coated for antireflection at 1064 nm. The front mirror is a convex mirror with high-reflection coating at 1064 nm ($R > 99.8\%$), and the radius of curvature of S_1 is -500 mm. The output coupler is a meniscus mirror with radii of curvature of 600 mm and 160 mm for surfaces S_2 and S_3 , respectively.

Various Cr⁴⁺:YAG crystals with different initial transmission ($30\% \leq T_0 \leq 60\%$) and various output couplers with different reflectivity ($50\% \leq R \leq 70\%$) were used to optimize the output performance. The total cavity length was approximately 9 cm. The pulse temporal behavior at 1064 nm was recorded by a LeCroy digital oscilloscope (Wavepro 7100; 10 G samples/sec; 1 GHz bandwidth) with a fast InGaAs photodiode.

(a)



(b)



(c)

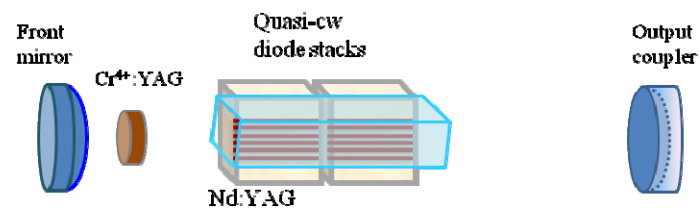


Fig. 5.2.1. Experimental setups of (a) the diode-side-pumped Nd:YAG laser in free-running operation; (b) the diode-side-pumped passively Q-switched Nd:YAG laser with a Cr⁴⁺:YAG crystal placed near the output coupler and (c) with a Cr⁴⁺:YAG crystal placed near the front mirror.

5.3 Results and Discussion

First of all, the quasi-cw free-running operation without saturable absorber was performed to confirm the quality of the laser crystal. For this investigation an output coupler with partial reflection at 1064 nm was used, and the diode stack was derived to emit optical pulses 250 μs long at a repetition rate of 20 Hz. **Figure 5.3.1** plots the experimental results of the free-running operation for the output energy as a function of the diode pump energy. The optimum reflectivity of the output coupler was found to be approximately 50%. The output energy of 48 mJ was achieved at an incident pump energy of 153 mJ. The overall slope efficiency was calculated to be as high as 44%. The fairly good efficiency affirms the pump scheme to be practical.

Employing a Cr^{4+} :YAG crystal to approach the output coupler, the passively Q-switched Nd:YAG/ Cr^{4+} :YAG laser was investigated. An output couplers with partial reflection at 1064 nm and a Cr^{4+} :YAG crystal with initial transmission were used, and the diode stack was derived to emit optical pulses 350 μs long at a repetition rate of 10 Hz. In order to generate high-pulse-energy Q-switched laser, a Cr^{4+} :YAG crystal with low initial transmission ($30\% \leq T_0 \leq 40\%$) was used. In this experiment, more output pulse energy was generated when the pump region was altered in the position of larger cavity mode size. The pump threshold energy increased with decreasing the initial transmission of a Cr^{4+} :YAG crystal. The laser threshold for the Cr^{4+} :YAG crystal with initial transmission of 30% was greater than the maximum pump energy that was approximately 280 mJ from the diode stack.

Using a Cr^{4+} :YAG crystal with initial transmission of 40% and an output coupler reflectivity of 55%, the optimized passively Q-switched laser was achieved. The threshold of the Q-switched laser operation was found to be approximately 180 mJ. The output pulse energy at 1064 nm was measured to be 18.5 mJ with an optical-to-optical efficiency of 10.5% with respect to incident pump energy. As presented in **Fig. 5.3.2 (a)**, the Q-switched pulse was found to display the mode-locking phenomenon, and the pulse envelope has temporal duration of approximately 7 ns. The repetition rate of the mode-locked pulses inside the

Q-switched pulses is approximately to be 1.36 GHz, with a pulse width of 340 ps as depicted in **Fig. 5.3.2 (b)**. The mode-locking phenomenon results in its maximum peak power up to 3.32 MW.



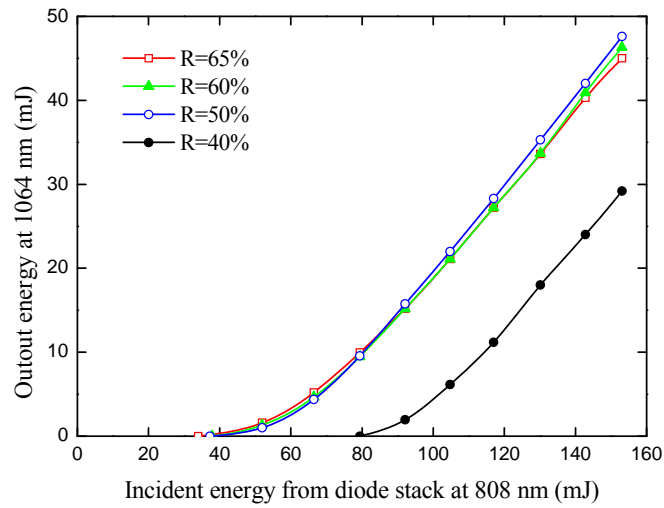
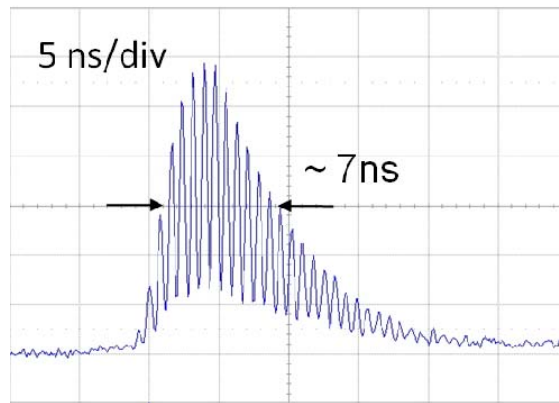


Fig. 5.3.1. Output energy at 1064 nm with respect to the incident pump energy at 808 nm for QCW free-running operation.

(a)



(b)

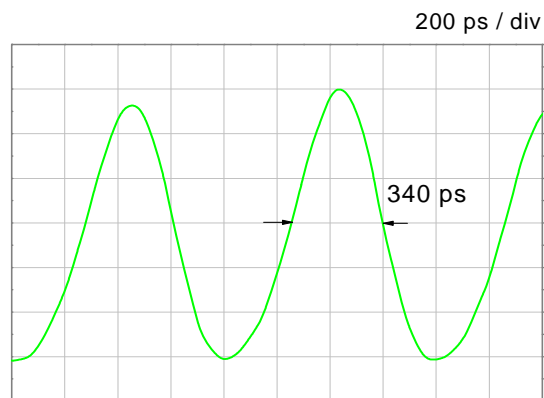


Fig. 5.3.2. Temporal characteristics of the Q-switched pulse in (a) and the expanded modulated pulse in (b).

Two types of passively Q-switched operations with the same Cr⁴⁺:YAG crystal ($T_o = 30\%$) and output coupler ($R = 70\%$), were used to demonstrate the influence of the position of a Cr⁴⁺:YAG crystal as depicted in **Fig. 5.2.1 (b)** and **(c)**. Experimental process revealed the laser threshold increased; for the reason, two diode stacks were used. Experimental result reveals that the output pulse energy was enhanced from 22 mJ to 34 mJ by changing the position of the Cr⁴⁺:YAG crystal near the output coupler to be adjacent to the high-reflection front mirror. The optical-to-optical efficiency was also enhanced from 6.3% to 7.5%. According the numerical result in **Fig. 5.1.3**, it can be found that the mode size is slightly decreased while varying the intracavity position from the output coupler to the front mirror. Therefore, it can be deduced that the enhanced output pulse energy is not caused by the mode size variation.

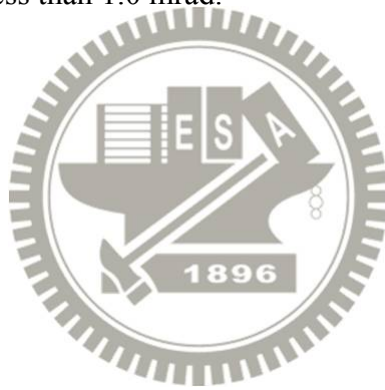
On the other hand, in a passively Q-switched laser, the initial population inversion density in the gain medium can be determined from the condition that the roundtrip gain is exactly equal to the roundtrip losses just before the Q-switch opens, i.e.

$$n_i = \frac{\ln\left(\frac{1}{T_o^2}\right) + \ln\left(\frac{1}{R}\right) + L}{2\sigma l}, \quad (10)$$

where T_o is the initial transmission of the saturable absorber, L is the round-trip fundamental wave intensity loss in the cavity, and R is the reflectivity of the output mirror. Physically, the output pulse energy is proportional to the initial population inversion density in the gain medium n_i that is an increasing function of the factor $\ln(1/T_o^2) + \ln(1/R) + L$. Therefore, the reasonable explanation of the experimentally enhanced output pulse energy is that the initial transmission factor of $2\ln(1/T_o)$ is different between two types of experimental setups. In other words, the effective initial transmission of the Cr⁴⁺:YAG crystal is altered by the adjacent cavity mirror.

Various Cr⁴⁺:YAG crystals with different initial transmission and various output couplers with different reflectivity were used in the experimental setup shown in **Fig.**

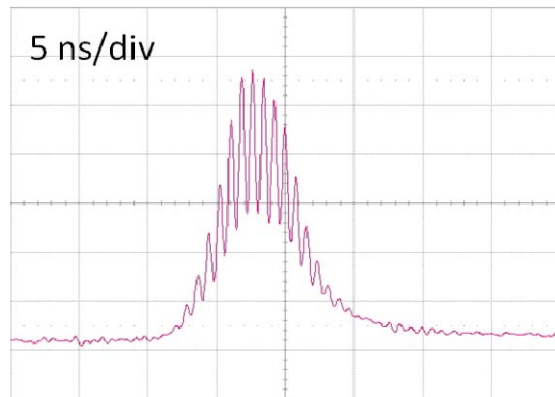
5.2.1 (c) to study the output performance. Experimental results are shown in **Tab. 5.3.1**. Using a Cr^{4+} :YAG crystal with initial transmission of 30%, the optimum reflectivity of the output coupler was found to be 70%. Lowering the reflectivity at 1064 nm is found to lead to a decrease in the output pulse energy and a relative increase in the peak power. The Q-switched pulse with an output coupler reflectivity of 70% is presented in **Fig. 5.3.3 (a)**, and the pulse envelope has temporal duration of approximately 6 ns. For this experimental setup, the effective performance was achieved with a Cr^{4+} :YAG crystal of initial transmission 40%. The output pulse energy of greater than 30 mJ was generated. Temporal characteristic of the Q-switched pulse with an output coupler reflectivity of 60% is shown in **Fig. 5.3.3 (b)**. The pulse envelope has temporal duration of approximately 4.5 ns, with the peak power of approximately 8 MW. Finally, the beam divergence (full angle) was measured and found to be less than 1.0 mrad.



Initial transmission T_0	Output coupler reflectivity R	Pump threshold (mJ)	Output pulse energy (mJ)	Pulse width (ns)	Peak power (MW)	Optical-to-optical efficiency (808nm→1064nm)
50%	50%	268	17~20	5	4~4.3	7.5 %
40%	60%	370	27~32	4~4.5	7.6~8.2	8.6%
	70%	454	30~34	6~7	6.8~7.6	7.5%
30%	65%	480	28~33	4.5~5	6.7~7.7	6.9%
	55%	506	28~32	5	7~7.8	6.3%

Tab. 5.3.1. Experimental results of passively Q-switched operations with a Cr^{4+} :YAG crystal posited to be adjacent to the high-reflection front mirror.

(a)



(b)

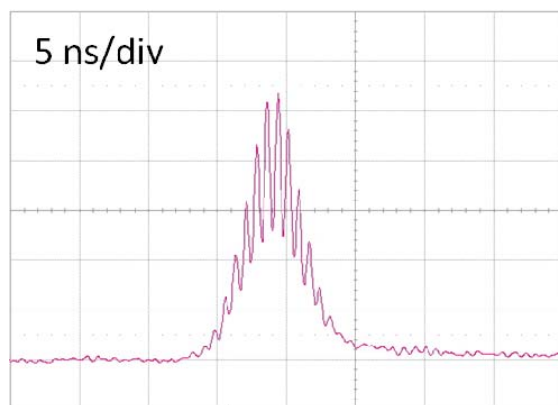
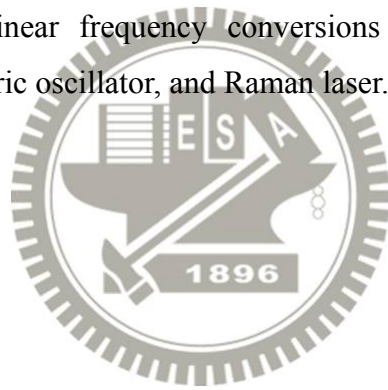


Fig. 5.3.3. Temporal characteristics of the Q-switched pulse: (a) $(T_0, R) = (30\%, 70\%)$, (b) $(T_0, R) = (40\%, 60\%)$.

5.4 Conclusions

We have analyzed an unstable cavity, which is stabilized by thermal lensing and provides a large-mode-volume. A meniscus output mirror is designed to collimate the laser beam. A side-pumped passively Q-switched Nd:YAG/Cr⁴⁺:YAG laser with high energy and low beam divergence was experimentally demonstrated. From experimental results we deduced that the effective initial transmission of the Cr⁴⁺:YAG crystal is altered by the adjacent cavity mirror. The Cr⁴⁺:YAG crystal positioned adjacent to the high-reflection cavity mirror leads to higher pulse energy output. Greater than 30 mJ of output pulse energy was generated with a Cr⁴⁺:YAG crystal of initial transmission 30%. The peak power was higher than 7 MW. The remarkable performance confirms the prospect of using this good beam quality and mJ Q-switched laser in nonlinear frequency conversions such as second harmonic generation, optical parametric oscillator, and Raman laser.



References

- [1] R. M. Kogan, and T. G. Crow, "A 1-J high- brightness frequency-doubled Nd:YAG laser," *Appl. Opt.* **17**, 927-930 (1978).
- [2] R. B. Chesler, and D. Maydan, "Convex-concave resonators for TEM₀₀ operation of solid-state ion lasers," *J. Appl. Phys.* **43**, 2254-2257 (1972).
- [3] W. J. Xie, W. T. Hu, J. D. Xu, and F. Zhou, "Dynamical thermal lensing of high-power solid-state lasers," *Opt. Eng.* **42**, 1439-1444 (2003).
- [4] M. L. Gong, S. S. Zou, G. Chen, P. Yan, Q. Liu, and L. Huang, "Threshold studies of pulsed confocal unstable optical parametric oscillators," *Opt. Express* **12**, 2932-2944 (2004).
- [5] T. Debuisschert, D. Mathieu, J. Raffy, L. Becouarn, E. Lallier, and J.-P. Pocholle, "High beam quality unstable cavity infrared optical parametric oscillator," in *Laser Resonators*, P. Galarneau and A. V. Kudryashov, eds., Proc. SPIE **3267**, 170-180 (1998).
- [6] J. N. Farmer, M. S. Bowers, and W. S. Scharpf, Jr., "High brightness eyesafe optical parametric oscillator using confocal unstable resonators," in *Advanced Solid State Lasers*, M. Fejer, H. Injeyan, and U. Keller, eds., **Vol. 26** of OSA Trends in Optics and Photonics (Optical Society of America, 1999), paper WC2.
- [7] B. C. Johnson, V. J. Newell, J. B. Clark, and E. S. Mcphee, "Narrow-bandwidth low-divergence optical parametric oscillator for nonlinear frequency-conversion applications," *J. Opt. Soc. Am. B* **12**, 2122-2127 (1995).
- [8] A. E. Siegman, *Lasers*, University Science, (Mill Valley, CA 1986).

- [9] N. Hodgson, and H. Weber, *Laser resonators and beam propagation: fundamentals, advanced concepts and applications*, Optical Sciences, 2th ed. (Springer, CA, 2005).



Chapter 6

Summary and Future Work

6.1 Summary

In this thesis we have realized the several fundamental emissions from standard Nd-doped lasers including the wavelengths of 0.94, 1.06, 1.44 μm . Based on nonlinear wavelength conversions, the intracavity frequency-doubled blue laser at 473 nm and an eye-safe optical parametric oscillator (OPO) at 1.57 μm have been achieved. Two pump source, including CW fiber-coupled laser diode and QCW two dimensional laser diode stacks, were used in our experiments.

First, diode-pumped quasi-three-level Nd:YAG lasers at 946 nm, blue light generation at 473 nm, and 946-nm passive Q-switching operation are performed in chapter 2. In order to reduce the reabsorption losses, short Nd:YAG crystals with a length of 2 mm are used. Under cw fiber-coupled laser diode pumping, the maximum output power at 946 nm is up to 3 W at an incident power of 19.6 W. Utilizing a BiBO nonlinear crystal, the blue laser with an average output power of 0.75 W is generated under a pump power of 13 W. For 946-nm passive Q-switching, a low-loss saturable absorber of InGaAs QWs has been developed. An average output power of 1.1 W is obtained at an incident pump power of 9.2 W. The maximum peak power is found to be up to 0.53 kW and the overall Q-switching efficiency is generally greater than 90%. The high-peak-power QCW diode stack is used as the pump source to achieve high-power Nd:YAG lasers. A lens duct with a smaller output aperture of $1.2 \times 1.2 \text{ mm}^2$ is used to deliver the pump radiation to the

laser crystal. At an on-time average pump power of 392 W, the maximum on-time average output powers at 946 nm and 473 nm are 34 W and 9 W, respectively. Furthermore, we experimentally demonstrate that the InGaAs QWs is superior to the Cr⁴⁺:YAG crystal because of the low nonsaturable losses. A QCW diode-pumped passively Q-switched Nd:YAG laser at 946 nm generates pulse energy of 330 μJ and peak power greater than 11 kW.

In chapter 3, the eye-safe laser at 1.44 μm is successfully realized by suppressing the higher gain transitions at 1.06 and 1.32 μm. We have developed an AlGaInAs material as a promising intracavity selective absorber (ISA) for an efficient high-power Nd:YAG laser at 1.44 μm. With the ISA to suppress operation at 1.06 μm, the output coupler at 1.44 μm can be straightforwardly designed and optimized. Experimental results confirm that the developed ISA can still fully suppress the 1.06 μm oscillation even if the cavity mirrors have a high-reflection coating at 1.06 μm. At a pump power of 16W, an output power of 2.5 W at 1.44 μm, with a slope efficiency of 23%, is achieved.

In chapter 4, eye-safe lasers at 1.57 μm with intracavity OPOs pumped by passively Q-switched Nd-doped lasers are performed. First, in Section 4.3 we have theoretically and experimentally verified that the threshold of an intracavity OPO in a shared cavity is controlled by the bleach of the saturable absorber not by the signal output reflectivity. A series of output couplers are used to optimize the OPO output performance. With a signal output reflectivity of 15%, an efficient subnanosecond eye-safe laser with 3.3 mJ pulse energy and 1.5 MW peak power is achieved at a pump energy of 65 mJ. Furthermore, in Section 4.4 we have developed an analytical model for designing the simultaneous emission of fundamental laser and OPO signal with a passively Q-switched IOPO. By means of a nonlinear regression fit to the numerical calculations, the output pulse energies of fundamental laser and converted OPO signal are expressed as analytical functions of the initial transmission of the saturable absorber and the reflectivity at fundamental laser wavelength. To verify the utilization of the present model, a passively Q-switched IOPO including both the fundamental laser at 1.06 μm and the OPO signal at 1.57 μm is systematically performed. With the reflectivity of 99.8%, 98%, 94%, and 90%, the output pulse

energies at 1064 nm are found to be 0.1, 1.9, 5.3, and 8.9 mJ, respectively; the corresponding pulse energies at 1572 nm are 10.8, 9.1, 7.7, and 6.6 mJ, respectively. Experimental results are found to be in good agreement with the results calculated from the analytic model. In section 4.5, an efficient diode-pumped passively Q-switched Nd:YVO₄ laser with the AlGaInAs QW material as a saturable absorber has been demonstrated to produce the 3.5 mJ pulse with a peak power of 1 MW at a repetition rate of 200 Hz. The excellent passively Q-switched Nd:YVO₄ laser is used as the intracavity OPO pump laser. An internal convex lens is used to achieve high conversion efficiency. With the optimum output coupler of $R_s = 80\%$, the OPO pulse energy is measured to be 1.53 mJ with a peak power of 60 kW. The effective conversion efficiency with respect to the optimized pulse energy from the passively Q-switched laser is up to 44%.

In chapter 5, we have designed an unstable cavity to not only carry a large mode volume but also improve the laser beam quality and beam divergence. Thermal lensing effect is useful in the unstable cavity. The qualitative analysis of cavity mode size with respect to the focal length of the thermal lensing is presented in section 5.1. A side-pumped passively Q-switched Nd:YAG/Cr⁴⁺:YAG laser with an unstable cavity has been experimentally demonstrated. From experimental results we deduce that the effective initial transmission of the Cr⁴⁺:YAG crystal is altered by the adjacent cavity mirror. The Cr⁴⁺:YAG crystal posited adjacent to the high-reflection cavity mirror leads to higher pulse energy output. With a Cr⁴⁺:YAG crystal of initial transmission 30%, greater than 30 mJ of output pulse energy and higher than 7 MW of peak power is generated. Experimental result reveals the excellent PQS performance with high energy and low beam divergence.

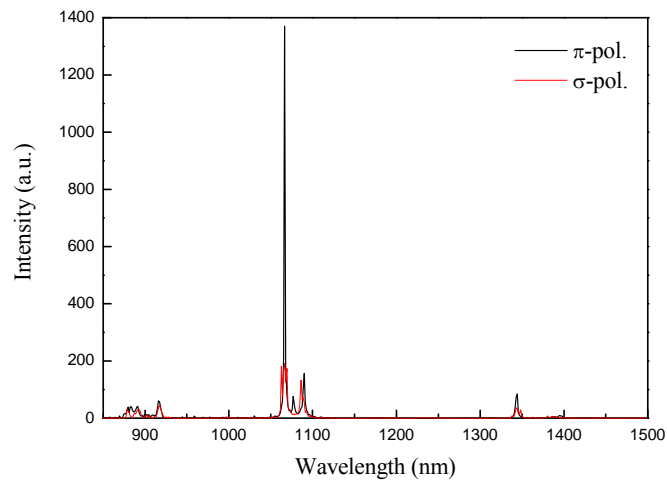
6.2 Future Work

The achievement of fundamental emissions from standard Nd-doped lasers can be applied to the further study, as follows. The remarkable performance of the passively Q-switched 946-nm laser in chapter 2 indicates the possibility of using InGaAs QWs structure to generate the high-peak-power blue laser at 473 nm with intracavity second harmonic generation. The excellent Q-switched laser with mJ pulse energy, good beam quality and low beam divergence in chapter 5 can be used in nonlinear frequency conversions such as eye-safe optical parametric oscillators, stimulated Raman lasers with extracavity KTP or YVO₄ crystals, and extracavity harmonic generations for 532-nm green laser and 355-nm UV laser in the future.

Neodymium (Nd)-doped vanadate crystals, including Nd:YVO₄ [1–3], Nd:GdVO₄ [4-8], and Nd:LuVO₄ [9,10], have been proved to be excellent laser materials and found many applications, due to their broad absorption bands, larger absorption and emission crosssections, and polarized emission. With Gd ions replacing a fraction of Y ions in Nd:YVO₄ crystal, the material parameters of which will be altered and different from the ordered ones. Nd-doped mixed Gd_xY_{1-x}VO₄ series crystals have proven to be advantageous over their corresponding ordered ones showing significant improvement in passively Q-switched laser performance [11,12]. As similar mixed crystals, Nd:Lu_xGd_{1-x}VO₄ crystals should also have excellent laser properties just like that of Nd:Gd_xY_{1-x}VO₄. Recently, Nd:Lu_xGd_{1-x}VO₄ crystals have been grown and their laser performances were studied at 1.06 μm and 1.34 μm [13,14].

Besides the common transition lines at 1.06 μm and 1.34 μm, we are interested in other special transition lines such as 1.08-1.09 μm in Nd:Lu_xGd_{1-x}VO₄ series crystals. The measured fluorescence spectrum of Nd:LuGdVO₄, is shown in **Fig. 6.2.1**. It could be found that there are interesting transition lines at 1.08-1.09 μm of a-cut and c-cut Nd:LuGdVO₄, which have a broaden bandwidth and different peaks of the σ and π polarizations. Therefore, we look forward that a simultaneous dual-wavelength laser is realized with the a-cut Nd:LuVO₄ laser in the future.

(a)



(b)

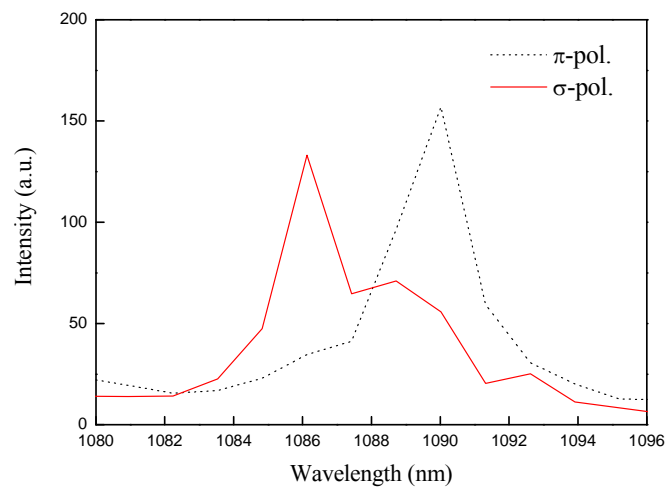


Fig.6.2.1. Room-temperature emission spectrum of an a-cut Nd:LuGdVO₄ and the partial region around 1.8-1.09 μm shown in (b).

References

- [1] R. A. Fields, M. Birnbaum, and C. L. Fincher, "Highly efficient Nd:YVO₄ diode-laser end-pumped laser", *Appl. Phys. Lett.* **51**, 1885-1886 (1987).
- [2] A. Agnesi, A. Guandalini, and G. Reali, "Efficient 671-nm pump source by intracavity doubling of a diode-pumped Nd :YVO₄ laser," *J. Opt. Soc. Am. B* **19**, 1078-1082 (2002).
- [3] C. Lu, M. Gong, Q. Liu, L. Huang, and F. He, "16.4 W laser output at 1.34 μ m with twin Nd:YVO₄ crystals and double-end-pumping structure," *Laser Phys. Lett.* **5**, 21-24 (2008).
- [4] T. Jensen, V. G. Ostroumov, J.-P. Meyn, G. Huber, A. I. Zagumennyi, and I. A. Shcherbakov, "Spectroscopic characterization and laser performance of diode-laser-pumped Nd: GdVO₄," *Appl. Phys. B* **58**, 373-379 (1994).
- [5] J. Yang, J. Liu, and J. He, "High efficiency continuous-wave operation of a diode-pumped Nd:GdVO₄ laser at 1.06 μ m," *Laser Phys. Lett.* **2**, 171-173 (2005).
- [6] S. V. Garnov, S. A. Solokhin, E. D. Obraztsova, A. S. Lobach, P. A. Obraztsov, A. I. Chernov, V. V. Bukin, A. A. Sirotkin, Y. D. Zagumennyi, Y. D. Zavartsev, S. A. Kutovoi, and I. A. Shcherbakov, "Passive mode-locking with carbon nanotube saturable absorber in Nd:GdVO₄ and Nd:Y_{0.9}Gd_{0.1}VO₄ lasers operating at 1.34 μ m," *Laser Phys. Lett.* **4**, 648-651 (2007).
- [7] W. Tian, C. Wang, G. Wang, S. Liu, and J. Liu, "Performance of diode-pumped passively Q-switched mode-locking Nd:GdVO₄/KTP green laser with Cr⁴⁺:YAG," *Laser Phys. Lett.* **4**, 196-199 (2007).

- [8] J. Yang, Q. Fu, J. Liu, and Y. Wang, "Experiments of a diode-pumped Nd:GdVO₄/LT-GaAs Q-switched and mode-locked laser," *Laser Phys. Lett.* **4**, 20-22 (2007).
- [9] C. Maunier, J. L. Doualan, R. Moncorgé, A. Speghini, M. Bettinelli, and E. Cavalli, "Growth, spectroscopic characterization, and laser performance of Nd:LuVO₄, a new infrared laser material that is suitable for diode pumping," *J. Opt. Soc. Am. B* **19**, 1794-1800 (2002).
- [10] Z. Wang, H. Zhang, F. Xu, D. Hu, X. Xu, J. Wang, and Z. Shao, "High-power, continuous-wave, Nd:LuVO₄ microchip lasers," *Laser Phys. Lett.* **5**, 25-28 (2008).
- [11] J. Liu, X. Meng, Z. Shao, M. Jiang, B. Ozygus, A. Ding, H. Weber, "Pulse energy enhancement in passive Q-switching operation with a class of Nd:Gd_xY_{1-x}VO₄ crystals," *Appl. Phys. Lett.* **83**, 1289-1291 (2003).
- [12] J. Liu, Z. Wang, X. Meng, Z. Shao, B. Ozygus, A. Ding, H. Weber, "Improvement of passive Q-switching performance reached with a new Nd-doped mixed vanadate crystal Nd:Gd_{0.64}Y_{0.36}VO₄," *Opt. Lett.* **28**, 2330-2332 (2003).
- [13] H. Yu, H. Zhang, Z. Wang, J. Wang, Y. Yu, Z. Shao, and M. Jiang, "Enhancement of passive Q-switching performance with mixed Nd:Lu_xGd_{1-x}VO₄ laser crystals," *Opt. Lett.* **32**, 2152-2154 (2007).
- [14] H. H. Yu, H. J. Zhang, Z. P. Wang, J. Y. Wang, Y. G. Yu, and M. H. Jiang, "Continuous-wave laser performance of Nd:Lu_xGd_{1-x}VO₄ operating at 1.34 μm," *Laser Phys. Lett.* **5**, 181-184 (2008).

Curriculum Vitae

Personal Data

Name: Yi-Ping Huang

Birthday: Feb. 3, 1983

Nationality: Taiwan (R.O.C.)

Birthplace: Tainan

Sex: Female

E-mail: nameep.ep94g@nctu.edu.tw; nameep@msn.com

Education

2005 ~ 2010 Ph.D. in Dep. of Electrophysics, National Chiao Tung University, Hsinchu, Taiwan.

2001 ~ 2005 B.S. in Dep. of Physics, Tunghai Hai University, Taichung, Taiwan.

1998 ~ 2001 Private Kang Ming High School, Tainan, Taiwan.

Work Experience

2005 ~ 2010 T. A. of General Physics, Differential Equations, and Optics Lab.

Specialty

Laser Technology and Physics

Nonlinear Optics

Publication List

(A) Journal papers:

1. **Y. P. Huang**, H. C. Liang, J. Y. Huang, K. W. Su, A. Li, Y. F. Chen, and K. F. Huang, "Semiconductor quantum-well saturable absorbers for efficient passive Q switching of a diode-pumped 946 nm Nd:YAG laser," *Appl. Opt.* **46**, 6273-6276 (2007)
2. **Y. P. Huang**, K. W. Su, A. Li, Y. F. Chen, and K. F. Huang, "High-peak-power passively Q -switched Nd:YAG laser at 946 nm," *Appl. Phys. B* **91**, 429-432 (2008)
3. **Y. P. Huang**, Y. T. Chang, K. W. Su, Y. F. Chen, and K. F. Huang, "AlGaInAs intracavity selective absorber for an efficient high-power Nd:YAG laser operation at 1.44 μ m," *Opt. Lett.* **33**, 1452-1454 (2008)
4. Y. T. Chang, **Y. P. Huang**, K. W. Su, and Y. F. Chen, "Diode-pumped multi-frequency Q -switched laser with intracavity cascade Raman emission," *Opt. Express* **16**, 8286-8291 (2008)
5. Y. T. Chang, **Y. P. Huang**, K. W. Su, and Y. F. Chen, "Comparison of thermal lensing effects between single-end and double-end diffusion-bonded Nd:YVO₄ crystals for ${}^4F_{3/2} \rightarrow {}^4I_{11/2}$ and ${}^4F_{3/2} \rightarrow {}^4I_{13/2}$ transitions," *Opt. Express* **16**, 21155-21160 (2008)
6. **Y. P. Huang**, H. L. Chang, Y. J. Huang, Y. T. Chang, K. W. Su, W. C. Yen, and Y. F. Chen, "Subnanosecond mJ eye-safe laser with an intracavity optical parametric oscillator in a shared resonator," *Opt. Express* **17**, 1551-1556 (2009)
7. W. Z. Zhuang, W. C. Huang, **Y. P. Huang**, K. W. Su, and Y. F. Chen, "Passively Q -switched photonic crystal fiber laser and intracavity optical parametric oscillator," *Opt. Express* **18**, 8969-8975 (2010)
8. Y. J. Huang, **Y. P. Huang**, H. C. Liang, K. W. Su, Y. F. Chen, and K. F. Huang, "Comparative study between conventional and diffusion-bonded Nd-doped vanadate crystals in the passively mode-locked operation," *Opt. Express* **18**, 9518-9524 (2010)

(B) Conference:

1. 黃依萍, 蘇冠暉, 張雅婷, 陳永富, 閻偉中, “精巧與高效率的人眼安全腔內光參數震盪器雷射,” 96 年度國防科技學術合作計畫成果發表會 45CS, 論文集 B-32, 龍潭(2007)
2. Y. P. Huang, H. C. Liang, J. Y. Huang, K. W. Su, A. Li, Y. F. Chen, and K. F. Huang, “Semiconductor quantum-well saturable absorbers for efficient passive Q switching of a diode-pumped 946 nm Nd:YAG laser,” Optics and Photonics in Taiwan (OPT2007), CP-005, Taichung (2007)
3. Y. P. Huang, K. W. Su, Y. T. Chang, and Y. F. Chen, “MW passively Q-switched eye-safe laser from compact intracavity optical parametric oscillator, ” Annual Meeting of the Physical Society of the Republic of China, Hsinchu (2008)
4. Y. T. Chang, K. W. Su, Y. P. Huang and Y. F. Chen, “High-power diode-pumped actively Q-switched Nd-doped Raman laser employing an undoped YVO4 crystal as a Raman medium,” Annual Meeting of the Physical Society of Republic of China, Hsinchu (2008)
5. 黃依萍, 張漢龍, 黃郁仁, 蘇冠暉, 陳永富, 閻偉中, “精巧與高能量的人眼安全腔內光參數震盪器雷射,” 97 年度國防科技學術合作計畫成果發表會 CS52, 論文集, 龍潭 (2008)
6. 莊威哲, 黃依萍, 蘇冠暉, 陳永富, 黃凱風, “被動與主動式 Q 開關鏡摻雜光子晶體光纖雷射之比較性研究,” 98 年度國防科技學術合作計畫成果發表會 CS43, 論文集, 龍潭(2010)